國立臺灣大學理學院物理學系

博士論文

Department of Physics

College of Science

National Taiwan University

Doctoral Dissertation

高質量恆星形成區域的磁場演化

Evolution of Magnetic Fields in High Mass Star Formation

湯雅雯

Ya-Wen Tang

指導教授：賀曾樸 博士

Advisor: Paul T. P. Ho, Ph.D.

中華民國 98 年 6 月

June, 2009

Abstract

In this thesis, I study the role of Magnetic (B) fields in the massive star forming process. It has been suggested that B field plays a key role in the star formation process - it sustains the molecular cloud from collapsing rapidly and helps to redistributes the flux density and angular momentum via ambipolar diffusion. However, there are limited measurements of B field strengths and also field morphologies, due to the weak signal and the limitation of instruments. The measurements of B-field morphologies associated with star-forming cores with high angular resolution, $\sim$ a few arcseconds, are only available since recent decades. With the Submillimeter Array, the B field morphologies projected in the plane of sky ($B_\perp$) are traced by mapping the thermal continuum emission of the dust grains at wavelengths of 870 μm. I study four massive star star forming regions in various evolutionary stages: the collapsing core W51 e2/e8 and W51 North:dust, the Ultracompact H II (UC H II) region G5.89-0.39, and the closest massive star forming site Orion BN/KL. The source in the earliest evolutionary stage, the dense core MMS 6 in OMC-3, is also observed.

As inferred from the gas kinematics and the complicated B field morphology, the B field in G5.89 is most likely been overwhelmed by the stellar feedbacks, such as expansion of the UC H II region and the molecular outflows. While in the collapsing core W51 e2/e8, the hourglass-like B field associated with e2 seems to be located in a subcritical envelope at a scale of 0.5 pc, suggesting that the B field plays a dominant role in the formation process of the star-forming cores. The field geometry in W51 North:dust is complex but organized, correlated with the fragmentation and the rotation of the flattened structure. B field in Orion BN/KL shows a part of the larger scale (0.5 pc) hourglass morphology. In MMS 6, no smaller B field structure is detected, suggesting that the field is relatively uniform across the OMC-3 filament. In this thesis, I conclude that the role of the B field varies with the evolutionary stages of the central stars. The high angular resolution B field map is crucial when study the role of the B field in the star forming region. To understand the role of the B field, kinematics of the molecular cloud and linking the field geometry with larger scale field are necessities.

摘要

在此博士論文中，我分析磁場在高質量恆星形成區域所扮演的角色。

一般認為，磁場在恆星形成過程中扮演很重要的角色。它提供支持的力量，使得分子雲可以緩慢地塌縮，因此可以解決僅有極少比例的分子雲形成恆星的問題。另外，它可以重新分布磁通量以及轉動慣量，使得物質可以掉入中心的原恆星。然而，一直到近十年才開始有高解析度(約數角秒)的磁力線型態、而且極為有限的歸測資料。其中，次毫米波陣列是目前唯一可以偵測毫米與次毫米波段的偏極化光的陣列。這波段對恆星形成區域的塵埃輻射特別敏感。藉由觀測塵埃的熱輻射中的偏極化光，我們可以推得磁場投影的天球上的磁力線型態。利用次毫米波陣列，我研究四個在不同演化階段的高恆星形成區域：超緻密氫離子區 G5.89-0.39，塌縮原恆星核 W51 e2/e8 以及 W51 North，以及離我們最近的高質量恆星形成區域 Orion BN/KL。此外，獵戶座分子雲 3 (OMC-3)中最亮的高密度核 MMS 6 也是本論文的研究天體。

根據所分析的分子雲的運動狀態與所觀測到的複雜磁力線型態，超緻密氫離子區天體 G5.89-0.39 的磁場明顯的受到擾動。比較此天體中所存在的輻射壓力、氣體的力學能密度與磁壓力，我們估計輻射壓在靠近中心的高質量恆星位置的地方，有足夠的能量密度可以擾動磁場與推動附近的分子雲。在演化更早期的天體 W51 e2/e8 區域，我們看到被吸積盤面拉扯的磁力線型態。而在此塌縮核以外的分子雲氣中，磁場呈現非常規則的狀態。此結果傾向支持磁場主導的分裂過程。比較這兩個處於不同演化狀態的天體 G5.89-0.39 及 W51 e2/e8，觀測所看到的磁力線分布型態，取決於恆星形成區域的演化狀態。若是中心的恆星已經釋放出足夠的能量，並且週遭的分子雲已經明顯的受到擾動，則所觀測到的磁力線可能極為複雜。而在演化比較早期的階段，磁力顯然扮演極為重要的角色—它主導分子雲氣演化到塌縮核的過程。而在演化最早期的天體 MMS 6，磁通量明顯的比其他天體還低。此外，沒有更小尺度的磁力線型態存在，顯示獵戶座分子雲 3 的磁力線型態是非常均勻、規則的。因為磁場的投影影像容易受到投影作用的影響，我們需要更多的塌縮核的磁力線觀測數據。塌縮核 W51 North 磁力線已經受到分化過程的影響，其中大部分的高密度核中的磁力線方向約略一致，然而在密度最高的區域，磁力線明顯地受到規則地拉扯。我們需要一些數值模擬來解釋在這個區域所看到的磁力線型態。最後，觀測較近的高質量恆星形成區域的磁力線可以提供磁場在較小尺度的資訊。根據我們所觀測到 Orion BN/KL 天體內的磁力線型態，我們發現在以往所看到的較大尺度(約 0.3 pc)均勻的磁場中，磁力線在比較小尺度內呈現明顯的規則、且較複雜的磁力線型態。在 Orion BN/KL 中，根據先前的的氨氣觀測數據顯示，此區域的分子雲處於非重力束縛態。此外，磁場方向有規則地變化方向。因此，我們推測所觀測到的磁場型態極可能是殘留的偽吸積盤面。

總結，在本論文中，我發現磁場所扮演的角色隨著恆星形成區域的演化階段而改變。高解析度的磁場型態資料、分析分子雲內的氣體運動狀態、以及比較小尺度與大尺度的磁場型態對研究恆星形成區域中的磁場極為重要。

Contents

List of Figures

List of Tables

Citations to Previously Published Work

Two chapters of the thesis have been published or accepted for publication in the Astrophysical Journal.

"Evolution of Magnetic Fields in High Mass Star Formation: SMA dust polarization image of the UCHII region G5.89-0.39" Tang, Ya-Wen, Ho, Paul T. P., Girart, Josep. M., Rao, Ramprasad, Koch, Patrick M., & Lai, S.-P. 2009, ApJ, 695, 1399 (chapter 5)

"Evolution of Magnetic Fields in High Mass Star Formation: Linking Field Geometry and Collapse for the W51 e2/e8 Cores" Tang, Ya-Wen, Ho, Paul T. P., Koch, Patrick M., Girart, Josep Miquel, Lai, Shih-Ping, & Rao, Ramprasad 2009, ApJ, in press (chapter 2)

The following three chapters are in preparation to be submitted in ApJ.

Chapter 3: Field geometry in rotating disk/ring system W51 North: dust

Chapter 4: Resolving the polarization in Orion BN/KL with 2 milli-parsec resolution

Chapter 6: B field geometry in relatively quiescent core MMS 6 in OMC 2/3

Acknowledgments

I am most grateful to my thesis advisor Paul T. P. Ho for the support and inspiring discussions on both science and life. I thank Josep Miquel Girart, Ramprasad Rao and Shih-Ping Lai for the fruitful collaborations on the thesis projects. The visit to Stephane Guilloteau and Anne Dutrey in the summer of 2008 in Bordeaux is a very important and nice experience in the way I do research. I thank postdocs, students and assistants in IAA for all the good time we spent together and helpful discussions. I appreciate the encouragement and support from Professor Hsiang-Kuang Chang and Yi-Jehng Kuan when I just started the graduate study. Finally, I thank Patrick Koch for the unconditionally mental support and also fruitful discussions.

Chapter 1

Introduction

In star formation process, magnetic (B) field is expected to play an important role traditionally. It provides the mechanism to enable the material to accrete onto the central "protostar" by removing the excess angular momentum. In larger scales, B field is thought to sustain the molecular cloud from collapse globally. However, there are limited observational results of the B field strength and morphology in the star forming regions, especially observations with higher angular resolution (a few arcseconds).

Toward low mass star forming regions, the B field morphology was revealed to be hourglass-like in NGC 1333 IRAS 4A (Girart, Rao & Marrone 2006), which is a consequence of the contraction and formation of a disk. Will high mass stars ($M > 8M_\odot$) form via an accretion disk as in the low mass case? Will interactions between group members and the much faster evolutionary time scales be the dominant criteria? Will the B field play a dominant role in the massive star formation process? In the PhD study, I observe a list of massive star formation sites with high angular resolution (up to $0.7''$) to measure the B field morphologies using the thermal dust polarization and the gas kinematics using the molecular emission lines. I summarize current understanding of the process of star formation in molecular clouds, and also the control mechanism of the star formation process in §1.1. The method to probe the B field in star forming regions are described in §1.2.

1.1   Star formation in molecular clouds

It has been well known that the stars are formed inside the molecular cloud. However, the star formation efficiency inside the cloud is low, typically a few percent of the mass is converted into stellar mass (Zucherman & Evans 1974). One of the main questions in the star formation process is that how to sustain the molecular cloud from gravitational collapse. Both the B field and the turbulence are suggested to play the dominant role. In the classical scenario, the B field is suggested to play the important role in sustaining the cloud from collapse. The material starts to collapse toward a "seed" through the ambipolar diffusion. However, this scenario can explain the isolated star formation and also only limited to the low mass case. In contrast, the turbulence dominant model seems to explain better the observed cluster formation, and also the diversity of the mass distribution of the stars. In the turbulent dominant theory, the molecular cloud is only a transient phenomena, which is formed by the compress of the turbulent flows. In this case, the B field is suggested to play a minor role in the evolution of the molecular cloud and therefore, the star formation process.

1.1.1   Magnetic Field or Turbulence Dominates Star Formation?

To test these two extreme dominant models, the key parameter of the magnetic dominant model is the mass-to-flux ratio ϕ. The molecular cloud is original sustained by the magnetic field and is sub-critical, i.e. $\phi < 1$. Because the ambipolar diffusion timescale τ_{AD} is ionization rate dependent: $\tau_{\mathrm{AD}} \propto \chi_e \propto n_{\mathrm{H}_2}^{-0.5}$ (McKee 1989; Mouschovias 1991). At denser region, τ_{AD} is smaller and therefore, the collapsing cores can be formed through ambipolar diffusion. One of the main prediction of the magnetic driven star formation is the existence sub-critical envelope and the super-critical cores.

In the turbulence driven model, the main argument is based on the ages of some star forming cores, typically only a few times of the free-fall time scale. In this scenario, the molecular cloud is supported by turbulence. Once the turbulence dissipates,

the molecular cloud will start to collapse, and therefore, the cloud is only a transient phenomena.

Why is it so important to study which mechanism is the dominant force? The observational constraint can provide the key to the theorists about the driving mechanism. The prediction of the turbulent driven or magnetic driven star formation is different. The study of the driven mechanism is the fundamental question.

1.1.2   Previous approach to the problem

Mass to Flux ratio

The mass to flux ratio $\phi_{\mathrm{M,B}}$ in the isolated low-mass star forming cores has been studied using the SCUBA in L183, L43, L1544 (Ward-Thompson et al. 2002; Crutcher et al. 2004), L1498 and L1517B (Kirk et al. 2006). The magnetic field and turbulence are reported to be equally important in these isolated and moderately quiescent cores (Ward-Thompson et al. 2006). As comparing the $\phi_{\mathrm{M,B}}$ in four envelope and the corresponding cores, Crutcher, Hakobian, & Troland (2009) report that $\phi_{\mathrm{M,B}}$ in the core does not larger than the one in the envelope, and suggest that the cores are not formed purely through ambipolar diffusion.

Estimate of the ages of star forming cores

The age of the intermediate cores, $14M_{\odot} < M < 80M_{\odot}$, has been suggested to be in the order of million years, significantly longer than free fall or turbulent decay timescale (Netterfield et al. 2009). Proposed by the same authors, B field is more likely to be dominant. In contrast, Motte et al. (2007) suggested that high-mass prestellar and protostellar cores are in a high dynamic state, and therefore, turbulence seems to dominate in the molecular cloud.

In summary, there is no single answer to which force is dominant in the star formation processes in previous approaches.

1.2   Massive Star Formation through Accretion?

The formation of low mass stars (M $\sim$ 1M$_\odot$, L$\sim$ 1L$_\odot$) are well characterized observationally. Infall via accretion disks, the removing of excess angular momentum via winds and outflows, as described by standard models (see review by Shu et al. 1987), appear to operate up to intermediate stellar masses (M$_\odot$ $\sim$ 8 M$_\odot$, L $\sim$ 10^4 L$_\odot$). In particular, for stellar luminosity up to 10^{4}L$_\odot$, detected molecular outflows are highly collimated, circumstellar disks are found (Cesaroni et al. 2005), and their properties appear to be scaled-up versions of low mass cases (Beltrán et al. 2008).

The formation process of the more massive stars could be fundamentally different. High mass star forming regions, because of their rarity, are usually at greater distances. They are also located always in dense and massive regions, as they are typically formed in a group. Theoretically, the environment of high mass star forming region is very different from the low mass case because of the high radiation pressure and the stronger gravitational field. The observed molecular outflows appear poorly collimated. This may be because that the more massive stars will reach the main sequence stage very quickly, in 10^4 years. Accretion and molecular outflows are likely still in process when the central stars already begin nuclear burning and thereby radiate in the ultraviolet. Thus, the molecular material near the central star will be photoionized if the accretion pressure is not high enough. If the inner core is ionized, the high plasma pressure may affect the accretion and the outflow process (Shepherd 2003, Königl 1999). Furthermore, observed outflows may contain the emission from multiple sources, since the massive stars are always formed in a dense cluster. Hence, both poor resolution and complexity have plagued observational studies. We thus need higher angular resolution observations to provide better physical constraints on the theoretic models of the massive star formation process.

1.3 Approach to the Problems: B field morphologies in the plane of sky

In this thesis, I observe the B field morphology in the plane of sky ($B_\perp$) in the massive star forming regions to analyze the problems listed before. The $B_\perp$ is derived from the observed polarized dust continuum emission. The method is explained here.

1.3.1 Alignment Mechanism

The polarized light of the dust continuum can provide the morphology of the B field on the plane of sky ($B_\perp$). The dust grain is paramagnetic and elongated, and it is in the lowest energy state when aligned perpendicular to the magnetic field (Davis & Greenstein (1951) for the original theory; Lazarian (2007) for the recent review of the alignment mechanisms). Although the alignment mechanism of the dust grains has been a difficult topic for decades, the radiation torques seem to be a promising mechanism to align the dust grains with the B field (e.g., Draine & Weingartner 1996; Lazarian & Hoang 2007). Dust grains are thought to be aligned with their monor axes parallel to the B field in most of the cases, even if the alignment is not magnetic (Lazarian 2007).

1.3.2 Polarized Dust Emission

The polarized light can be from the absorption of the background stellar light, which is due to the difference of the fraction of the light being absorbed between the major and minor axes. Using this method, the detection of the polarization is restricted to the locations where the background stars can be seen. The polarization direction is parallel to the B field direction in this case. While in the star forming site, the extinction is so hight that most of the radiation will be absorbed. Observations at far-infrared and (sub-)millimeter, which trace the thermal dust emission from star forming sites directly are powerful to trace the dense regions. Again, in the case when dust grains are aligned with the B field, the polarized emission can be detected. Due the difference in the emissivity along the major and minor axes, the emitted

light will appear to be linearly polarized. In this case, the polarized emission will be perpendicular to the B field direction.

1.3.3   The Chandrasekhar-Fermi Method

The field strength in dense clouds can be estimated by using the Chandrasekhar-Fermi (CF) method (Chandrasekhar & Fermi 1953). Assuming the dispersion of the position angles of the detected polarization is caused by the perturbation by Alfvén waves or turbulence in the magnetic field lines, the strength of the B field projected in the plane of sky ($B_\perp$) is given by:

$$B_\perp = Q\sqrt{4\pi\bar{\rho}}\frac{\delta V}{\delta\phi}(mGauss).\qquad(1.1)$$

Here, the factor Q is a dimensionless parameter < 1, which depends on the cloud structure, the $\bar{\rho}$ is the mean gas density in g cm^{-3}, δV is the velocity dispersion along the line of sight in km s^{-1}, $\delta\phi$ is the dispersion of the polarization position angles in radian. This CF method can be applied in a strong field condition ($\delta\phi < 25°$) with Q of 0.5, according to Ostriker, Stone, & Gammie (2001). The resultant polarized dust emission has been studied successfully using the SMA and BIMA, such as in the case of NGC1333 IRS 4A (SMA), W51 e1/e2 cores (BIMA), DR(21) (BIMA), NGC2071 (BIMA) and NGC2024 IRS5 (BIMA). In this thesis, I use the thermal dust polarized emission to map the B field in the massive star formation sites.

1.4   Previous $B_\perp$ measurements: far-IR to mm

1.4.1   single dish polarization: SHARC, HERTZ and SCUBA

At 100 μm, observations done with Stokes on the KAO have angular resolutions of 35″. At 350 μm, observations obtained with Hertz in CSO are typically with the resolution of 18″. The observed $B_\perp$ morphologies tend to be uniform at pc scale, such as M17 (Dotson 1996), OMC-1 (Schleuning 1998), W3 (Dotson et al. 2000), and DR 21 MAIN (Kirby 2009). At 850 μm, the angular resolution of polarization

observations can reach to $14''$ with SCUBA in JCMT. The revealed polarization in the OMC-2 and OMC-3 filaments (Matthews, Wilson & Fiege 2001) and in OMC-1 (Vallee & Fiege 2007) are also uniform. There are also cases where the revealed $B_\perp$ are complex, such as NGC 7538 (Dotson et al. 2000) and W51 A (Chrysostomou et al. 2002).

These observations are measuring the B field morphology in the scale of the molecular cloud. A decrease of polarization percentage is commonly seen toward the star forming cores (denser regions), where the field direction shows an abrupt change in some cases. The star forming cores can only be resolved in the interferometry observations.

1.4.2   interferometer: BIMA and SMA

The interferometric observations at (sub-)millimeter carried out prior this thesis work are typically at the angular resolution of $3''$ to $10''$. Both uniform and complex field field geometries have been detected. Due to the sensitivity and the low polarization percentage, most of the observations are toward high mass star forming region. Complex field geometry has been detected in Orion BN/KL (Rao et al. 1998). Uniform field geometries which suggestive of hourglass-like morphologies are seen toward NGC 2024 (Lai et al. 2002), NGC 1333 IRAS 4A (Girart, Rao & Marrone 2006), and G30.79 FIR 10 (Cortes & Crutcher 2006). At this scale, the decrease of polarized percentage toward the emission peak is also seen.

In interferometric observations, the star forming regions can be resolved with the angular resolution of Jeans lengths scales in the massive star forming regions. The $B_\perp$ morphologies linking the cores with the molecular cloud can be resolved.

1.5   Structure of the thesis

To understand the roles of B field in the star formation regions, I have studied the B field morphology and the kinematics of the molecular clouds in different evolutionary stages. Because the polarization percentage is low, typically $\sim 5\%$ in the

star forming regions, we choose to the star forming regions which are strong in the thermal dust emission. The stages of the source observed are in the earlier stage where collapse is still dominant, to the more evolved stage, where the stellar feedback start to influence the surrounding material. The angular resolution reached ranges from $0.''7$ to $3''$.

In Chapter 2 to 6, I present results of the case studies on five sources at different evolutionary stages. The conclusion and future direction are presented in Chapter 7.

Chapter 2

Linking field geometry and collapse for the W51 e2/e8 cores

Ya-Wen Tang, Paul T. P. Ho, Patrick M. Koch, Josep M. Girart, Shih-Ping Lai, &
Ramprasad Rao
2009 ApJ, in press

ABSTRACT

We report our observational results of 870 μm continuum emission and its linear polarization in the massive star formation site W51 e2/e8. Inferred from the linear polarization maps, the magnetic field in the plane of sky ($B_\perp$) is traced with an angular resolution of $0\rlap{.}''7$ with the Submillimeter Array (SMA). Whereas previous BIMA observations with an angular resolution of $3''$ (0.1 pc) showed a uniform B field, our revealed $B_\perp$ morphology is hourglass-like in the collapsing core near the Ultracompact H II region e2 and also possibly in e8. The decrease in polarization near the continuum peak seen at lower angular resolution is apparently due to the more complex structures at smaller scales. In e2, the pinched direction of the hourglass-like B field morphology is parallel to the plane of the ionized accretion flow traced by H53α, suggesting that the massive stars are formed via processes similar to the low mass stars, i.e. accretion through a disk, except that the mass involved is much larger.

Furthermore, our finding that the resolved collapsing cores in e2 and e8 lie within one subcritical 0.5 pc envelope supports the scenario of *magnetic fragmentation* via ambipolar diffusion. We therefore suggest that magnetic fields control the dynamical evolution of the envelope and cores in W51 e2 and e8.

ISM: individual (W51 e2/e8) — ISM: magnetic fields — polarization — stars: formation

2.1 Introduction

The magnetic (B) field has been suggested to play an important role in the star formation process. While the B field flux density is eventually redistributed via ambipolar diffusion (Mestel & Spitzer 1956; Mouschovias 1978), the collapse itself is slowed sufficiently to explain the low star formation rate observed in molecular clouds. Alternative support via turbulence (cf. Mac Low & Klessen 2004) seems less important on parsec (pc) scales since the B fields in the plane of sky ($B_\perp$) are often observed to be organized and uniform across the cloud, such as in M17 (Dotson 1996), OMC-1 (Schleuning 1998) and DR21 MAIN (Kirby 2009). One key question is at which sizescale will the magnetic support be overcome by gravity. The morphology of the B field at that point may reveal the details of the contraction process such as geometry and timescale. The Submillimeter Array (SMA) can be used to address this question by resolving the $B_\perp$ structures via dust polarization studies with high angular resolutions at typically a few arcseconds.

The B field is traced by the dust continuum emission. The dust grains are most likely not spherical in shape, but somewhat elongated. They are thought to be aligned with their minor axes parallel to the B field in most of the cases (Lazarian 2007). Among different alignment mechanisms, radiation torques seem to be a promising mechanism to align the dust grains with the B field (Draine & Weingartner 1996; Lazarian & Hoang 2007). Due to the differences in emissivity perpendicular and parallel to the direction of alignment, the observed thermal dust emission will be linearly polarized. The direction of the linear polarization is therefore perpendicular to the B field. With the SMA, we are able to detect the polarized component of the thermal

dust emission at sub-millimeter (sub-mm) wavelengths in order to trace the B field within the dense cores, where stars are formed. Compared to the polarization studies via absorption and scattering of stellar light in the optical or near infrared (Goodman et al. 1995), sub-mm polarization, being derived directly from dust emission, does not suffer from a limited range in grain size and the possible contamination from the more diffuse emission and absorption along the line of sight.

In this paper, we present SMA observational results with an angular resolution of $0\rlap{.}''7$ (0.02 pc) of the massive star forming site W51 e2 and e8 in W51 MAIN. The dust continuum at a wavelength of 870 μm, and the $B_\perp$ field inferred from its linearly polarized component are presented. The W51 MAIN is on the eastern edge of W51. It is at a distance of 7.0±1.5 kpc (Genzel et al. 1981) or 6.1±1.3 kpc (Imai et al. 2002). Here, we adopt a distance of 7 kpc. There is a group of Ultracompact H II (UCHII) regions in W51 MAIN, and many H_2O, OH and NH_3 maser spots have been identified (Genzel et al. 1981; Gaume & Mutel 1987; Pratap et al. 1991) to be associated with the e2 and e8 regions. The terminology of the structures discussed in this paper is shown in the schematics in Figure 1. The radio continuum sources e2, e4, e8, e1 and e3 are UCHII regions (Gaume & Johnston 1993; Zhang & Ho 1997), and their locations are labelled in Figure 2. Hereafter, *e2*, *e4*, *e8*, *e1* and *e3* (when in *italic*) refer to their corresponding UCHII regions. The infall signatures toward the e2 and e8 regions (i.e., e2 and e8 collapsing cores) have been detected clearly in NH_3 (Ho & Young 1996; Zhang & Ho 1997) and in CS (Zhang, Ho, & Ohashi 1998), indicating that they are in an early evolutionary stage. Furthermore, the total luminosity of the W51 MAIN is 2×10^6 $L_\odot$ (Jaffe et al. 1987), indicating that it is a massive star forming site.

The polarized dust emissions associated with the envelope of the W51 e2 and e8 regions have been previously observed at 1.3 mm and 850 μm. The $B_\perp$ field structure varies with different size scales. Chrysostomou et al. (2002) has shown that the morphology of the field on the very large scale observed with SCUBA with an angular resolution of $\sim 10''$ (0.5 pc) appears more complex, possibly because of projection effects from several clouds along the line of sight. With an angular resolution of $\sim3''$ (0.1 pc) with the BIMA, Lai et al. (2001) found that the position angles (P.A.s)

of the polarization vectors vary smoothly across the e2 and e8 cores (Figure 2(a)), suggesting that the B field dominates over the turbulent motions in the envelope. At which scales will the B field lose its dominance over turbulence and gravity?

2.2   Observation

The observations were carried out on 2008 July 13 using the SMA (Ho, Moran, & Lo 2004) [1] in the extended configuration, with seven of the eight antennas available. The projected lengths of baselines ranged from 30 to 262 kλ. The largest size scale which could be sampled in this observation was $\sim 8''$ (0.3 pc). The local oscillator frequency was tuned to 341.482 GHz. With the 2 GHz bandwidth in each sideband, we were able to cover the frequency ranging from 345.5 to 347.5 GHz and from 335.5 to 337.5 GHz in the upper and lower sidebands, respectively. The phase center is near *e2* at Right Ascension (J2000) = $19^h23^m43^s.95$, Declination (J2000)=$14°30'34''.00$. *e8* is $\sim 7''$ south of the phase center. The primary beam (field of view) of the SMA at 345 GHz is $\sim 30''$.

Linear polarization (LP) observations using interferometer arrays are best obtained using receivers which detect both orthogonal circular polarizations (CP) simultaneously. However, the SMA receivers are intrinsically linearly polarized and only one polarization is available currently. Thus, quarter-wave plates were installed in order to convert the LP to CP. Detailed information of the design of the quarter-wave plates and how the quarter-wave plates were controlled is described in Marrone et al. (2006) and Marrone & Rao (2008). We assume that the smearing due to the change of the P.A.s on the time scale of 5 minutes in one cycle of polarization measurement is negligible.

The conversion of the LP to CP is not perfect. This instrumental polarization (also called the leakage terms) (see Sault et al. 1996) and the bandpass were calibrated by observing 3c454.3 for 2 hours while it was transiting in order to get the best coverage

---

[1] The Submillimeter Array is a joint project between the Smithsonian Astrophysical Observatory and the Academia Sinica Institute of Astronomy and Astrophysics and is funded by the Smithsonian Institution and the Academia Sinica.

of parallactic angles. The instrumental polarization is ∼1% for the upper sideband and ∼3% for the lower sideband before calibration, and ∼0.6% after calibration in both sidebands. The complex gains were calibrated every 12 minutes by observing 1751+096 until it set, followed by 1925+211 for the last 3.5 hours. The absolute flux scale was calibrated using Titan.

The data were calibrated and analyzed using the MIRIAD package. After the standard gain calibration, self-calibration was also performed by selecting the visibilities with uv distances longer than 40 kλ. In order to Fourier transform the measured visibilities to the image, the task INVERT in MIRIAD was used with natural weighting. The Stokes Q and U maps are crucial for the derivation of the polarization. We use the dirty maps of Q and U to derive the polarization in order to avoid a possible bias introduced from the CLEAN process. We applied CLEAN to the Stokes I (total intensity) map in order to reduce the sidelobes. The presented SMA images have all been corrected for the primary beam attenuation. The synthesized beam of the presented maps is $0\farcs7 \times 0\farcs6$ with a P.A. of $-58°$. The presented polarization vectors are gridded to a $0\farcs3$ spacing - which is about half of the synthesized beam FWHM - in order to show the curvature of the B field morphology. Therefore, adjacent polarization vectors are not formally independent within one synthesized beam. However, as usual, relative information can be extracted at under the synthesized beam resolution.

The Stokes I, Q and U images of the continuum are constructed with natural weighting in order to get a better S/N ratio for the polarization. The noise levels of the I, Q and U images are ∼ 60, 4 and 4 mJy Beam^{-1}, respectively. The strength (I_p) and percentage ($P(\%)$) of the linearly polarized emission are calculated from: $I_\mathrm{p}^2 = Q^2 + U^2 - \sigma_{Q,U}^2$ and $P(\%) = I_\mathrm{p}/I$, respectively. The term $\sigma_{Q,U}$ is the noise level of the Stokes Q and U images, and it is the bias correction due to the positive measure of I_p (Leahy 1989; Wardle & Kronberg 1974). The σ_{I_p} is thus 4 mJy beam^{-1}. To derive the polarization, the MIRIAD task IMPOL was used. The SMA polarization vectors presented are above $3\sigma_{I_\mathrm{p}}$ in red segments and between 2 to 3 σ_{I_p} in black segments.

2.3   Results

The 870 μm continuum emission and its polarized components were detected (Figure 2; Table 1 & 2). The results are presented in this section.

2.3.1   Continuum Emission

In e2, a compact 870 μm continuum emission structure with a radius of $\sim 1''$ (0.03 pc) is centered at $\sim 0''.7$ east of *e2*. Extending to the north-west of this compact emission, a fainter structure with an overall length of $\sim 2''$ (0.07 pc) is detected. The H_2O (Genzel et al. 1981) and (J,K)=(9,6) NH_3 (Pratap et al. 1991) masers are located in this north-west extension, $\sim 2''$ away from the continuum peak. Associated with the continuum peak, there are OH masers detected within $0''.5$ to the east and $\sim 1''$ to the south of *e2* (Gaume & Mustel 1987; Fish et al. 2006), suggesting that it is an active star forming site.

In e8, the 870 μm continuum peak is centered at $0''.3$ west of *e8*. *e4*, *e1* and *e3* are at the periphery of the 870 μm continuum emission. There is an extension toward the south-west with an overall length of $\sim 3''$. Associated with *e8*, an NH_3 maser spot was detected $0''.8$ south of the 870 μm continuum peak by Pratap et al. (1991). The OH (Gaume & Mustel 1987) and H_2O (Genzel et al. 1981) masers are also associated with *e8* and the 870 μm continuum peak, suggesting again that this is an active star formation site.

When fitted with a Gaussian, the deconvolved size of the 870 μm emission in e2 is $0''.9 \times 0''.8$, slightly larger than the synthesized beam, and therefore, the e2 core has been resolved. For e8, the deconvolved size is $0''.9 \times 0''.3$ with a P.A. of 12°. Therefore, e8 has been resolved along the major axis of the dust ridge but not along the minor axis. In both e2 and e8, the 870 μm continuum emissions are associated with the NH_3 cores (Ho et al. 1983; Zhang & Ho 1997), suggesting that they are also tracing the dense regions.

The measured 870 μm flux densities within the upper and lower boxes in Figure 2(b), associated with e2 and e8, are 9.3 and 4.0 Jy, respectively. The flux densi-

ties of the free-free continuum F_{ff} at 1.3 cm in e2 and e8 are 300 mJy (Gaume & Johnston 1993) and 17 mJy (Zhang & Ho 1997), respectively. In order to estimate the F_{ff} contribution at 870 μm, we extrapolate from 1.3 cm, assuming $F_{ff} \propto \nu^{-0.1}$. Although this assumption of optically thin emission is crude, it has been shown that the resultant F_{ff} roughly agrees (within a factor of 3) with the estimate from the radio recombination line at 2 mm (Zhang, Ho, & Ohashi 1998), suggesting that the assumed $F_{ff} \propto \nu^{-0.1}$ is reasonable. The extrapolated F_{ff} at 870 μm is $\sim$230 and 13 mJy for e2 and e8, respectively. As compared to the 870 μm flux densities, F_{ff} contributes $\sim$2% for the e2 region and 0.3% for the e8 region. Therefore, the 870 μm continuum is dominated by dust emission. Hereafter, the structures traced by the 870 μm emission in the e2 and e8 regions are named as e2 dust ridge and e8 dust ridge, respectively.

Assuming a dust temperature of 100 K (Zhang, Ho, & Ohashi 1998), a dust grain emissivity $Q(\lambda) \propto \lambda^{-\beta}$ with $\beta = 1$, and the normal gas to dust ratio of 100, we estimate gas masses M_{gas} of 245 and 106 M$_\odot$ for the e2 and e8 dust ridges, respectively (cf. Tang et al. 2009). Note that the M_{gas} given here is highly affected by the assumed β. If the assumed β is 2, the estimated M_{gas} will be 14 times larger. Assuming the extents along the line of sight are equal to the diameters of the emission area in the e2 and e8 dust ridges, the average gas number densities $n_{\mathrm{H_2}}$ are 3.4$\times10^6$ and 2.2$\times10^6$ cm^{-3}, respectively. By using the same equation and the same assumed values of β and dust temperature, the M_{gas} estimated from the 2 mm dust continuum (Zhang, Ho, & Ohashi 1998) for the e2 and e8 dust ridges are 1100 and 590 M$_\odot$, respectively. The difference in the estimated M_{gas} at 2 mm and 870 μm is most likely due to the missing flux from the extended component, which is not recovered with our SMA observations. In comparison, with the same assumptions, the M_{gas} of the envelope is 1834 M$_\odot$ as traced at 1.3 mm by BIMA (Lai et al. 2001). The M_{gas} associated with the e2 and e8 dust ridges recovered with our SMA observations is $\sim 19\%$ of the M_{gas} in the envelope.

The main conclusion from the dust continuum data is that the associated mass is large. The morphology of the dust continuum is elongated. The positional offsets between the various embedded sources are significant, such as between the positions

of the 870 μm peaks and the UCHII regions. These results are consistent with the formation of a cluster of stars.

2.3.2   Dust Polarization

The polarization in the e2 and e8 dust ridges is detected and resolved (Figure 2 (c) and (d)). Throughout the paper, P.A. is defined from the north to the east. In the e2 dust ridge, the bulk of the polarization vectors form a ring around the 870 μm peak with a radius of $\sim 1''$ and with the geometric center near the continuum peak instead of *e2*. In the north-west extension of the dust ridge, the polarization appears to be perpendicular to the major axis of the extension.

The e8 dust ridge is $\sim 7''$ away from the phase center. Even though the antenna response is 15% less efficient than at the phase center, the polarization revealed is clearly also not as uniform as previously seen with BIMA. The polarization vectors again form a ring like structure around the continuum peak. The polarization is weaker in e8 with more vectors between 2 to 3 $\sigma_{I_{\mathrm{p}}}$.

In comparison, the polarization in the envelope of the e2 and e8 regions, as revealed with an angular resolution of $3''$ (0.1 pc) with BIMA, shows a relatively uniform distribution in P.A. and therefore, a fairly uniform $B_\perp$ field at 1.3 mm (Figure 2(a); Lai et al. 2001). In their results, the polarization in the e2 region is weak and resolved into e2 main and e2 pol NW, named in the same paper, according to the P.A. of the polarization vectors. The component e2 pol NW is at $3''$ to the north-west of *e2*. There is a gap where no polarized emission is detected between *e2* and e2 pol NW. In the e8 region, the polarization in the BIMA results is nearly uniform with a decrease in polarization percentage near the peak position.

In order to test if the differences in polarization properties from SMA and BIMA are due to their different angular resolutions, we smoothed our SMA results to the BIMA resolution, as shown in Figure 3. Wherever the polarized emission was both detected at 1.3 mm and 870 μm, the resultant P.A.s of the polarization differed by $\sim 30°$ on average. This significant difference can be due to the different sampling of the visibilities, which are in the range of 6 to 170 kλ (λ=1.3 mm) for the BIMA

and in the range of 30 to 262 kλ (λ=870 μm) for the SMA. Specifically, the SMA filtered out the more extended and uniform component which is larger than 8$''$. At the same angular resolution, the derived global B$_\perp$ field directions in e2 and in e8 are therefore consistent in the regions where both the SMA and BIMA have polarization detections. Most importantly, the smoothed SMA polarization map shows that the polarization percentage has decreased significantly, especially near the continuum peak positions, where the field geometry is more complex at the resolution of 0$\overset{''}{.}$7. This demonstrates that the low polarization percentage at the emission peaks is due to the limited angular resolution when a more complex underlying B field morphology has not been resolved. This effect can also be due to the decrease of the alignment efficiency of the dust grains in denser regions (Lazarian & Hoang 2007) or due to geometrical effects, such as the differences in the viewing angles (Gonçalves et al. 2005). However, in this case, the complex B field structure is the dominant effect.

The polarization percentage $P(\%)$ decreases with increasing continuum intensity I in both e2 and e8 even for the higher resolution SMA results (Figure 4). Since the BIMA results come from a resolution effect, the same might be true for the SMA results at the emission peaks. Away from the emission peaks, the general increase in $P(\%)$ is somewhat misleading. Figure 2(a) shows that this effect is not symmetrical on either side of the elongated envelope, i.e. the $P(\%)$ differs with positions on the same contour level of I. This is reflected by the large dispersion in $P(\%)$ at any value of I/I_{max}. Several effects, including B field geometry related to the line of sight, need to be disentangled. That the $P(\%)$ ranges mainly between 1% to 10% (Figure 4), seems to agree with the model of grain growth in the dense regions where grain alignments are via radiative torques (see Figure 11 in Pelkonen et al. 2009). However, based on our results, the effects of angular resolution and geometry must first be taken into account.

2.4   Discussion

2.4.1   Hourglass B field Morphology inside the e2 dust ridge?

The inferred B field in the e2 dust ridge exhibits a complex but organized morphology (Figure 5). We have tested the hypothesis of the measured B field being radial, and have shown quantitatively the preference of a non-radial field at a high significance level (see Appendix). There are positions where no polarized emission (depolarization) is detected, extending along a P.A. $\sim 60°$ across the 870 μm peak (color scale in Figure 2(c)). The existence of non-radial field lines together with the depolarized zones are in favor of an hourglass field morphology. Along the extension of the dust ridge toward the north-west, the B field lines are approximately parallel to the major axis, which is consistent with the BIMA measurement at 1.3 mm. These lines are radial-like, but the complex structure in the north-west could belong to another embedded source as possibly indicated by the masers.

Associated with *e2*, organized motions in the ionized gas have been revealed with the H53α radio recombination line (Keto & Klaassen 2008), with the maximum velocity gradient along P.A. $\sim 60°$. These authors interpret this gradient as a supporting evidence for an accretion flow along a dense flattened structure, where the detected motion tracks the ionized particles on the surface of the dense midplane. Both the infall and rotation near *e2* have also been detected in several molecular lines (Ho & Young 1996; Zhang & Ho 1997; Zhang, Ho & Ohashi 1998). As discussed in Keto & Klaassen (2008), this H53α accretion flow in the direction of P.A. $\sim 60°$ might drive the molecular outflow at P.A. $\sim -20°$ as traced by the CO 2-1 line. The argument is based on the hypothesis that if the massive star formation process is similar to the low mass case, the bipolar outflow should be along the rotation axis. The linearly distributed H$_2$O and OH masers in the W51 e2 region could trace an outflow (Figure 19(c) in De Buizer et al. 2005), as identified with the CO 2-1 line. Although the determined direction may be highly uncertain, the rotation in NH$_3$ (3,3) is more clearly revealed along PA=135° (Figure 7 in Zhang & Ho 1997) and in CH$_3$CN along PA=110° (Zhang, Ho & Ohashi 1998), which seems inconsistent with the gradient de-

tected with the H53α ionized flow. This might indicate that the revealed kinematics based on different lines may be from multiple embedded sources. Higher spatial resolution kinematic studies with hot core molecular lines will be helpful for deciphering the underlying structures.

The B field appears to be hourglass-like near *e2*, with the field lines pinched along the plane of the proposed H53α accretion disk. If the B field lines are frozen into the ionized material, the field lines will be tangled along with the rotation and infall motions. The revealed depolarization might then result from the more complex underlying B field. We note that the field lines seem to go to the core with an essentially radial pattern, and therefore, leading to a sharp pinched angle in the hourglass. In contrast, the low mass case (Girart, Rao, & Marrone 2006) shows a wider and smoother pinched angle. We speculate that a larger infall momentum and a larger differential rotation (Zhang, Ho, & Ohashi 1998) might drag the field lines along and result in a narrower pinched angle in the projected plane. Projection of a nearly pole-on hourglass-like morphology possibly also leads to similar signatures. In any case, the scenario of material accreting through a disk as proposed by Keto and Klaassen (2008) is supported by our inferred B field morphology.

2.4.2   Hourglass B field Morphology in the e8 dust ridge?

Along the e8 dust ridge, the B field also shows a systematic deviation from the larger scale (0.5 pc) B field revealed by BIMA. This can again be explained by the field lines being dragged along with the accretion toward *e8*. In this case, the revealed B field appears to be part of an hourglass structure on a larger scale of 4″ ($\sim$0.08 pc) (Figure 5(b)), with its pinched direction parallel to the dust ridge. Centered on the e8 continuum peak, a compact hourglass structure would be more convincing except for the field lines to the north. There are H$_2$O masers north of the e8 continuum peak, and another embedded source may be indicated. This could explain the incomplete hourglass structure here.

As in the case of e2, a zone of depolarization seems to be present at the continuum peak, along the north-south direction. This is consistent with the pinch direction of

the hourglass-like morphology being along the elongated e8 dust ridge. Rotation associated with the e8 collapsing core was detected in the direction of P.A. $\sim 156°$ $(-24°)$ with CH_3CN (Zhang, Ho, & Ohashi 1998). In this scenario, the pinch direction of the hourglass-like B field is parallel to the plane of rotation. The rotation axis of the e8 collapsing core is then almost parallel to the B field threading the 870 μm dust ridge. Note that the rotation direction as traced in CH_3CN is still uncertain (Zhang, Ho, & Ohashi 1998). An accurate determination of the plane of rotation associated with the e8 collapsing core is needed to test if the larger scale B field controls the direction of accretion.

Although the plane of accretion (or the pinched angle of the hourglass) cannot be determined with certainty, the collapse signature was detected toward *e8* (Ho & Young 1996; Zhang & Ho 1997; Zhang, Ho & Ohashi 1998), consistent with the possible hourglass-like B field morphology. Furthermore, this collapsing core is inside the 0.08 pc scale dust ridge, as revealed with the $0.''7$ angular resolution B field morphology. Based on this morphology and the presence of *e4*, *e8*, *e1*, and *e3*, we suggest that the star formation process involves different stages of fragmentation, proceeding at different evolutionary timescales.

2.4.3   Estimate of the Strength of the B field

The B field strength can be estimated by comparing the gravitational force f_G with the B field tension f_B following Dotson (1996) and Schleuning (1998). The value of f_G at a distance R_G away from the center is given by

$$f_G = \frac{G\,M_R\,\rho}{R_G^2} = 5 \times 10^{-26} \frac{M_R}{100 M_\odot} \frac{n_{H_2}}{10^5\,\mathrm{cm}^{-3}} \left(\frac{R_G}{0.1\,\mathrm{pc}}\right)^{-2} \quad \frac{\mathrm{dyne}}{\mathrm{cm}^3}, \tag{2.1}$$

where M_R refers to the gas mass enclosed within a radius R_G, ρ is the mass density at R_G, and n_{H_2} is the gas volume number density. The f_B can be given by

$$f_B = \frac{1}{4\pi} \vec{B} \cdot \vec{\nabla} \vec{B} \sim \frac{B^2}{4\pi R_B} = 5 \times 10^{-26} \left(\frac{B}{\mathrm{mG}}\right)^2 \left(\frac{R_B}{0.5\,\mathrm{pc}}\right)^{-1} \quad \frac{\mathrm{dyne}}{\mathrm{cm}^3}, \tag{2.2}$$

where R_B is the radius of a magnetic flux tube, and B is the B field strength. Since the e2 and e8 cores are known to be in a collapse stage, we conclude that $f_G > f_B$.

An upper limit of B can then be derived. For the e2 collapsing core, M_R is estimated to be 220$M_\odot$ based on the 870 μm flux density within a radius of 1″ of the continuum peak. This is consistent with the proposed self gravitating mass of >160 $M_\odot$ (Ho & Young 1996) based on the kinematics of the NH_3 lines. R_G is 1″ (0.034 pc), and the mean n_{H_2} within R_G is 2.7×10^7 cm^{-3}. Assuming $R_G = R_B \simeq 0.034$ pc, the B field strength in the e2 core is therefore < 19 mG. In the e8 collapsing core, M_R is 94 $M_\odot$, and n_{H_2} is 1.2×10^7 cm^{-3} within a radius of 1″ centered on the peak position. The B field strength in the e8 core is therefore < 8 mG. Both of the upper limits of B are consistent with the lower limit of the larger scale $B_\perp$ field strength of 1 mG (Lai et al. 2001) estimated from the method proposed by Chandrasekhar & Fermi (1953).

2.4.4 Characteristic Length Scales

To analyze the interactions between B field, gravitational force and thermal force in star forming sites, we further calculate the following three length scales following Mouschovias (1991): First, the interplay between ambipolar diffusion and Alfvén waves is characterized by the Alfvén length scale λ_A. Second, the interplay between gravitational and thermal pressure forces is characterized by the thermal Jeans length scale $\lambda_{T,cr}$, following Bonnor (1956) and Ebert (1955; 1957). Third, the interplay between magnetic and gravitational forces is characterized by the critical magnetic length scale $\lambda_{M,cr}$. They can be calculated using the following equations:

$$\lambda_A = 8\frac{B}{\text{mG}}\left(\frac{n_{H_2}}{10^6\,\text{cm}^{-3}}\right)^{-1}\left(\frac{K}{3\times10^{-3}}\right)^{-1} \quad \text{mpc,} \tag{2.3}$$

$$\lambda_{T,cr} = 31\sqrt{\frac{T}{100\,\text{K}}\left(\frac{n_{H_2}}{10^6\,\text{cm}^{-3}}\right)^{-1}} \quad \text{mpc,} \tag{2.4}$$

and

$$\lambda_{M,cr} = 36\frac{B}{\text{mG}}\left(\frac{n_{H_2}}{10^6\,\text{cm}^{-3}}\right)^{-1} \quad \text{mpc.} \tag{2.5}$$

Here, the parameter k (Eq. (6f) in Mouschovias 1991), related to the mean collision time between an ionized and a neutral particle, is assumed to be 0.5 when we derive Eq. (3), which is within the most likely range given in the reference in their paper. The factor K is related to the cosmic ionization rate. We assume K

$= 3 \times 10^{-3}$ (Mouschovias & Morton 1991) following the ionization rate calculated by Nakano (1979). With the assumed k and K, the estimated fractional ionization rate is 3×10^{-9} for a number density of 10^7 cm^{-3}, which seems to be reasonable. T is the gas temperature, and $n_{\mathrm{H_2}}$ is the gas volume number density. B is the B field strength. Note that T is assumed to be 100 K in both the e2 and e8 dust ridges based on the analysis of the hot core lines by Zhang, Ho & Ohashi (1997). Since these natural length scales depend on $n_{\mathrm{H_2}}$ and B, they are calculated separately based on the detected continuum emission with the same assumption as in §3.1. In the 1.3 mm envelope, the $n_{\mathrm{H_2}}$ is the mean number density within a best-fit Gaussian centered on the peak, and B is the lower limit of 1 mG. In the 870 μm dust ridges, $n_{\mathrm{H_2}}$ is calculated within a radius of 1″, and B is the upper limit calculated in §4.3. The calculated natural length scales in the e2 and e8 cores are listed in Table 3.

The physical meaning of these length scales are explained clearly in Mouschovias (1991) and references therein. λ_{A} gives the lower limit of the scale at which the B field can sustain the structure. At the scale R< λ_{A}, the ambipolar diffusion between neutral and ionized particles is more efficient and the Alfvénic motion is less important. $\lambda_{\mathrm{T,cr}}$ gives the scale where the gravitational force is equal to the thermal pressure. If an object has a size scale R > $\lambda_{\mathrm{T,cr}}$, gravity can overwhelm the thermal pressure and collapse will start. $\lambda_{\mathrm{M,cr}}$ gives the upper limit of the scale where the cloud can be magnetically supported along the B field direction. In a region R> $\lambda_{\mathrm{M,cr}}$, there will be enough mass and therefore the material can collapse if there are no other supporting forces.

Correlation with the SMA e2 dust ridge

In the e2 dust ridge, the revealed B$_\perp$ morphology is clearly pinched with a radius of $\sim 0\rlap{.}''8$ near *e2*, comparable to the radius of the proposed rotating flattened structure of 1″ (Zhang & Ho 1997; Zhang, Ho, & Ohashi 1998) and the proposed ionized accretion disk of $\sim 0\rlap{.}''5$ (Keto & Klaassen 2008). The derived $\lambda_{\mathrm{T,cr}}$ is $\sim 0\rlap{.}''2$, suggesting that at $\sim 1''$, gravity will easily overcome the thermal pressure support if there are no other supporting forces. The scale where ambipolar diffusion starts to take place (λ_{A})

is $\sim 0\rlap{.}''2$ for the e2 dust ridge, consistent with the observed pinched $B_\perp$ field lines. Note that the revealed width of the depolarization zone near *e2* is narrow ($< 0\rlap{.}''5$), which is smaller than our synthesized beam. Higher angular resolution measurements with at least $0\rlap{.}''3$ resolution are needed to discriminate whether the depolarization is due to ambipolar diffusion, inefficient grain alignment or other mechanisms, such as geometrical effects. The calculated scale where the B field can sustain the structure against gravitational collapsing ($\lambda_{M,cr}$) is $0\rlap{.}''8$ along the field line. However, it is difficult to compare $\lambda_{M,cr}$ with the scale associated with the dust ridge, because the large scale (0.5 pc) $B_\perp$ field is twisted by $\sim 45°$ (Figure 2(a)) at $3''$ resolution. Observations with visibilities at both shorter and longer uv ranges are needed in order to link the $B_\perp$ in the core with the field in the envelope at the same wavelength. Note that the weak constraints on λ_A and $\lambda_{M,cr}$ result from the large range of possible B field values.

Correlation with the SMA e8 dust ridge

The dust continuum emission appears to be ridge-like, and the minor axis of the e8 dust ridge is approximately parallel to the 0.5 pc $B_\perp$ field direction. The deconvolved length of the e8 dust ridge along the minor axis is barely resolved, and we adopt an upper limit to the radius of $0\rlap{.}''3$ along the minor axis. This is consistent with the estimated $\lambda_{M,cr} < 0\rlap{.}''7$, and the estimated $\lambda_{T,cr}$ of $0\rlap{.}''3$. This suggests that thermal pressure is significant as compared to gravity and field tension at this scale. Along the major axis, the deconvolved size is $0\rlap{.}''9$, which is larger than $\lambda_{T,cr}$. Furthermore, ambipolar diffusion is expected to dominate at the scale $\lambda_A < 0\rlap{.}''2$ in e8. Hence we expect collapse and fragmentation to occur along the ridge. This is consistent with the revealed hourglass-like B field morphology associated with the e8 collapsing core at $0\rlap{.}''7$ resolution and the smooth B field morphology in the envelope at $3''$ resolution. These results in the e8 core seem to be consistent with the ambipolar diffusion model (Mouschovias & Morton 1991) and suggest that the formation of the dust ridge is influenced by the B field in the envelope.

Connection between the BIMA 0.5 pc scale envelope and the SMA dust ridges

The main difference between the 0.5 pc envelope and the dust ridges is in the large contrast in the derived value for $n_{\mathrm{H_2}}$. Nevertheless, the agreement in the estimates of λ_A and $\lambda_{M,cr}$ for the envelope and the ridge is very good, because of the lower estimates of B in the envelope. This implies that the B field support is adequate till the scale of $0\rlap{.}''2-1''$. The derived value of $\lambda_{T,cr}$ is larger for the envelope than for the ridge, but still smaller than the measured size of the envelope. This is also consistent with the proposed scenario that the B field provides the support against gravity at the 0.5 pc scale.

2.4.5   Role of $B_\perp$ from Envelope (0.5 pc) to Collapsing Cores (0.02 pc)

The structure of the B field varies with different size scales (Figure 6).

At the $0\rlap{.}''7$ (0.02 pc) scale, the B field in the W51 e2 and e8 cores is not uniform. In both the e2 and e8 cores, the hourglass-like morphology suggests that at the 0.02 pc scale, gravity dominates over the B field. Our estimated collapsing M_{gas} is on the order of 100 $M_\odot$ (see §4.3) in both the e2 and e8 cores, which is roughly consistent with M_{gas} estimated in the local collapsing scenario (Ho & Young 1996; Sollins et al. 2004). The cores are therefore in the supercritical phase.

At the 0.5 pc scale, the B field in the envelope is uniform throughout the e2 and e8 dust ridges, except to the north-west of e2. Due to the small dispersion of the measured P.A.s of the polarization in the envelope, the B field is suggested to dominate over the turbulence with a strength of $\gtrsim 1$ mG by Lai et al. (2001). We further suggest that the envelope is subcritical. The reasons are: 1. B field dominates over turbulence in the envelope. 2. B field is apparently sufficient to support the envelope against gravity (§4.4.3). 3. The collapse is apparent only locally in e2 and e8 with M_{gas} in the order of 100 $M_\odot$, so that the envelope is stable.

Based on the MHD simulations (Klessen et al. 2000), turbulent motions (cf. Mac

Low & Klessen 2004) can produce an elongated envelope and can sustain the envelope from collapse. However, such elongated structures would not exhibit a preferred alignment with the B field (Heitsch et al. 2001), as it is seen here. The measured B field structures from 0.02 pc to 0.5 pc do not show an obvious necessity for turbulent support. Instead, the cloud morphology, sizescale, and B field geometry are consistent with *magnetic fragmentation* via ambipolar diffusion (Mouschovias & Morton 1991; Lizano & Shu 1989; Shu et al. 2004).

2.4.6   Comparison with other star formation sites

Because the collapse signatures in the W51 e2 and e8 regions are clearly detected, and the UCHII regions are still relatively compact and weak, they are in an earlier evolutionary stage as compared with the other massive star formation sites, such as G5.89−0.39 (Tang et al. 2009). In G5.89-0.39, the B field is suggested to be overwhelmed by the turbulent motions from the UCHII expansion and the molecular outflows. A more complex $B_\perp$ morphology is detected (Tang et al. 2009) with a spatial resolution of 0.02 pc. In contrast to G5.89−0.39, the $B_\perp$ morphologies are hourglass-like in both of the W51 e2 and e8 regions at the 0.02 pc spatial resolution, but much smoother at the 0.5 pc scale. This comparison of G5.89-0.39 and W51 e2/e8 with the same spatial resolution indicates that the role of the B field varies with the evolutionary stages of the central sources.

In the low mass star formation region NGC 1333 IRAS 4A, the hourglass shape is observed on a scale of 2400 AU (0.01 pc) and $M_{\rm gas}$ is $\sim$1.2M$_\odot$ (Girart, Rao, & Marrone 2006). In comparison, the hourglass $B_\perp$ structure detected in W51 e2 is on the scale of $\sim$ 0.03 pc ($1''$), and the mass involved is $\sim$ 200 M$_\odot$. The consistency of the directions of the ionized flow and the pinched field further suggests that the stars are formed with similar mechanisms, i.e. material is accreted through a flattened structure. The difference is that the scale and the mass involved are much larger in the massive star forming regions. At the time of publication of this paper, additional observational evidence of an hourglass B field morphology in the massive star forming core G31.41+0.31 is presented in Girart et al. (2009). This further supports the

proposed similar formation mechanism as in the low mass case.

However, the massive star forming sites are much further away than the low mass regions in general. For example, W51 e2 is at 7 kpc, ~ 23 times further away than NGC 1333 IRAS 4A. Observations with higher spatial resolution are thus needed for the massive star forming regions. The closest massive star forming site is Orion BN/KL. Source I in Orion BN/KL is suggested to be in an early stage of massive star formation due to the weak and compact free-free emission (Plambeck et al. 1995). Source I is also suggested to harbor an ionized accretion disk (Reid et al. 2007). The $B_\perp$ at 0.5 pc starts to exhibit a larger scale hourglass-like morphology (Schleuning 1998). The existence of the ionized disk, the uniform large scale $B_\perp$ geometry and the compact free-free source all suggest that it is an analog of W51 e2/e8, but at a much closer distance. The comparison between w51 e2/e8 and Source I in Orion BN/KL may provide a clue of the $B_\perp$ morphology at even higher physical resolutions.

In W51 e2/e8, we found two supercritical cores at 0.03 pc within a subcritical envelope at 0.5 pc (§4.5). At a larger scale, DR21 MAIN is suggested to have started undergoing a gravitational Suggested by the same author, in the outer part (~ 1 pc away from the center), the cloud is still magnetically supported. That the collapsing cores formed inside a magnetically supported cloud as in W51 e2/e8, is therefore not a special case. As indicated by Vaillancourt (2009), observations of B field at the larger scales are needed to test the magnetically controlled star formation process. Shorter spacing visibilities of the SMA are needed to directly compare the field morphology of the cores with the envelope at the same wavelength of 870 μm. In this paper, we have demonstrated that smaller scale $B_\perp$ maps provide crucial information about the $B_\perp$ field by resolving the star forming cores and by linking the field morphology with the kinematics of the molecular cloud.

2.5   Conclusion and Summary

To study the role of the B field in the star forming cores, we have observed and analyzed the $B_\perp$ morphologies, inferred from the linearly polarized dust continuum emission, in the massive star forming site W51 e2/e8 by using the Submillimeter

Array (SMA). We further compare the $B_\perp$ morphologies in the dust ridges with the one in the envelope. Three different natural length scales, namely the Alfvén length scale λ_A, thermal Jeans lengths scale $\lambda_{T,cr}$, and the magnetic length scale $\lambda_{M,cr}$, are calculated and compared to the dust ridges and envelope. Here are the summary and conclusion.

1. The 870 μm continuum and its polarization in W51 e2 and e8 are resolved with an angular resolution of $0''.7$ as observed with the SMA. The polarization in both e2 and e8 exhibit complex structures. In comparison, the polarization at 1.3 mm observed at $3''$ resolution with the BIMA revealed a uniform morphology across e2 and e8, with almost no polarization detected near the peak position in e2 (Lai et al. 2001). We conclude that low or no polarization near the emission peaks heretofore seen in the star formation regions is likely due to a more complex underlying $B_\perp$ morphology (§3.2).

2. In the e2 dust ridge, the inferred $B_\perp$ morphology is hourglass-like near the collapsing core, with its pinched direction parallel to the direction of the ionized accretion flow as traced by H53α (Keto & Klaassen 2008). The $B_\perp$ here shows a similar morphology as in the low mass star formation case NGC 1333 IRAS 4A. However, the mass included in this core is $\sim$200 times larger. This result shows that the B field in the e2 collapsing core plays a similar role as in the low mass star formation regions (§4.1). Higher angular resolution observations are required to test if the hourglass-like $B_\perp$ morphology is preserved at smaller scale.

3. The e8 dust ridge is perpendicular to the 0.5 pc scale $B_\perp$ direction as revealed with the BIMA, which suggests that the B field at 0.5 pc controls the forming process of the dust ridge. The $B_\perp$ along the dust ridge exhibits a systematic deviation from the $B_\perp$ at 0.5 pc scale. Associated with the e8 collapsing core, the hourglass $B_\perp$ morphology is more clearly detected, suggesting that the collapsing core is formed locally inside a flattened structure (§4.2).

4. The exhibited hourglass-like $B_\perp$ morphologies in the e2 and possibly the e8 dust

ridges are consistent with the proposed local collapse (Ho & Young 1996; Sollins et al. 2004) instead of the global collapse (Rudolph et al. 1990). This indicates that both the e2 and e8 cores are in a supercritical stage (gravity dominating over the B field) at the 0.02 pc scale. In contrast, the B field morphology of the 0.5 pc envelope is uniform across the e2 and e8 dust ridges and strong (≥ 1 mG). We further propose that the B field in the 0.5 pc scale envelope is subcritical (B field dominating the gravity). That the supercritical cores formed inside a subcritical envelope seems to support a *magnetic fragmentation* scenario (Mouschovias & Morton 1991; Lizaro & Shu 1989; Shu et al. 2004), suggesting that ambipolar diffusion plays a key role in the evolution of the envelope at this stage (§4.5).

Appendix

In order to test how significantly the measured B field deviates from a purely radial field, we have analyzed the differences, δ, between position angles (P.A.s) of the measured B field lines and the corresponding hypothetical radial field lines. The radial field lines are derived from their relative positions (center of each P.A.) with respect to the origin, which is defined as the 870 μm peak in e2. Due to the limited detected data points, we do not apply this statistical analysis to e8. All the data considered are above 3 $\sigma_{I_{\mathrm{p}}}$. We have excluded the 6 data points in the north-west extension, which correspond to e2 pol NW. The distribution of δ apparently deviates from a Gaussian (Figure A1(Left-panel)). When, nevertheless enforcing a Gaussian fitting, the derived mean μ is 1.6° and the standard deviation σ is 14°, which is larger than the mean measurement uncertainty $\sigma_{\mathrm{mean,PA}}$ of 6.9°.

To quantify the deviation from a Gaussian, we further apply a Kolmogorov-

Smirnov (KS) test to δ. As null hypothesis we assume that the distribution of δ is normal with $\sigma_{\mathrm{mean,PA}}$ and $\mu = 0°$. This mimics an observation of a radial field with our observed measurement uncertainty $\sigma_{\mathrm{mean,PA}}$. The measurement uncertainties in each P.A. are propagated with a Monte-Carlo (MC) simulation when deriving δ and applying the KS test. In the MC simulation we also allow for a shift of $\pm 0''\!.1$ of the origin of the radial field. Figure A1 (Right-panel) shows the cumulative distributions which are used for the statistic measure in the KS test. As a result, the probability of the measured field being radial is 20%. For the $\pm 1 \sigma_{\mathrm{mean,PA}}$ error bounds, the probability of being radial is less than 5%. Therefore, the null hypothesis can be rejected. Our test favors the existence of a non-radial B field.

δ as a function of P.A. is presented in Figure A2. If we separate the segments according to the depolarization zones (marked as arrows in Figure A2), there are always segments with δ larger than 3 $\sigma_{\mathrm{mean,PA}}$ in each zone. This suggests that deviations are not prevalent in certain directions, but rather grouped together and interleaved with depolarization zones, as we would expect from an hourglass field morphology.

Table 2.1.   SMA dust polarization at 870μm in e2

$\triangle$x	$\triangle$y	I	$P(\%)$	I_{p}	$\phi(°)$
-1.2	2.4	0.32	5.9 ± 1.1	19	66 ± 6
-1.5	2.4	0.29	6.6 ± 1.3	19	61 ± 6
-0.6	2.1	0.24	7.4 ± 1.5	18	-71 ± 6
-0.9	2.1	0.36	4.4 ± 1.0	16	-75 ± 7
0.3	1.8	0.31	4.8 ± 1.2	15	-75 ± 7
0.0	1.8	0.45	4.2 ± 0.8	19	-82 ± 6
-0.3	1.8	0.41	4.9 ± 0.9	20	-89 ± 6
-0.6	1.8	0.43	3.7 ± 0.9	16	-84 ± 7
-0.9	1.8	0.43	3.0 ± 0.9	13	-70 ± 8
0.6	1.5	0.22	5.1 ± 1.7	11	-61 ± 10
0.3	1.5	0.66	2.9 ± 0.6	19	-74 ± 6
0.0	1.5	0.96	2.3 ± 0.4	22	-87 ± 5
-0.3	1.5	0.82	2.2 ± 0.5	18	79 ± 6
0.3	1.2	1.33	0.9 ± 0.3	12	-71 ± 9
0.0	1.2	1.71	0.7 ± 0.2	12	-83 ± 9
-0.6	1.2	1.23	1.3 ± 0.3	16	19 ± 7
-0.9	1.2	0.56	3.2 ± 0.7	18	-3 ± 6
-0.3	0.9	2.67	0.6 ± 0.2	16	17 ± 7
-0.6	0.9	1.71	1.4 ± 0.2	24	9 ± 4
-0.9	0.9	0.82	2.8 ± 0.5	23	-5 ± 5
-1.2	0.9	0.21	7.5 ± 1.8	16	-18 ± 7
0.9	0.6	0.30	4.7 ± 1.3	14	18 ± 8
0.6	0.6	1.30	1.0 ± 0.3	13	37 ± 8
-0.3	0.6	2.33	0.6 ± 0.1	14	6 ± 8

Table 2.1 (continued)

$\triangle$x	$\triangle$y	I	$P(\%)$	I_{p}	$\phi(°)$
-0.6	0.6	1.55	1.1 ± 0.2	17	-2 ± 6
-0.9	0.6	0.70	2.7 ± 0.6	19	-22 ± 6
0.9	0.3	0.20	7.5 ± 1.9	15	32 ± 7
0.6	0.3	0.81	2.7 ± 0.5	22	48 ± 5
0.3	0.3	1.75	0.8 ± 0.2	14	65 ± 8
-0.9	0.3	0.32	3.7 ± 1.1	12	-27 ± 9
0.6	0.0	0.22	8.1 ± 1.7	18	55 ± 6
0.3	0.0	0.60	2.5 ± 0.6	15	80 ± 7
0.0	0.0	0.95	2.1 ± 0.4	20	-79 ± 5
-0.3	0.0	0.76	1.7 ± 0.5	13	-80 ± 9
0.0	-0.3	0.23	6.0 ± 1.6	14	-81 ± 8
-3.6	-2.4	0.22	5.0 ± 1.7	11	-17 ± 10

Note. — $\triangle$x & $\triangle$y: offsets in arcsecond from Right Ascension (J2000) = $19^{\mathrm{h}}23^{\mathrm{m}}43^{\mathrm{s}}.95$, Declination (J2000) = $14°30'34''.00$. I: intensity of the Stokes I component in Jy beam^{-1}. $P(\%)$: polarization percentage, derived from the ratio I_{p}/I. I_{p}: the polarized intensity in mJy beam^{-1}. ϕ: position angle from the north to the east. Listed data points are within the red box associated with *e2* in Figure 2. All listed points are above 3 $\sigma_{I_{\mathrm{p}}}$.

Table 2.2.   SMA dust polarization at 870μm in e8

$\triangle$x	$\triangle$y	I	$P(\%)$	I_{p}	$\phi(°)$
-0.6	-5.1	0.28	4.0 ± 1.3	11	76 ± 10
-1.2	-5.4	0.64	2.2 ± 0.6	14	-1 ± 8
-1.5	-5.7	0.22	5.8 ± 1.8	13	-1 ± 9
-0.9	-6.0	1.57	0.7 ± 0.2	11	-70 ± 10
-1.5	-6.6	0.27	7.5 ± 1.4	20	-21 ± 5
-1.5	-6.9	0.39	3.8 ± 1.0	15	-19 ± 7
-1.2	-7.2	0.55	2.0 ± 0.7	11	36 ± 10
-1.2	-7.5	0.42	3.3 ± 0.9	14	59 ± 8
1.5	-8.7	0.26	4.2 ± 1.4	11	6 ± 10
-1.8	-8.7	0.24	5.0 ± 1.6	12	-33 ± 9
-2.1	-8.7	0.23	8.0 ± 1.7	18	-40 ± 6
-2.1	-9.0	0.23	4.7 ± 1.5	11	-33 ± 10

Note. — Identical notation as in Table 1. $\triangle$x and $\triangle$y are with respect to the same coordinate as in Table 1. Listed data points are all within the red box associated with *e8* in Figure 2.

Table 2.3.   Derived parameters in e2 and e8

Parameters	units	e2		e8	
		BIMA[a]	SMA[b]	BIMA[a]	SMA[b]
$\theta_{maj} \times \theta_{min}$	$''$	3.6×2.6	0.9×0.8	5.0×2.2	0.9×0.3
$M_{\rm R}$	$M_{\odot}$	-	220	-	94
$n_{\rm H_2}$	cm^{-3}	1.5×10^6	2.7×10^7	7.6×10^5	1.2×10^7
B	mG	≥ 1	<19	≥ 1	<8
$\lambda_{\rm A}$	mpc	≥ 5	<6	≥ 11	<5
	$('')$	(≥ 0.2)	(<0.2)	(≥ 0.3)	(<0.2)
$\lambda_{\rm T,cr}$	mpc	25	6	36	9
	$('')$	(0.8)	(0.2)	(1.1)	(0.3)
$\lambda_{\rm M,cr}$	mpc	≥ 24	<25	≥ 47	<24
	$('')$	(≥ 0.7)	(<0.8)	(≥ 1.4)	(<0.7)

[a]The derived mean $n_{\rm H_2}$ is based on a Gaussian fit of the 1.3 mm continuum emission toward the peak. All the natural length scales depend on this $n_{\rm H_2}$.

[b]The derived mean $n_{\rm H_2}$ is within a radius of $1''$ centered on the 870 μm continuum peak, where the collapsing signatures were clearly revealed with the molecular lines. All the natural length scales and the upper limit of B depend on this $n_{\rm H_2}$.

Note. — θ_{maj} and θ_{min} refer to the major and minor axis of the deconvolved size, respectively. They are determined by a best-fit Gaussian of the continuum emission centered on the peak. $M_{\rm R}$ refers to the estimated $M_{\rm gas}$ from the continuum emission within a radius of $1''$ centered on the peak position. The lower limit of the B field strength of 1 mG is adopted from Lai et al. (2001). Characteristic length scales $\lambda_{\rm A}$, $\lambda_{\rm T,cr}$ and $\lambda_{\rm M,cr}$ are calculated assuming T = 100 K. Note that the weak constraints on $\lambda_{\rm A}$ and $\lambda_{\rm M,cr}$ result from the large possible range of B field strength.
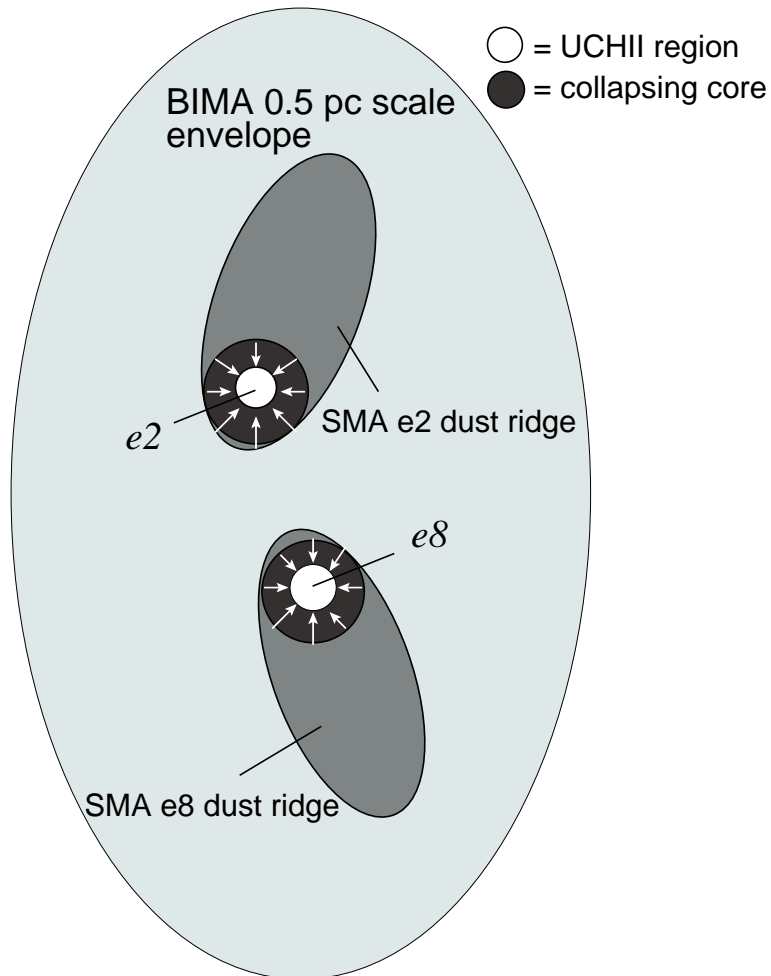
Figure 2.1 Schematic cartoon of structures in W51 e2/e8. *e2* and *e8* refer to the UCHII region e2 and e8, respectively.

Figure 2.2 (a) Polarization map observed with BIMA adopted from Lai et al. (2001). Contours are the 1.3 mm continuum strength of -3, 3, 5, 10, 20, 30, ..., 90, 100, 110 $\times$ 27 mJy beam^{-1}, where the size of the synthesized beam is $2\rlap{.}''7 \times 2\rlap{.}''0$. The cyan stars mark the UCHII regions. The offset is in arcsecond with respect to Right Ascension (J2000)=$19^h23^m43^s$.95, Declination (J2000)=$14°30'34\rlap{.}''00$. Red boxes indicate the regions presented in panel (c) and (d). (b): SMA 870 μm continuum emission in W51 e2/e8. Contours are the 870 μm continuum strength at -6, -3, 3, 6, 12, 24, 36, 48, 60 $\times$ 60 mJy beam^{-1}, where the beam size is $0\rlap{.}''7 \times 0\rlap{.}''6$. All the other symbols are identical to the ones in (a). (c): SMA polarization in W51 e2. Contours are the 870 μm continuum strength at -4, -2, 2, 4, 6, 8, 10, 15, 20, ..., 55, 60 $\times$ 60 mJy beam^{-1}. Black and red segments represent the polarization with its length proportional to the polarized percentage at 2 to 3 $\sigma_{I_{\mathrm{p}}}$ and above $3\sigma_{I_{\mathrm{p}}}$, respectively. Solid and unfilled triangles mark the positions of the H$_2$O (Genzel et al. 1981) and (J,K) = (9,6) NH$_3$ (Pratap et al. 1991) masers, respectively. All the other symbols are identical to the ones in (a). (d) SMA polarization map in W51 e8. All the symbols and contour levels are identical to the ones in (c). All images shown have been corrected for the effect of primary beam attenuation. In each panel, the synthesized beam is plotted as a black ellipse at the lower-left corner. In panel (a), (c) and (d), the polarized intensity is shown in color scale with strength indicated by the wedge on the right in units of mJy beam^{-1} (mJy/B).
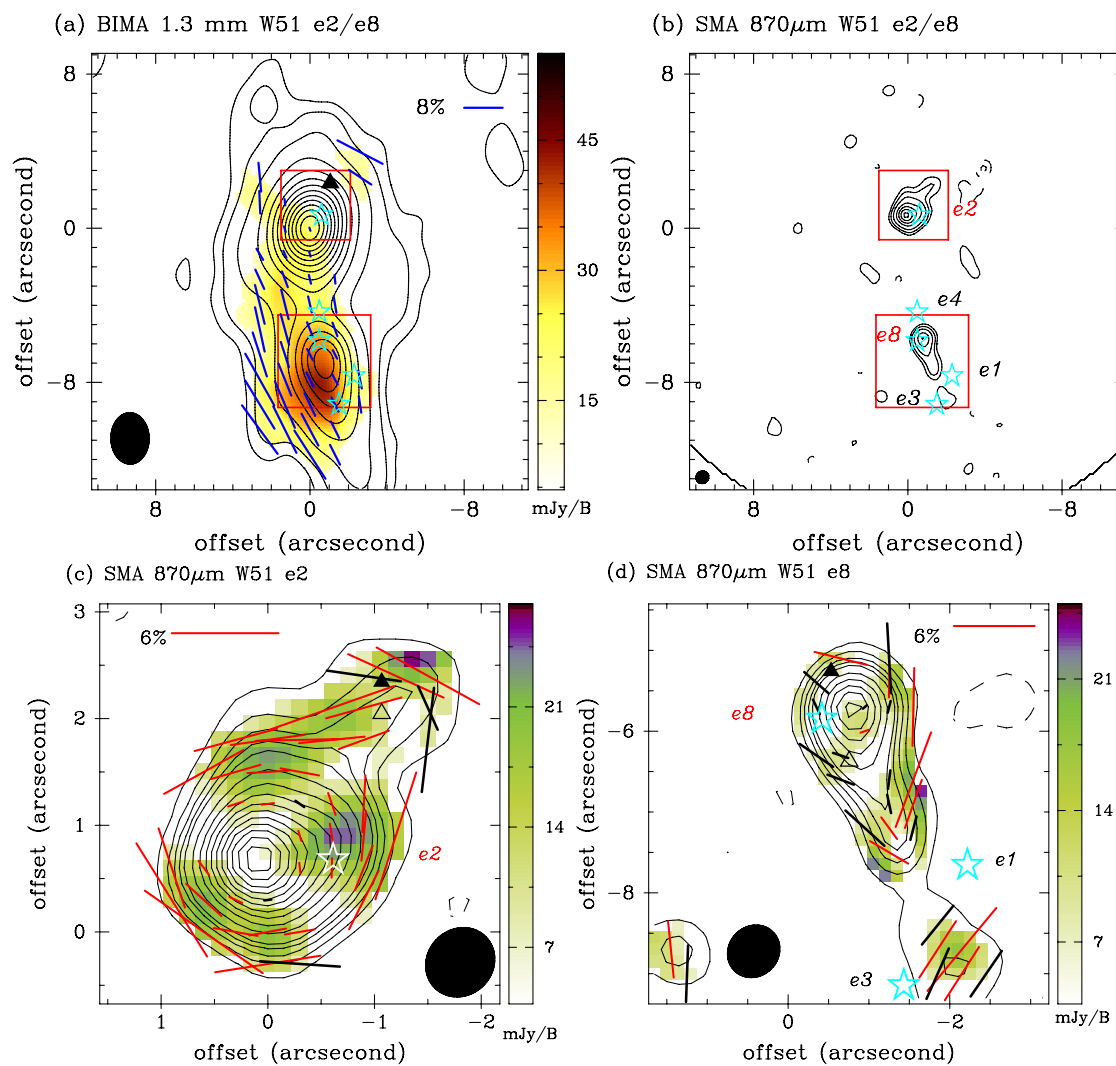
Figure 2.2 –continued..
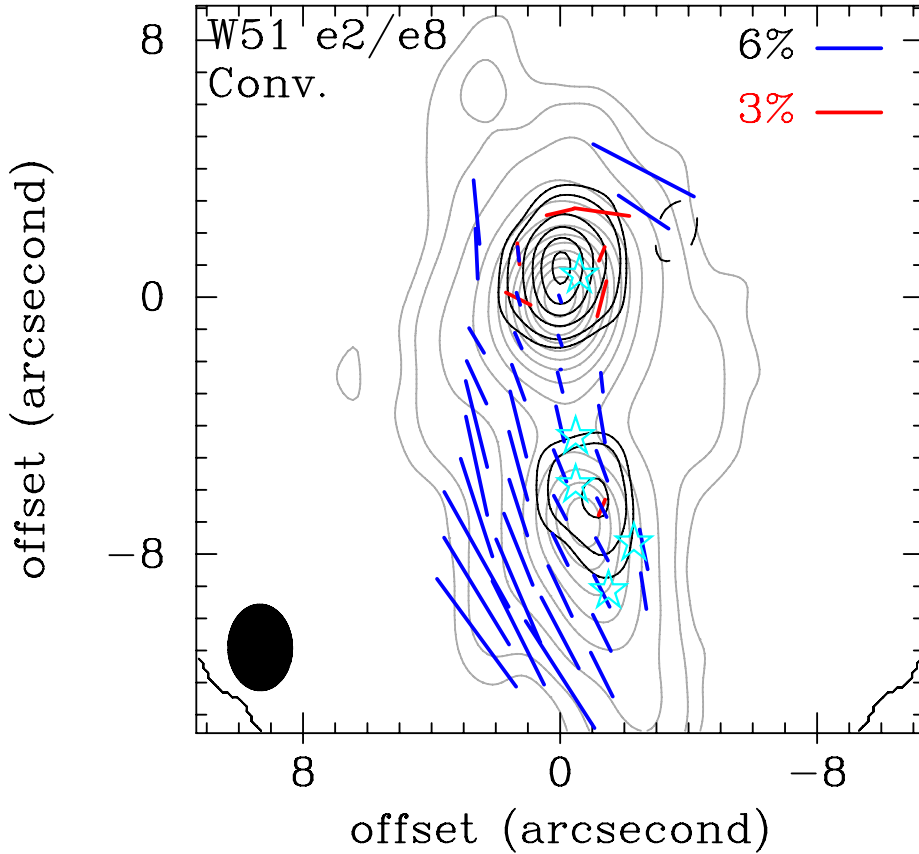
Figure 2.3 Polarization map of the SMA results (red segments) at 870 μm restored with the BIMA synthesized beam. BIMA polarization at 1.3 mm is shown in blue segments. The synthesized beam size is $2''7 \times 2''0$ with a P.A. of $1°$. The black contours represent the SMA 870 μm continuum emission after restoring to the BIMA resolution with contours of $-3, 3, 5, 10, 15, 20, 25 \times 0.3$ Jy beam^{-1}. The grey contours represent the BIMA 1.3 mm continuum emission with strengths as shown in Figure 2. All polarization vectors plotted are above $3\sigma_{I_\mathrm{p}}$. All the other notations are identical to the ones in Figure 2. The slight offset between the SMA and BIMA maps is most likely due to missing short spacing information in the SMA data, being insensitive to structures larger than $8''$.
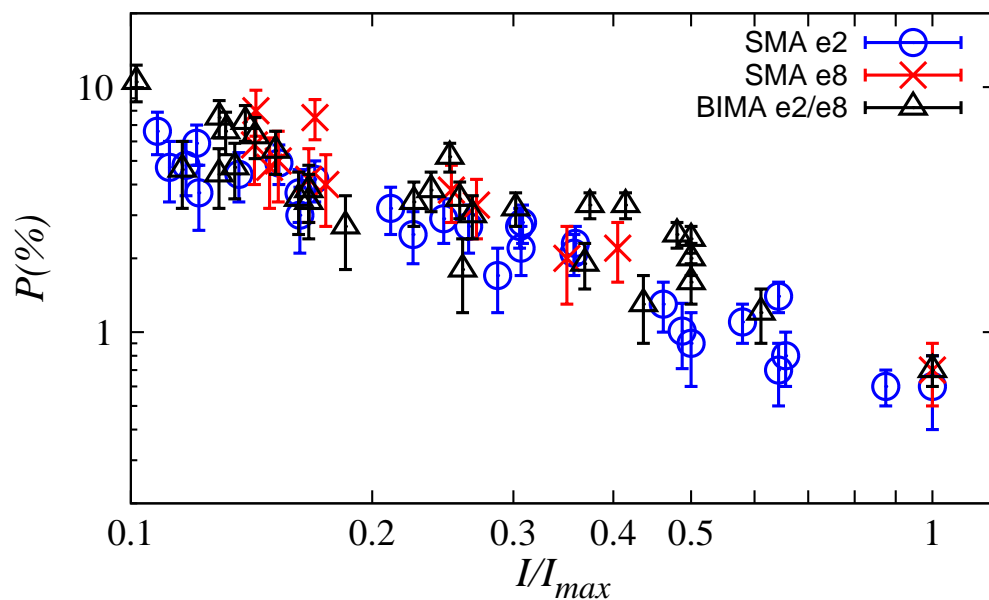
Figure 2.4 Plot of polarization percentage, $P(\%)$, versus normalized intensity (I/I_{max}). The blue circles, red crosses, and black triangles are SMA results for e2, e8 and BIMA results for both e2 and e8, respectively. All the plotted data are above $3\sigma_{I_p}$.
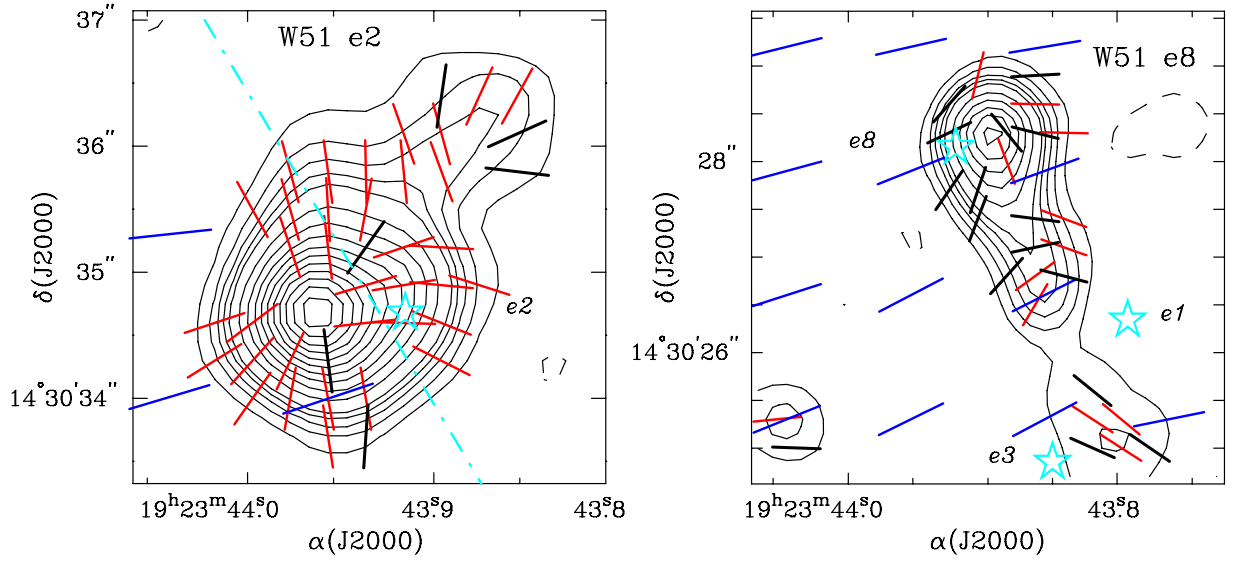
Figure 2.5 Left-panel: B field maps in W51 e2 with S/N ratio between 2 to 3 σ_{I_p} (black segments) and >3 σ_{I_p} (red segments), and 870 μm continuum emission in black contours. The dot-dash cyan segment marks the direction of the ionized accreting flow by Keto & Klaassen (2008). Blue segments are the inferred B field direction from the BIMA. The magnetic field segments (all of equal length) are rotated by 90° with respect to the polarization segments. Right-panel: B field map in W51 e8. All the symbols are identical to the ones in the left-panel. All the contours are plotted with the same level as in Figure 2(c) and 2(d) for left-panel and right-panel, respectively. Note that even at 2 to 3 σ_{I_p}, the B field directions are varying in a coherent manner. Hence the trends are significant.
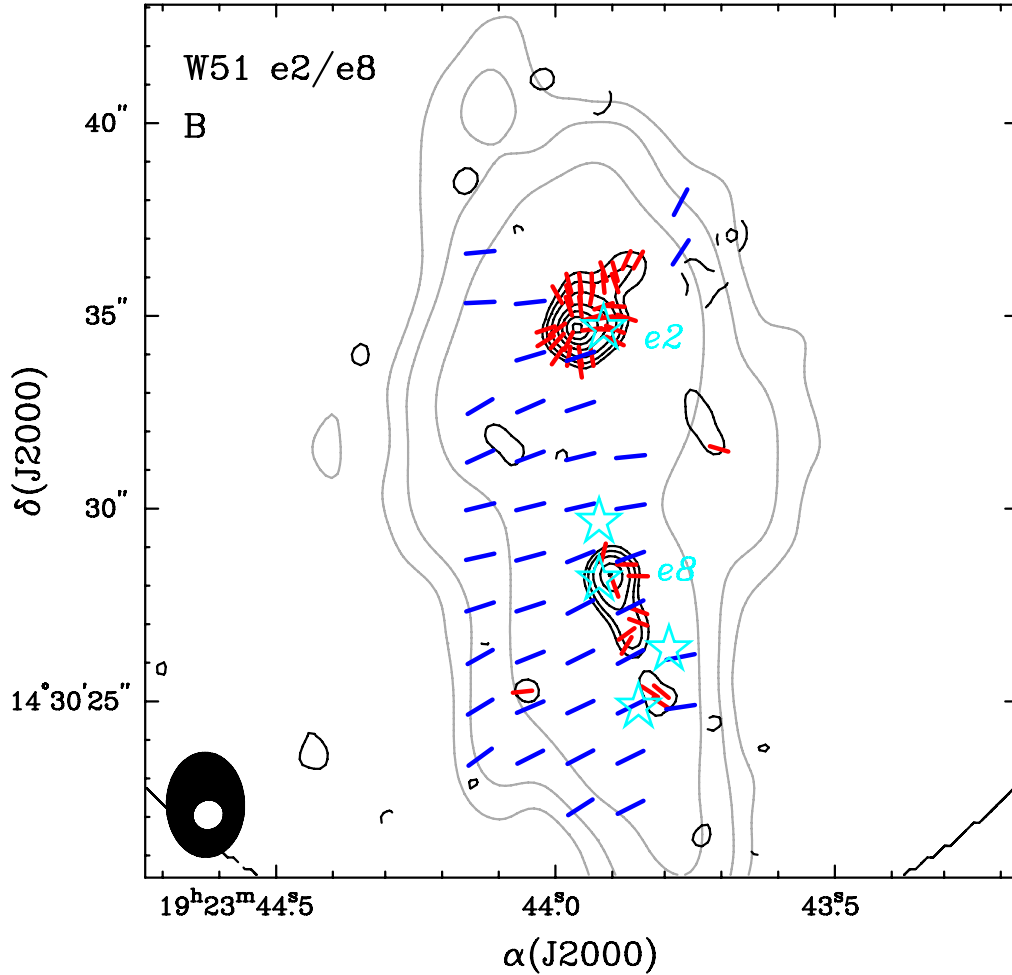
Figure 2.6 B field maps of W51 e2/e8 from the SMA (red segments) at 870 μm and BIMA (blue segments) at 1.3 mm. The black and grey contours represent the strengths of the continuum emission at 870 μm and at 1.3 mm, respectively. The black contours are plotted in the same levels as in Figure 2(b), and grey contours plotted are 3, 5, 10 $\times$ 27 mJy beam^{-1}. The other symbols are identical to the ones in Figure 2. The synthesized beams of the SMA and BIMA are plotted in the lower-left corner as white and black ellipses, respectively.
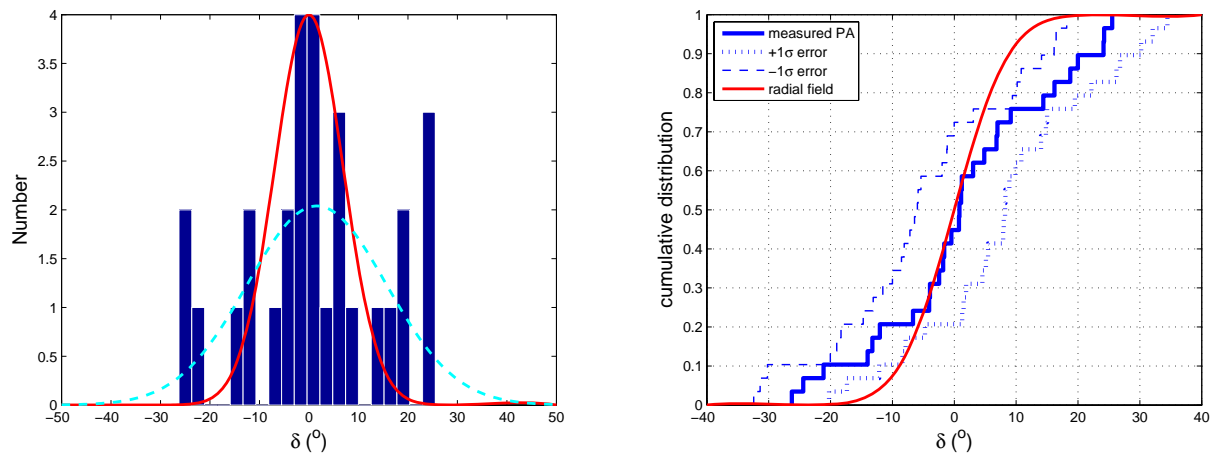
Figure 2.7 Left-panel: Histogram of the differences δ between the measured P.A. and a radial field. The cyan dashed curve is the enforced fitted Gaussian to the measurement with the resultant standard deviation $\sigma=14°$ and mean $\mu=1.6°$. The red solid curve is the normal distribution with $\sigma = \sigma_{\mathrm{mean,PA}}=6.9°$, which is the mean uncertainty of the measurement. Right-panel: Cumulative distribution of δ (solid blue line). The red curve marks the cumulative normal distribution with $\sigma_{\mathrm{mean,PA}}$. The $\pm$ 1 $\sigma_{\mathrm{mean,PA}}$ error bounds from the MC simulation, including measurement uncertainties and the shift of the center of the radial field, are also shown.
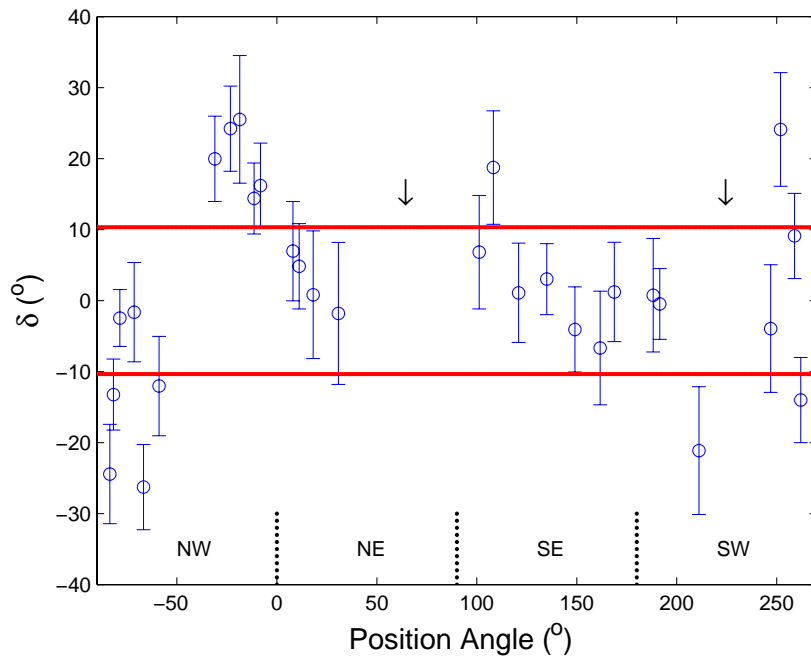
Figure 2.8 Plot of position angle versus δ. The red lines mark the 3 $\sigma_{\mathrm{mean,PA}}$ bounds. The black arrows mark the depolarization zones around P.A.s of $60°$ and $220°$, $\sim$ parallel to the maximum velocity gradient in the H53α line. The areas with respect to the 870 continuum peak are marked as NW, NE, SE and SW, which correspond to the north-west, north-east, south-east and south-west, respectively. There are always $\delta > 3$ $\sigma_{\mathrm{mean,PA}}$ in the areas separated by the depolarization zones.

Chapter 3

field geometry in infall disk/ring system W51 North

Tang, Ya-Wen, & Ho, Paul T. P. et al.

ABSTRACT

We present the observed dust continuum at wavelengths of 870 μm and its linear dust polarized emission in the massive star forming core W51 North:dust. The dust core is resolved into six clumps, and five clumps are aligned nearly in the major axis of the dust ridge. The magnetic field in the plane of sky ($B_\perp$), as inferred from the linear polarized emission, is detected and resolved in these clumps. While the $B_\perp$ in four clumps appears to have similar position angles, the $B_\perp$ in the clump near the continuum peak appears to be twisted. The clump in the west of the peak has a very different B field morphology, which is fan-like. As compared with the other collapsing cores, W51 North:dust appears to be in a stage where the fragmentation has started,

and sources at different evolutionary stages have been revealed, such as several O stars in the continuum free region, a very compact HII region and a protostar candidate. A more detail model considering the rotating and inclination angle of an hourglass-like B field is needed to interpret the results more quantitatively.

3.1   Introduction

High angular resolution observations of the submillimeter (submm) continuum emission are powerful to trace the star forming regions, because at submm, the continuum is mostly from the thermal dust emission and is optically thin. The dust grains are aligned with B field in most cases (Lazarian 2007). Furthermore, due to the difference in emissivities along the major and minor axes of the elongated dust grains, the continuum emission can be partly polarized. The morphology of magnetic field projected in the plane of sky ($B_{\perp}$) can be inferred by rotating $90°$ of the detected polarization.

$B_{\perp}$ morphologies have been observed toward several star forming regions with high angular resolutions, typically a few arcseconds. If B field lines in the star forming cores are anchored to accretion disks, the field lines will be dragged inward and form an hourglass-like morphology. Among the resolved star forming cores, the hourglass-like $B_{\perp}$ morphologies have been seen toward both low-mass (NGC 1333 IRAS4A by Girart et al. 2006) and massive (G31.41+031 by Girart et al. 2009 and W51 e2/e8 by Tang et al. 2009) star forming regions. As discussed by these authors, this similarity in the observed $B_{\perp}$ morphologies supports the notion that massive stars are formed through similar processes as in the low mass cases, i.e. via accretion. Of course, since we only detect the $B_{\perp}$ projected morphology, the observed structures are highly dependent on the inclination angle of the system along the line of sight. Assuming dust grains are all aligned with B field, Aitken et al. (2002) have shown that the projected B field morphology can vary significantly in different field geometry of the system, such as being purely axial, azimuthal, hourglass-like, or twisted due to rotation. To test if massive stars are formed through accretion, more observations toward collapsing cores are required, especially when the astronomical sources are different from source

to source.

W51 North is a good candidate to study the massive star formation processes. It has strong dust emission at mm wavelengths, which increases the possibilities of the detection of polarization due to the low polarization percentage P(%), typically a few percent, in star forming regions. The infall motions of the molecular cloud core have been detected in the SO_2 (Sollins et al. 2004) and the CN (Zapata et al. 2008) lines. The very faint thermal cm free-free continuum (< 1 mJy; Zhang, Ho, & Ohashi 1997) and the absence of high-velocity gas detected in CS 3-2 (Zhang et al. 1998), suggest that this source is probably in an extremely early evolutionary stage (protostars).

W51 North is a complex of maser sources and lies within the HII region complex G49.5-0.4 in W51 A, east of the W51 giant molecular cloud. It is located $6-8$ kpc away in the Sagittarius spiral arm (Genzel et al. 1981; Imai et al. 2002). In this paper, we adopt a distance of 7 kpc. This region is also known as W51 IRS2 as it is a strong infrared source with $L_{total} \sim 2.8 \times 10^6\ L_\odot$ within $14''$ (Erickson & Tokunaga 1980), which makes it one of the most luminous massive star-forming regions in our Galaxy. Also associated with W51 IRS2 are the edge-brightened cometary or shell-like HII region W51d (Gaume, Johnson, & Wilson 1993; labelled as IRS2d in this paper) and the ultracompact HII (UCHII) region W51d2 (Wilson, Gaume, & Johnston 1991).

Observed with $2''$ resolution , Zhang, Ho & Ohashi (1997) found that the continuum emission at wavelengths of 2 mm appears to be outside the projected boundary of the 1.3 cm continuum, and designated this 2 mm continuum source as W51 North:dust. Since the presented 870 μm continuum (see §4.2) is tracing similar region as 2 mm, we follow the denotation of W51 North:dust in this paper. Molecular emission is from a large ($\sim 4 \times 10^4$ AU) hot core with the excitation temperature of 100-200 K (Zhang et al., 1998). With an angular resolution of $0''.4$, Zapata et al. (2009) found an infalling ring-like structure with the SO_2 emission line with a deconvolved size of $1''.8 \times 1''.2$. At the center of the molecular ring is the "dominant center", named by Schneps et al. (1981), where the strongest H_2O, OH and SiO masers were found. The molecular outflow traced by SiO 5-4 was detected at a position angle (P.A.) of $150°$ (Zapata et al 2009). Eisner et al. (2002) and Imai et al. (2002) proposed an outflow at a P.A. of $105°$ to $140°$, which is instead traced by the proper motions of

H_2O masers. Both outflows are centered on the "dominant center".

Based on the mid-infrared morphology and spectroscopic observations, Okamoto et al. (2001) found one embedded protostar candidate OKYM 1, also called KJD 3 (Kraemer et al. 2001), at $1''$ to the north-east of "dominant center". Reported by the same authors, source OKYM 1 has deep silicate absorptions and has strong peaks at 8 and 12 μm, and there is no radio continuum detected, suggesting that it is a "protostar" candidate. Three O stars surrounding the W51 North region were identified by using the mid-infrared spectra by Okamoto et al. (2001). This region is therefore a very active star forming complex which several regions are at different evolutionary stages.

Lacy et al. (2007) have imaged the W51 IRS2 region with [S IV] line at 10.5 μm and found a high-velocity ionized streamer, with a relative velocity of up to 100 km s^{-1} with respect to the systematic velocity. Such ionized streamer was detected at $\sim 2''$ to the north of the 7 mm continuum peak and extended $4''$ in the east-west direction.

Here, we report the detection of linearly polarized emission of dust continuum at an angular resolution of $0\rlap{.}''7$ toward the W51 North, which appears to be still in a collapsing phase and several O stars have been identified surrounding it.

3.2   Observation and Data Reduction

The observations were carried out on 2008 July 13 using the SMA (Ho, Moran, & Lo 2004) [1] in the extended configuration, with seven of the eight antennas available. Note that this observation was carried out along with W51 e2/e8, and these two sources shared the same calibrators and were reduced and imaged by the same way, the details of the observation and data reduction is shown in Tang et al. (2009b). In summary, the projected lengths of baselines ranged from 30 to 262 kλ. The largest size scale which could be sampled in this observation was $\sim 8''$ (0.3 pc). The local oscillator

---

[1] The Submillimeter Array is a joint project between the Smithsonian Astrophysical Observatory and the Academia Sinica Institute of Astronomy and Astrophysics and is funded by the Smithsonian Institution and the Academia Sinica.

frequency was tuned to 341.482 GHz. The primary beam (field of view) of the SMA at 345 GHz is $\sim 30''$. The presented maps were constructed with natural weighting, and the size of the synthesized beam is $0''.7 \times 0''.6$ with a P.A. of -58°. The noise levels of the Stokes I, Q, and U components are 50, 3 and 3 mJy beam^{-1}, respectively. The strength (I_{p}) and percentage ($P(\%)$) of the linearly polarized emission are calculated from: $I_{\mathrm{p}}^2 = Q^2 + U^2$ - $\sigma_{Q,U}$ and $P(\%) = I_{\mathrm{p}}/\mathrm{I}$, respectively. Here, $\sigma_{Q,U}$ is the noise level of the Stokes Q and U images, and it is the bias correction due to the positive measure of I_{rmp} (Leahy 1989; Wardle & Kronberg 1974). The resulting noise level of I_{p} ($\sigma_{I_{\mathrm{p}}}$) is therefore 3 mJy beam^{-1}. All maps shown have been corrected for the primary beam attenuation.

The presented polarization vectors were gridded every $0''.3$, $\sim$ half of the synthesized beam in order to present the variation of the P.A.s of the detected polarization across the detected regions.

3.3 Results

3.3.1 Continuum emission

We obtained the best dust continuum map of the W51 North region, with high sensitivity (50 mJy beam^{-1}) and high angular resolution ($0''.7$). The dust continuum at the wavelength of 870 μm is resolved and is elongated in the east-west direction (Figure 1), consistent with the NH$_3$ map (Zhang & Ho 1995). The main dust continuum component lies in the south of the luminous infrared source IRS2d. There is another weaker dust clump $2''$ in the north of IRS2d. Note that the elongation of the main dust ridge is at P.A. of $\sim 90°$, nearly following the maximum velocity gradient of the envelope traced with C$_2$H$_3$CN by Zapata et al. (2008). This rotating C$_2$H$_3$CN envelope is seen to be series of condensations in the east-west direction. The continuum peak is at the position of the "dominant center" and is consistent with the 7 mm continuum peak. Note that there are water maser spots near the peak position, suggesting that it is active in the star formation process. To the west of the peak, the ridge is resolved into three more clumps. The two clumps in the far west are aligned

nearly on the major axis of the dust ridge, where one of the clump is detected at $0\rlap{.}''5$ north of the radio source W51d2 and the NH_3 maser spot (Mauersberger et al. 1987; Wilson, Gaume, & Johnston 1991).

The total continuum in the main dust ridge is 16 ± 1 Jy. The clump in the north of IRS2d has flux density of 1.2 ± 0.2 Jy. Associated with W51 North:dust, the UCHII region W51d2 has the strength of 19 mJy at 1.3 cm with a projected diameter less than 300 AU (Gaume, Johnston, & Wilson 1993) and therefore, the 870 μm continuum emission is dominant by thermal dust emission. Assuming a gas temperature of 100 K, and the dust emissivity β of 1, the derived gas mass M_{gas} is 424 $M_\odot$ in the main ridge, and 32 $M_\odot$ for the clump in the north.

3.3.2   Dust Polarization and the B Field

The linear polarization is detected in most part of the dust ridge. The P(%) is in the range of <1 to 4.5%. At $1''$ and $2''$ west of the peak, there are zones of depolarization. The P.A.s in most of the detected vectors are at $\sim 120°$ (from north to east) with smooth variation within the clumps. Note that in between these depolarization zones, the P.A.s of polarization are very different from the P.A.s at the other positions. The depolarization zone is most likely due to the abrupt change in P.A. of the B field lines and simply smeared out within the synthesized beam, as seen in the W51 e2/e8 regions (Tang et al. 2009). It is also possible that due to superposition of two different polarization components, and thus the polarization cancelled out.

Assuming the dust grains are aligned with the B field, the $B_\perp$ morphology integrated along the line of sight can be derived by rotating the direction of the detected polarization by 90°. Because the polarized percentage (P(%)) does not have the information of the B field strength, we plot the derived B field vectors with identical length (Figure 2).

The B field in general is at P.A. of $\sim30°$ in the fainter clumps, i.e. the clump in the north of IRS2d, and the two clumps in the far west of continuum peak. At the brightest spot, deviations in B field lines can be hourglass-like. The clump in between

the depolarization zones, B field lines appear to be fan-like. Possible interpretation will be discussed in the next section.

3.4 Discussion

3.4.1 Dust continuum in collapsing cores

Now we compare the detected continuum emission with the collapsing core W51 e2/e8, which is also located in the same Giant Molecular Cloud of W51 North. These two sources were observed at the same time under the same array and weather conditions, and shared the same calibrators. Therefore, the possible bias and uncertainties from both the observed results can be eliminated.

Both the W51 e2/e8 and W51 North:dust are known to be in collapsing phases. The detected flux density at 870 μm in W51 e2 and e8 is 9.3 and 4.0 Jy, respectively, while it is 16 Jy for W51 North:dust. W51 North:dust is slightly stronger in continuum emission. The elongation lengths of the W51 e2 and e8 dust ridges are both $\sim 3''$. In contrast, the main dust ridge of W51 North is double the lengths of the ones in W51 e2/e8, $\sim 6''$. The peak intensity in e2, e8 and North regions are 3.8, 2.2 and 3.7 Jy beam^{-1}, respectively. These two sources have similar peak intensities. The main differences in e2/e8 and North:dust are that the free-free continuum emissions are stronger, and the hot core lines are stronger in e2/e8 regions. Besides, there are two collapsing cores detected toward e2/e8 region, with the peak intensity differs by a factor of 1.7. While in W51 North:dust, the continuum emission is concentrated in one peak. The second brightest continuum peak in W51 North:dust has intensity of 1.1 Jy beam^{-1}, almost 4 times smaller than the peak component.

In the collapsing core G31.41, the flux density is 21.2 Jy with the elongation of the dust ridge of $6''$. There is also only one dust continuum peak in this region and there no other peaks resolved within $1''$ beam. Is the W51 e2/e8 region a special case? Does the existence of two collapsing cores in one subcritical envelope due to the evolutionary effect?

3.4.2   Fragmentation?

W51 North is a massive star forming regions, and there are several star formation processes going-on at different evolutionary stages (§3.1). The polarization image is shown to be very sensitive to underlying structures. The individual clumps detected near the ring structure is from individual condensation.

In the west of the ring, there are aligned polarization vectors, where the P.A.s of the polarization is very different from the other positions'. The origin of this structure is not clear. Note that there is a high velocity streamer detected using the ionized line (see §3.1), and the strongest feature seems to link to the dust ridge. Can this fan-like B field dragged by this streamer? Can it be the remnant B field when this $5''$ dust ridge formed?

The rest of the clumps, i.e OKYM1, W51d2 and the clump north of IRS2d, have the B field direction nearly at P.A. of $30°$, $\sim30°$ east of the proposed rotating axis traced with hot core line by Zapata et al (2008). Can these sources be in earlier evolutionary stages?

Near the strong IR source IRS2d, there is no dense dust clumps detected. We note that there are three O stars identified in W51 North region. It is likely that dust grains here are evaporated by the radiation from the nearby OB stars. There are hot core lines detected centered on IRS2d (Zapata et al. 2008). It is most likely that the lines are originated from the radiation of this source. On the other hand, the temperature $4''$ in the south of IRS2d is ~80 K (Zapata et al. 2009). It seems that the dust ridge here is "young" (not affected much by the radiation yet).

3.4.3   B field dragged by the molecular ring?

Zapata et al. (2009) reported the detection of a molecular ring seen in SO_2 emission line. A molecular outflow as traced by SiO 5-4 emission is launched near the "dominant center". Proposed by the same authors, this molecular ring harbors both infall and Keplerian motions. Furthermore, the axis of the molecular outflow seems to be aligned with the line of sight as suggested by the large radial velocities of the outflow. Can the B field lines near the continuum peak be dragged by the motions of

the ring through ionized particles? To test this scenario, the kinematics derived from the ionized molecular lines such as $H^{13}CO^+$ is required.

Nevertheless, we note that the major axis of this molecular ring deviates from the major axis of the dust ridge by 18°. The ring is suggested to have small inclination angle and almost lie in the plane of sky (Zapata et al. 2009). The B field lines seem to be twisted near the "dominant center". If the field lines are anchored to the motions of the molecular ring, we would expect the B field lines to be pinched, strongly twisted, and inclined. Therefore, the morphology of the B field will be different from an hourglass. A model including all the known kinematics of the molecular ring is needed to have further interpretations.

3.4.4 Correlation of outflow axes with B field direction and dust ridge

There are two outflows detected originating from the continuum peak. Based on the SiO and H_2O masers, Eisner et al. (2002) proposed an outflow at a P.A. of 105° to 140° with an extent of 0″.6. While tracing with the SiO 5-4 molecular line, Zapata et al. (2009) propose an outflow at P.A. of 150° ± 20° with an extent of 4″. It is possible that there outflows originate from different condensations, since there are several clumps with different B field direction detected along the dust ridge. However, we note that the outflows traced by SiO and H_2O maser spots seem to originate from the "dominant center". We could not rule out the possibility that the outflow/jet system is processing.

Note that there is no clear correlation of the outflow axes and the main dust ridge. Theoretically, the outflow is launched by a disk-like structure. It seems that angular momentum of the disk has little influence from the earlier contraction phase.

3.4.5 B field in massive collapsing cores

With $\sim 1''$ angular resolution, the SMA has observed the collapsing cores G31.4, W51 e2/e8 and the presented W51 North. The B field in these regions all show

that B field is nearly perpendicular to the major axis of the dust ridge. The B field morphologies of G31.4 and near the "dominant center" in W51 North are possibly dragged by the rotation of the central flattened structures. All these results seem to support the notion that the massive stars are formed through similar processes as the low mass cases. Although the kinematics in these massive cores can be complex, in the collapse phase the role of the B field seems to be not different from the low mass cases.

3.5   Summary

We have resolved the 870 μm dust continuum and the B field morphology in W51 North region. Within the resolved clumps, the B field morphologies appear to be smooth and have variations within individual clumps. The B fields in most clumps have similar P.A.s. In the clump associated with the continuum peak, the B field lines seem to have a systematic variation, which can be explained by an inclined hourglass-like morphology with rotation near the center. A fan-like B field is detected in 2″ west of the continuum peak.

The kinematics derived from the ionized line, and a model to simulate the observed B field near the "dominant center" are required to interpret the results more quantitatively.

Table 3.1. SMA dust polarization at 870 μm in W51 North:dust

$\triangle$x	$\triangle$y	I(Jy/B)	P(%)	I_{p}(mJy/B)	$\phi(°)$
0.3	-0.3	0.50	2.4 $\pm$ 0.6	12	-60 $\pm$ 7
0	-0.3	0.64	2.2 $\pm$ 0.5	14	-59 $\pm$ 6
-0.3	-0.3	0.45	2.0 $\pm$ 0.6	9	-49 $\pm$ 9
-2.7	-0.3	0.33	4.5 $\pm$ 0.9	15	-62 $\pm$ 6
-3	-0.3	0.44	4.3 $\pm$ 0.7	19	-69 $\pm$ 4
-3.3	-0.3	0.40	3.0 $\pm$ 0.7	12	-59 $\pm$ 7
-3.6	-0.3	0.34	2.9 $\pm$ 0.8	10	-45 $\pm$ 8
0.3	0	1.11	0.9 $\pm$ 0.3	10	-74 $\pm$ 8
0	0	1.57	0.7 $\pm$ 0.2	11	-63 $\pm$ 7
-0.3	0	1.25	0.8 $\pm$ 0.2	10	-41 $\pm$ 9
-1.5	0	0.50	1.8 $\pm$ 0.6	9	-40 $\pm$ 9
-2.7	0	0.50	2.2 $\pm$ 0.6	11	-79 $\pm$ 7
-3	0	0.81	1.6 $\pm$ 0.4	13	-82 $\pm$ 6
0.3	0.3	2.40	0.5 $\pm$ 0.1	12	-82 $\pm$ 7
0	0.3	3.33	0.3 $\pm$ 0.1	10	-62 $\pm$ 8
-0.3	0.3	2.60	0.5 $\pm$ 0.1	13	-40 $\pm$ 6
-0.6	0.3	1.50	0.6 $\pm$ 0.2	9	-41 $\pm$ 9
-1.2	0.3	1.00	0.9 $\pm$ 0.3	9	-20 $\pm$ 9
-1.5	0.3	1.00	1.6 $\pm$ 0.3	16	-18 $\pm$ 5
-1.8	0.3	0.56	1.8 $\pm$ 0.5	10	-10 $\pm$ 8
-2.7	0.3	0.60	2.0 $\pm$ 0.5	12	85 $\pm$ 7
-3	0.3	0.86	1.4 $\pm$ 0.3	12	78 $\pm$ 7
0.6	0.6	1.67	0.6 $\pm$ 0.2	10	83 $\pm$ 9
0.3	0.6	2.40	0.5 $\pm$ 0.1	12	-84 $\pm$ 7

Table 3.1 (continued)

$\triangle$x	$\triangle$y	I(Jy/B)	P(%)	I_p(mJy/B)	$\phi(°)$
0	0.6	4.00	0.2 ± 0.1	8	-65 ± 10
-0.3	0.6	3.67	0.3 ± 0.1	11	-43 ± 8
-1.2	0.6	1.29	0.7 ± 0.2	9	13 ± 9
-1.5	0.6	1.13	1.5 ± 0.3	17	11 ± 5
-1.8	0.6	0.52	2.9 ± 0.6	15	19 ± 6
-2.7	0.6	0.32	3.1 ± 0.9	10	80 ± 8
-3	0.6	0.54	2.8 ± 0.5	15	74 ± 6
-3.6	0.6	0.42	2.4 ± 0.7	10	-62 ± 8
-3.9	0.6	0.34	3.8 ± 0.8	13	-66 ± 6
0.6	0.9	1.13	0.8 ± 0.3	9	-79 ± 10
0.3	0.9	1.63	0.8 ± 0.2	13	-76 ± 6
0	0.9	2.25	0.4 ± 0.1	9	-70 ± 9
-1.2	0.9	1.20	1.0 ± 0.3	12	25 ± 7
-1.5	0.9	0.63	3.0 ± 0.5	19	29 ± 4
0.6	1.2	0.46	2.4 ± 0.6	11	-56 ± 7
0.3	1.2	0.58	2.4 ± 0.5	14	-69 ± 6
0	1.2	0.77	1.3 ± 0.4	10	-80 ± 8
-1.2	1.2	0.75	1.2 ± 0.4	9	34 ± 10
-0.9	1.5	0.39	3.1 ± 0.7	12	67 ± 7
-1.5	4.8	0.31	2.9 ± 0.9	9	-71 ± 9
-1.8	4.8	0.40	2.5 ± 0.7	10	-62 ± 8
-2.1	4.8	0.42	2.4 ± 0.7	10	-38 ± 8
-1.8	5.1	0.34	2.9 ± 0.8	10	-49 ± 8
-2.1	5.1	0.40	3.0 ± 0.7	12	-36 ± 7

Table 3.1 (continued)

$\triangle$x	$\triangle$y	I(Jy/B)	P(%)	I_{p}(mJy/B)	$\phi(°)$
-2.4	5.1	0.29	3.4 ± 0.9	10	-27 ± 8

Note. — $\triangle$x & $\triangle$y: offsets in arcsecond from the coordinate (J2000): $\alpha = 19^{\mathrm{h}}23^{\mathrm{m}}40.05^{\mathrm{s}}$, $\delta = 14°31^{'}5{.}^{''}0$. I_p: the polarized intensity in mJy beam^{-1}. P(%): polarization percentage, defined as the ratio of I$_p$/I. ϕ: position angle from the north to the east in degree. All data listed are above $3\sigma_{I_{\mathrm{p}}}$.

Figure 3.1 Polarization map in W51 North:dust with natural weighting. The plotted red and black vectors are above 3 and between 2 to 3 σ_{I_p}, respectively. Contours represent the 870 μm continuum strength at 3, 6, 9, ..., 24, 27, 30, 35, 40, ..., 60, 65, 70 $\times$ 50 mJy beam^{-1}. Polarized intensity map is shown in color scale with strength shown in wedge in units of mJy beam^{-1}. The black triangle marks the position of the SiO masers (Eisner et al. 2002), which is also the 7 mm continuum peak (Zapata et al. 2009). The cyan square marks the position of the edge-brightened cometary/shell-like HII region W51d (Gaume, Johnston, & Wilson 1993), which is labelled as IRS2d in this paper. W51d2 is a radio source (UCHII region) and associated with NH$_3$ masers (Gaume et al. 1993; Mauersberger et al. 1987; Wilson, Gaume, & Johnston 1991). KJD3, also called OKMY 1, are the infrared sources with silicate absorption features and is proposed to be a protostar candidate (Okamoto et al. 2001; Kraemer et al. 2001). The blue stars mark the identified O stars by Okamoto et al. (2001). The synthesized beam is 0$\farcs$7$\times$0$\farcs$6 with a P.A. of $-57°$, shown as black ellipse in the lower-left corner.
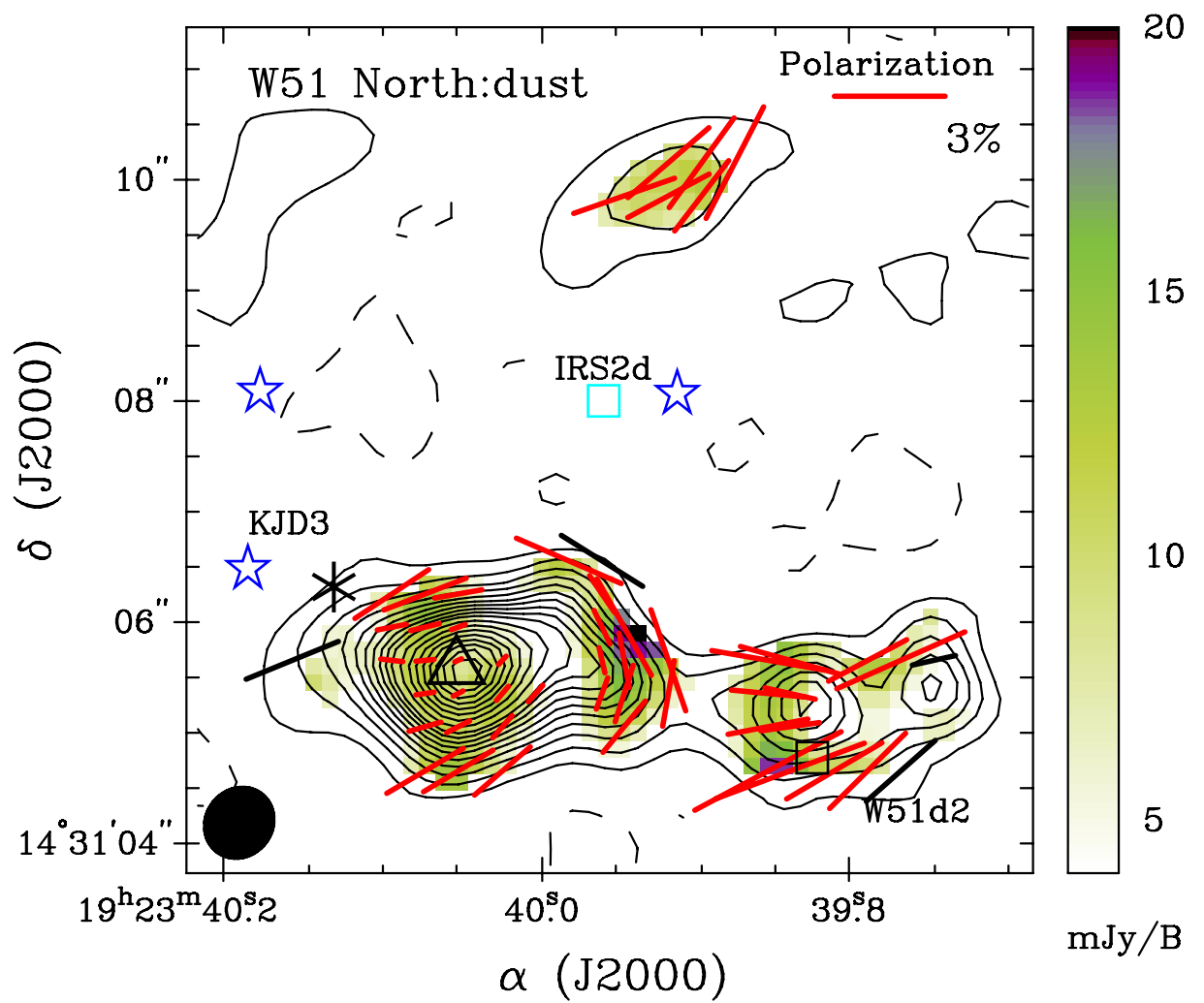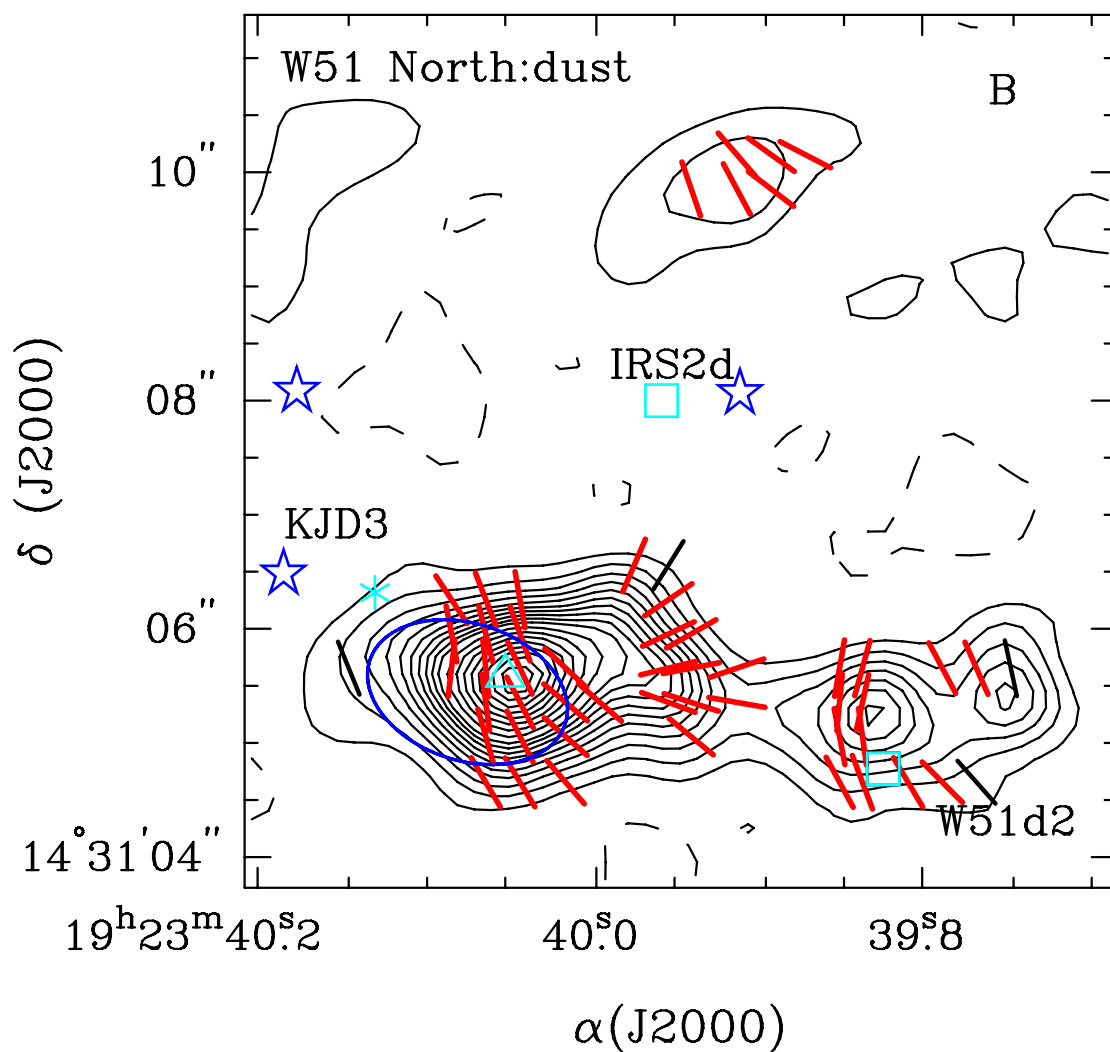
Figure 3.1 –continue..

Figure 3.2 B field map in W51 North:dust. The B field segments are derived by rotating the polarization by 90° with the equal length. The blue ellipse marks the ring-structure seen in SO$_2$ by Zapata et al. (2009). The deconvolved size of the ring is 1″8×1″2. All the other symbols are the same as in Figure 1.

Chapter 4

Remnant Disk in Massive Star Forming Region Orion BN/KL?

Tang, Ya-Wen, Ho, Paul T. P. et al.

ApJ, in prep.

ABSTRACT

We made a full synthesis of the dust continuum emission and its linear polarization at 870 μm wavelength for the massive star forming region Orion BN/KL. The estimated total gas mass from the dust continuum is only 3 - 20 $M_\odot$, which is much smaller than the total binding mass estimated from the virial theorem. This suggests that the majority of the molecular material has already been dispersed. Based on the morphology of the dust continuum, we interpret the emission as the remnant of an inclined-disk, with source I and SMA 1 near the inner edge of the disk. The morphology and polarization seem to support the scenario of an explosion 500 year ago when the source BN and I were ejected. With an angular resolution of $1''$ (2 milli-pc), the inferred B field directions in the plane of the sky vary significantly and smoothly around the central stars. In this scenario, the B field seen in the south of IRc2 is toroidal, being anchored to the rotating remnant disk. In the mean time, the poloidal B field associated with the 0.5 pc B field is kept in the rest of the remnant

disk. However, the possibility of mechanical alignment can not be ruled out.

4.1   Introduction

Massive star forming site is typically further away than the low mass cases. More-over, massive stars are forming in groups and are almost always in a more complex environment. To understand the massive star formation process, higher spatial reso-lution is necessary. The Kleinmann-Low (KL) (Kleinmann & Low 1967) nebula in the Orion molecular cloud, as the closest massive star forming site, is the best candidate for study. In this paper, we adopted a distance of 480 pc to the KL nebula (Genzel et al. 1981).

Inside the KL nebula, the Becklin-Neugebauer (BN) object is the brightest near-infrared source (Scoville et al. 1983). The source IRc2 is strong in mid-IR emission, and it is resolved into several isolated peaks in mid-IR (Shuping, Morris & Bally 2004), suggesting that it is a cluster forming region. With high angular resolution (up to $0\rlap{.}''7$) sub-millimeter (sub-mm) observations, Beuther et al. (2004; 2006) further identified the sub-mm counter part of the radio source I and a new sub-mm source SMA 1, and reported the mass of source I estimated from the sub-mm continuum of 0.2 $M_\odot$, and unknown for SMA1. Based on the proper motions of BN, source I and source n on the order of 10 mas yr^{-1}, Gomez et al. (2005) have proposed that they are run-away stars from a common center, some where between BN and source I about 500 yrs ago, hereafter we name it as BN-I center. Alternatively, Tan (2005) suggested that BN is a run-away star from the $\theta^1 C$ system.

Reid et al. (2007) reported the existence of an ionized accretion disk surrounding source I with a radius of 35 AU at a position angle (P.A., from the north to the east) of $\sim -40°$. An outflow on the scale of 4 milli-pc ($1\rlap{.}''7$), as traced by H_2O masers, (Greenhill et al. 1998) is suggested at P.A. of $\sim 45°$ centered on source I, nearly perpendicular to the plane of the ionized accretion disk. The orientations of this accretion disk and the outflow are consistent with the observations of the proper motion of SiO masers (Chandler 2005; Doddi et al. 2009). In contrast, the high velocity outflow detected in CO (Zapata et al. 2009; Chernin & Wright 1996) and in

H_2 (Kaifu et al. 2000) are in the NW-SE direction and are extended much over larger scales of 0.1 to 0.2 pc. These outflows at different size scales are most likely driven by different sources and ejected at different times.

Associated with BN/KL, there is a hot molecular core. Observed with NH_3 lines with $1''$ resolution, the linewidths of individual clumps in the Orion BN/KL core are narrow, smaller than the velocity resolution of 1.3 km s^{-1} in most clumps (Migenes & Wilson 1989). However, the relative peak velocities of the clumps are larger than the thermal motions. This superthermal motion between clumps could be due to the HII expansion, the outflow motions, the Alfvenic motions driven by the B field, or some other systematic motions.

The polarization of the Orion Nebula has been observed at various wavelengths and on various size scales. At 0.5 pc ($3.5'$) scale, the polarization at 350 and 450 μm seems to be uniform, and the B field directions are perpendicular to the dust ridge at that scale (Vaillancourt et al. 2008). Schleuning (1998) proposed that the B field starts to exhibit hourglass-like morphology at 0.5 scale based on the 100 μm polarization results. At 0.01 pc ($4''$) resolution, the position angles (P.A.s) of the polarization vary significantly on 0.02 pc ($10''$) scale at 1.3 mm and 3 mm (Rao et al. 1998). Observations with $1''$ resolution at various wavelengths all indicated that the P.A.s vary significantly near IRc2, such as at mid-IR by Aitken et al. (1997), or in the shocked region traced by H_2 ν = 1-0 S(1) by Chrysostomou et al. (1994). Compared with the mid-IR work, the polarized emission observed at sub-mm wavelengths is optically thin, and traces directly the dense regions, where the stars are forming. High angular resolution observations of the polarization at sub-mm are therefore crucial to understand the B field structure near IRc2.

In this paper, we present 870 μm observations of the Orion BN/KL region. With the combined three different configurations, we are able to achieve a much better uv coverage than the observations by Beuther et al. (2004), with comparable angular resolution of up to $0''.6$. We detected dust structures > 0.04 M$_\odot$ (see the assumptions in section 4.3.1), with size scales ranging from 0.2 milli-pc to 0.19 pc.

4.2   Observation

The observations were carried out on Jan 6 2008, Jan 25 and Feb 15 2009 using the Submillimeter Array (Ho, Moran & Lo (2004)) [1] in the compact, subcompact and extended configuration, respectively. The observational parameters are listed in Table 1. The projected baseline lengths ranged from 7 to 253 kλ ($\lambda = 870\ \mu$m). The sampled structures range from $0\rlap{.}''8$ to $80''$. The achieved angular resolution is $1\rlap{.}''2 \times 1\rlap{.}''1$, and the rms sensitivity is 70 mJy beam^{-1}. This is 54 times the theoretical expectations. The reason of the high actual measured rms is due to the existence of much larger scale structure, which is not recovered in our synthesized measurements. The presented maps are made by combining three tracks unless described separately. These are the best and most sensitive synthesis maps of the dust emission that we can make for this region at the moment. The absolute pointing accuracy of our maps is estimated to be $0\rlap{.}''4$ from the phase noise of $10°$.

4.3   Results

4.3.1   Continuum Emission

The 870 μm continuum emission in Orion KL is resolved into three clumps (Figure 1(left-panel)). We reckon that nearly all of the 870 μm emission is due to dust. The free-free emission in the region is very faint, at the 1.1 mJy level at 3.6 cm (Menten & Reid 1995), which can be negligible when extrapolated to 870 μm. The brightest dust continuum clump is associated with source I and SMA 1, hereafter we name it as *main dust ridge*. The continuum peak is $1''$ south-east of source I and $2''$ north-east of SMA 1. The relative shift in position of the main dust ridge with respect to these sources is real and significant. The Infrared sources IRc2 are to the north-west of source I, again offset from the main dust ridge. In the west, two fainter dust clumps are detected to the south of BN. The south-west clump is situated at the

---

[1]The Submillimeter Array is a joint project between the Smithsonian Astrophysical Observatory and the Academia Sinica Institute of Astronomy and Astrophysics and is funded by the Smithsonian Institution and the Academia Sinica.

so called "compact ridge", where strong line emission of oxygen-bearing molecules were detected (Beuther et al. 2005). The infrared sources IRc4 and IRc5 are in the periphery of the compact ridge. The north-west clump is near the infrared source IRc3, IRc6 and IRc20. Note that all the infrared sources are offset from the dust continuum peaks. Such offsets suggest that these sources are most likely physically located outside of the dense dust continuum clumps. Measurements of the extinctions toward these sources are required to estimate their relative positions along the line of sight, with respect to the dust emission peaks.

There is no 870 μm continuum peak detected at BN, source n, and the BN-I center. Furthermore, the morphology of the 870 μm dust continuum emission is similar to the NH_3 line emission structure as seen by Migenes et al. (1989) and Wilson et al. (2000), i.e. being bright to the east of source I, source n and IRc2, and with a cavity to the west of these sources. The coincidence with NH_3 line emission suggests that the revealed 870 μm continuum is mostly tracing the dense gas. Due to the significant differences in the spatial distributions of the molecules detected in these regions, Blake et al. (1987) and Beuther et al. (2005) suggest that these molecular line maps may help to differentiate evolutionary stages. The importance of the 870 μm dust emission is that it is optically thin, impervious to chemistry, and reliably tracks the total mass distribution.

The detected flux density in the *main dust ridge*, compact ridge and the north-west clump is 23±2 Jy, 8±1 Jy, and 7±1 Jy, respectively. When measured with the JCMT, the brightest point with 14″ angular resolution is 132 Jy beam^{-1} (Vallee & Fiege 2007). The reported SMA measurement therefore recovers 38% of the total flux density. When fitted with Gaussians toward the emission peaks in the map constructed with only the extended array data, the detected flux density in Source I and SMA 1 is 1.1±0.1 Jy and 2.3±0.1 Jy. Therefore, $\sim 9\%$ of our recovered continuum flux density is associated with source I and SMA 1.

Associated with the *main dust ridge* there is a "hot core", where a lot of hot core lines were detected (Beuther et al. 2005). The gas temperature is $\sim$ 165 to 400 K (Wilson et al. 2000). In the condition of LTE, the dust emission traced here is most likely tracing dense and hot gas. Assuming under LTE, the dust grains are at the

temperature of 160 K as traced with NH_3. The gas mass (M_{gas}) in the *main dust ridge* estimated from the dust continuum is 2 to 12 $M_\odot$, where the limits for M_{gas} are from the dust emissivity β of 1 or 2. The stellar mass of source I derived based on the kinematics of the maser spots is 6 to 10 $M_\odot$ (Greenhill et al. 2004). Based on the line-widths of ten NH_3 clumps, Migenes& Wilson (1989) reported the binding mass estimated from virial theorem within these clumps range from $<0''\!\!.7$ $M_\odot$ to $17''\!\!.3$ $M_\odot$. It is likely that the majority of the dust grains we traced has been dispersed by the stellar feedback. Note that the elongation of the *main dust ridge* is perpendicular to the 0.5 pc B field direction in OMC-1 dust ridge traced by Schleuning (1998) at wavelengths of 850 μm.

Based on the same assumptions, M_{gas} in the compact dust ridge and the clump in the south of BN are both in the range of 0.7 to 4 $M_\odot$.

4.3.2   Polarization

The linearly polarized emission ($I_{\rm p}$) is detected and resolved in the *main dust ridge* and in the south-west clumps (Figure 1(right-panel)), and is barely detected in the north-west clump. Near IRc2 in the west of the *main dust ridge*, there is weak or no $I_{\rm p}$ detected. I_p is strongest in the south of source I.

The detected polarization vectors exhibit significant deviation of P.A.s between clumps. Among these, the polarization vectors extending from source I toward the south have very different P.A. from the larger scale north-south polarization direction detected at 0.5 pc by Schleuning (1998). The rest of the vectors in the *main dust ridge* are consistent with the larger scale polarization direction, indicating that the larger scale B field is still retained in most parts of the dust ridge. The most striking feature revealed with the 870 μm polarization data is that the P.A.s vary smoothly and substantially across the *main dust ridge*, from P.A. of 10° in the north-east to P.A. of 100° in the south.

4.3.3 Comparison of polarization at 3 mm, 1 mm and 0.87 mm

When comparing to the previous polarization measurements at 3 mm and 1 mm using BIMA by Rao et al. (1998), the positions where I_{p} are detected are somehow different (Figure 2) within the SMA field of view. At 870 μm, the detected polarization is centered on a 14″ region near SMA 1. While at 3 mm and 1 mm, polarized emission appears further away from SMA 1 toward the north-east and south-west following the major axis of the OMC-1 dust ridge. The P.A. of polarization at these two extensions are consistent with the detected polarization at 870 μm in the north-east of source I and the western compact ridge.

Apart from the extensions following the OMC-1 dust ridge, the polarization extending toward the south-east from source I is only detected at 3 mm. The P.A.s here seem to be consistent with the polarization detected at 870 μm in 4″ south-east of source I. Similarly, the polarization 5″ south of BN is detected at 3 mm and 1.3 mm, the P.A.s here is consistent with the ones in the north of source I and in the western compact ridge.

The main improvement of our 0.87 mm results are: 1. polarization in the clumps are resolved with tighter sampling. 2. polarization percentage decreases to emission peak. 3. polarization decreases on the side towards the central sources.

4.4 Discussion

What's new and important in this experiment?

1. The dust continuum emission and its polarized components in a massive star forming region are resolved at 2 mpc (480 AU) scale for the first time.

2. The polarization is consistent with the 3 mm and 1 mm measurements by BIMA at ∼4 arcsecond resolution. The polarization in the north of IRc2 has been resolved in our 870 μm map. The direction is consistent with the 0.5 pc scale polarization direction.

3. Note that polarization is much lower or absent on the eastern side of the main dust ridge , immediately to the west of source I.

4.4.1   Dust grains being mechanically aligned?

There are several molecular outflows detected in the Orion BN/KL region. The large scale CO outflows are in the NW-SE direction and centered on near BN-I center. The low velocity outflow centered on source I is in the NE-SW direction. If the dust grains are aligned with these outflows, the detected polarization will be nearly parallel to the direction of these outflow due to the Gold alignment (Gold 1952).

However, the detected position angle of the polarization varies smoothly across the hot core ridge. These angles do not seem to align with the outflows. Furthermore, the fact that the smooth variation of position angle across the dust ridge seems to be difficult to be explained by the alignment of outflows.

4.4.2   Remnant dusty disk?

With an angular resolution of $\sim 3''$, Zapata et al. (2009) found a 0.14 pc scale CO outflow (shown in Figure 6) with velocities of ± 100 km s^{-1} originating from the BN-I center, where BN, source I and source n were proposed to have been dynamically dispersed ~ 500 yrs ago (Gomez et al. 2005). These authors noted the comparable energies released in the CO outflows and the ejection of the three sources, the comparable ages of the outflow ages and the ejection phenomenon, and the very special morphologies of the highly impulsive and poorly collimated molecular outflows. They propose that the 0.14 pc CO outflows may be the result of the disintegration of a central cloud core or circumstellar disks, when these three sources underwent a close dynamical encounter. Our results seem to support such a scenario based on the fact that there is no dust continuum emission detected at the BN-I center. As discussed in in §4.3.1, the similarity of the dust continuum emission and the integrated NH$_3$ line emission suggests that the central cavity is real.

Note that the NH$_3$ clumps are narrow in line-widths, but have large velocity dispersions between clumps on the order of ~ 15 km s^{-1} (Migenes et al. 1989). We

therefore suggest that the detected dust continuum emission is tracing a remnant disk (or flattened structure), where most of the disk has already been dispersed due to the close encounter of BN, source I, and source n, and the subsequent outflows. The fact that the 0.14 pc CO outflow filaments are numerous and bright preferentially in the northern part of the BN-I center further supports the proposed remnant disk. The detected remnant structure may have been the densest structures which were able to withstand the ionization of radiation and the shock fronts released in the event of the close encounter. As shown in Figure 3, the BN-I center is proposed to be at the center of the proposed remnant disk, which is inclined with a minor axis parallel to the larger scale B field.

Kinematics inferred from OH masers

Based on the detected positions and kinematics of OH masers, Cohen et al. (2006) suggested the presence of a expanding and rotating disk or torus with inner cavity of radius 1300 AU (3.5 milli-pc), which is elongated in the NE-SW direction and centered near source I. Our proposed scenario of remnant disk seems to agree with their interpretation.

B field in the remnant disk?

The interpretation of the remnant-disk B-field scenario would imply a toroidal B field, where the B field lines are anchored to the rotating disk such that the B field direction is perpendicular to the rotating axis of the disk. The center of the disk would be close to IRc2, as proposed by Aitken et al. (1997) or close to the the BN-I center as suggested in this paper. The polarization detected via absorption at the infrared with arcsecond resolution shows abrupt changes of the polarization angle near IRc2, IRc7 and IRc4, which are offset in position from the sub-mm dust emission peaks and therefore, can provide the B field geometry in regions where the dust continuum is absent or weak. The comparison of the infrared and the sub-mm polarization shows consistency, suggesting that the B field near IRc2 varies smoothly. In this scenario, the B fields in the extension following the OMC-1 dust ridge are tracing the poloidal

B field.

However, this retained/anchored B-field interpretation is not unique. Orion BN/KL region is very energetic with total luminosity of $\sim 10^5$ L$_\odot$. The grain alignment properties can be significantly different from the other more quiescent regions. We discuss the other possible interpretations in the next section.

Hierarchical Gravitational Fragmentation?

The proposed disk was formed before the event of the close encounter, and most part of the disk may have been dispersed later. The high velocity and large scale outflows in the NW-SE direction may have played the key role in this dispersal of the cloud core/disk. Later, there are some more smaller scale outflows formed, such as the one seen toward source I. Beuther et al. (2005) propose that SMA 1 is a protostar based on the detection of strong CH_3OH emission line, indicating that it is probably the youngest YSO in this field. In this scenario, the star formation process takes place on several size scale and via different episodes.

4.4.3   Polarization from entrained flows?

We are not able to rule out the possibilities that the dust grains are mechanically aligned as proposed by Rao et al. (1998). In this scenario, the grains are aligned with the molecular outflows through the Gold (1952) mechanism. However, we do emphasize that the revealed polarization in the south of IRc2 varies smoothly from a P.A. of 10° in the northern part of the *main dust ridge* to a P.A. of 100° in the south of IRc2. The proposed disk is centered on the BN-I center instead of the previously proposed IRc2.

4.5   Conclusion

The 870 μm dust continuum and its linearly polarized emission is detected and resolved in the Orion BN/KL region. With an angular resolution of 1″, the polarized emission from the dust continuum at submillimeter is resolved at 2 milli-pc (480 AU)

for the first time. As compared to dust polarization previously detected, the revealed polarization in the south of IRc2 changes smoothly by 90° instead of abrupt change previously observed at poorer resolution. The continuum emission is resolved into three clumps, and the strongest clump is associated with source I and SMA 1. The associated masses are 2 to 12 $M_\odot$. There is no continuum peak detected at source BN, n and the BN-I center. The upper limit of the associated mass is 0.01 $M_\odot$. We interpret the detected dust continuum as part of a remnant disk. The center of the proposed remnant disk is suggested to be at the common center of source BN and I about 500 years ago, as proposed by Gomez et al. (2005). Our proposed scenario of remnant disk is supported by the kinematics inferred from the OH masers by Cohen et al. (2006), where a clear signature of rotation is seen the positional-velocity plot. Furthermore, our proposed orientation and the center of the disk is consistent with the disk proposed by the same authors. In this scenario, the detected B field inferred from the dust continuum is toroidal in the south of source I, and is poloidal in the east of the *main dust ridge* and in the compact ridge. The poloidal B field is consistent with the field direction in the OMC-1 dust ridge. In the *main dust ridge*, source I and SMA 1 have been suggested to be active in star formation, indicating that further fragmentation is ongoing within the remnant disk. We note that the possibility of mechanical alignment can not be ruled out.

Table 4.1.   Observational parameters

Date	Configuration	gain calib.	flux calib.	BP/Pol. calib.
'08.Jan.6	Compact	0528+134	Uranus	3c273
'09.Jan.25	Subcompact	0423-013/0510+180	Titan	3c273
'09.Feb.15	Extended	0423-013	Titan	3c273

Note. — BP/Pol. refers to bandpass/polarization. Calib. refers to the calibrator. In all of the observations, the local oscillator frequencies are tuned at 341.482 GHz. With a bandwidth of 2 GHz, the frequency covered is from 345.5 to 347.5 GHz and from 335.5 to 337.5 GHz in the upper and lower sidebands, respectively. Maps of continuum emission at wavelengths of 870 μm is generated by averaging over the line-free channels.

Figure 4.1 Left-panel: SMA 870 μm continuum map in Orion BN/KL with natural weighting. Solid contours are the 870 μm continuum strength at 3, 6, 9, ..., 33, 36, 39 $\times$ 70 mJy beam^{-1}. The dashed contours are -3 and -6 $\times$ 70 mJy beam^{-1}, which are due to the missing of short spacing visibilities. The three resolved dust clumps are called *main dust ridge*, compact ridge and north-west clump anti-clockwise from the strongest clump. Asterisk marks the position of BN. Stars mark the radio sources identified by Menten & Reid (1995). Cross marks the submillimeter continuum source SMA1 identified by Beuther et al. (2004). Red pluses are the mid-infrared sources, where the adjacent numbers refer to the IRc source names in Shuping, Morris & Bally (2004), where the position uncertainties of these sources are typically $0''.1$ to $0''.3$. The cyan square marks the common center proposed by Gomez et al. (2005). The synthesized beam is $1''.2 \times 1''.1$ with a P.A. of $-16°$, shown as solid black ellipse at lower-left corner. Right Panel: Polarization map in Orion BN/KL with natural weighting. The plotted red vectors are above 3 σ_{I_P}, and black vectors are between 2 to 3 σ_{I_P}. Polarized intensity map is shown in color scale with strength in wedge in units of mJy beam^{-1}.
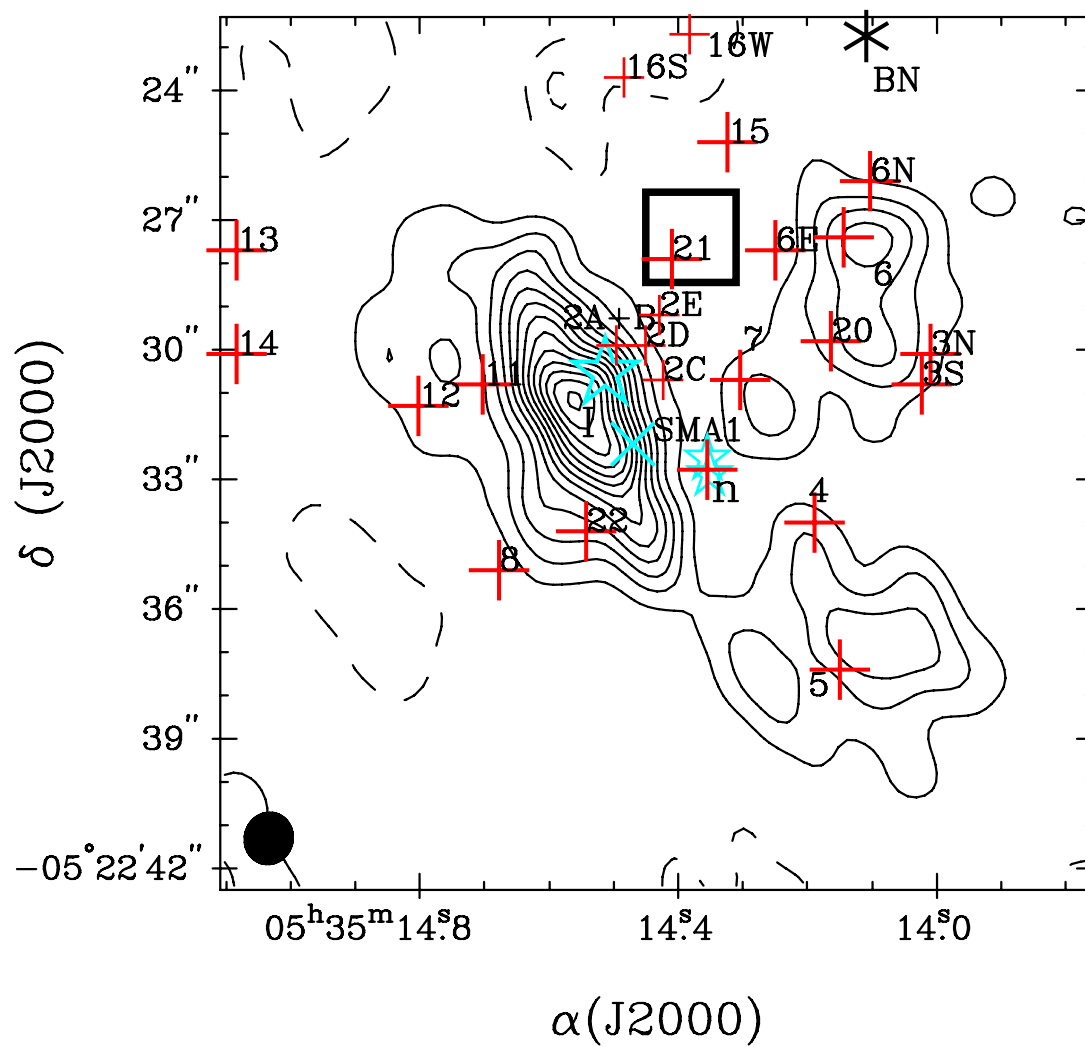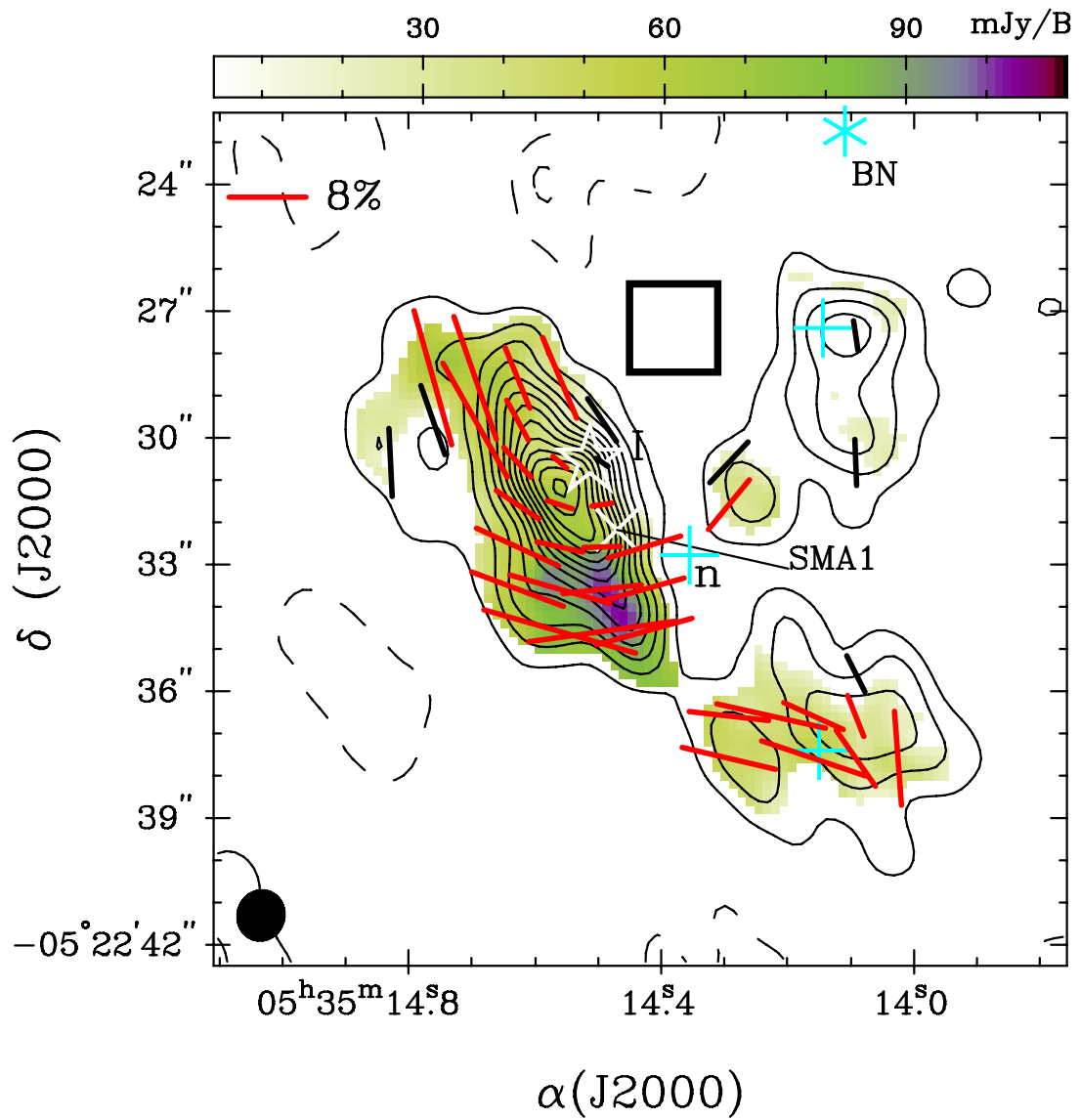
Figure 4.1 –continue

Figure 4.1 –continue
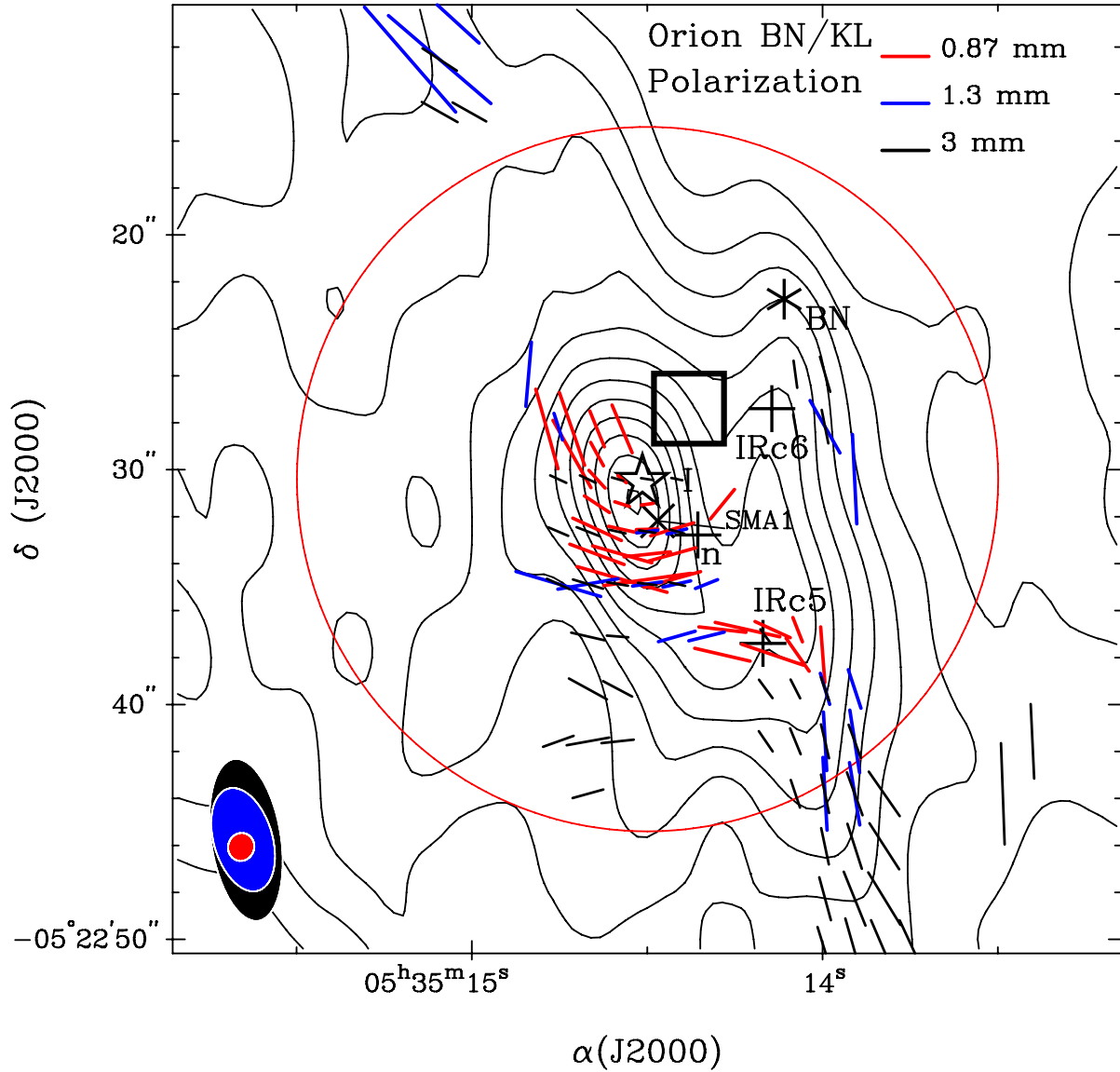
Figure 4.2 Polarization maps at 3 mm and 1 mm obtained with BIMA and at 870 μm obtained with the SMA. The sizes of the synthesized bemas are plotted in the lower-left corner in the corresponding color as indicated in the upper-right corner. The length of the indicated segments in these three wavelengths represents the polarization percentage of 8%. The black contours are the 3 mm continuum emission strength at 3, 6, 9, ..., 33, 36, 39 × 0.01 Jy beam^{-1}. The large red circle marks the field of view of 30″ of the SMA at wavelength of 0.87 mm. All the other symbols are the same as in Figure 1.

Figure 4.2 Polarization map in Orion BN/KL inferred from 0.87 mm with compact and subcompact array data. With robust weighting of 0.5, the synthesized beam is $2''\!.8 \times 1''\!.8$. All the symbols are the same as in Figure 1. The continuum emission at 0.87 mm is shown in contours plotted at 3, 6, 9, 12, 15, 20, 25, 30, 35, 40 × 0.16 Jy beam^{-1}. The polarized emission is shown in color scale. The cyan ellipse marks the proposed inclined disk, where the BN-I center is at the center of the ellipse with size equivalent to the positional uncertainty given in Zapata et al. (2009). The black circle marks the primary beam of the SMA at this wavelength. The red and black segments mark the inferred B field direction with S/N ratio above 3 and in between 2 to 3 $\sigma_{I_{\mathrm{P}}}$, respectively.
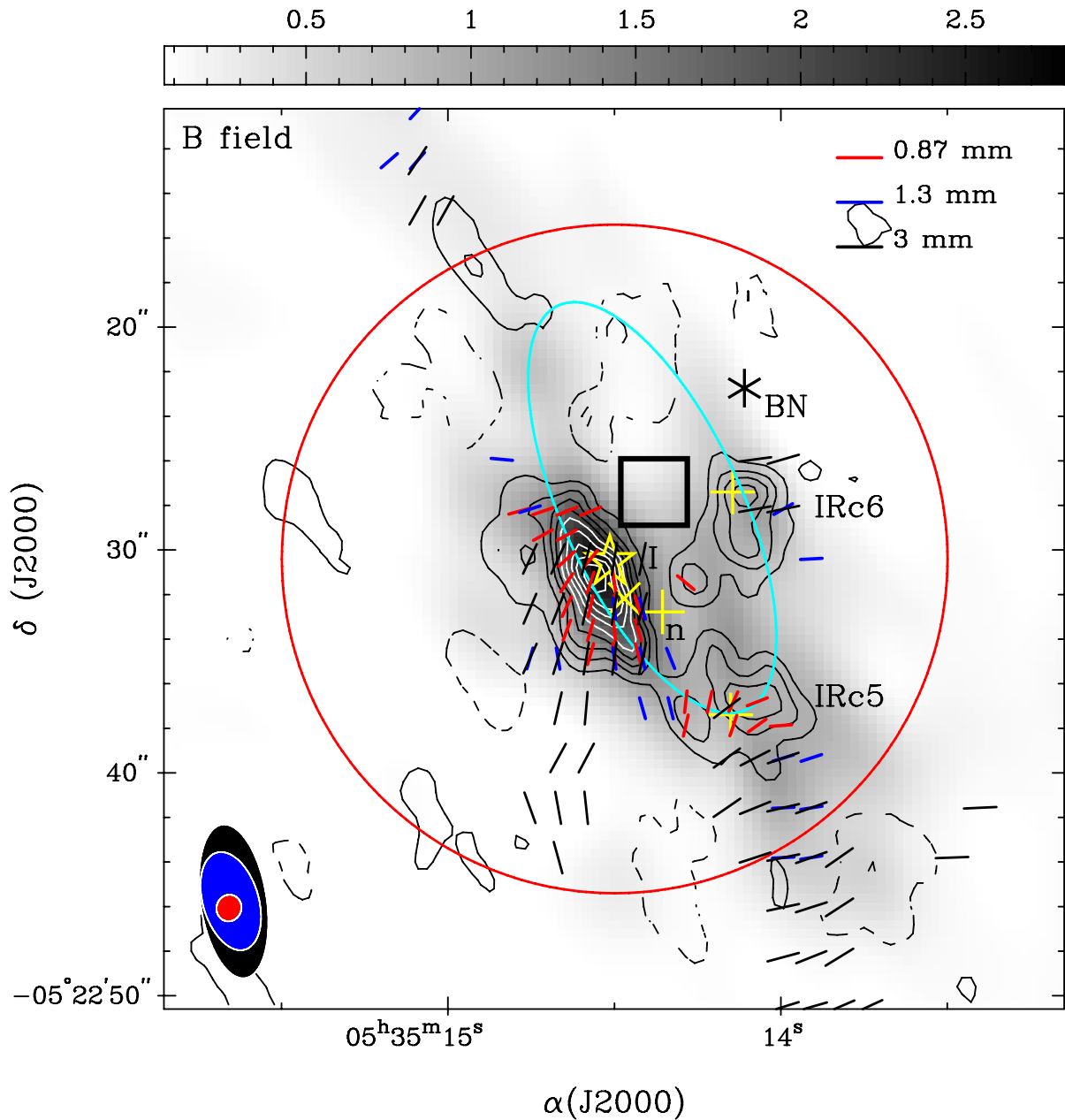
Figure 4.3 B field map in Orion BN/KL inferred from 3 mm, 1 mm, and 0.87 mm. All the symbols are the same as in Figure 1. The continuum emission at 0.87 mm is shown in contours plotted at 3, 6, 9, 12, 15, 20, 25, 30, 35, 40 × 0.07 Jy beam^{-1}, and at 1 mm in grey scale with strength indicated in the wedge in units of Jy beam^{-1}. The cyan ellipse marks the proposed inclined disk, where the BN-I center is at the center of the ellipse with size equivalent to the positional uncertainty given in Zapata et al. (2009).
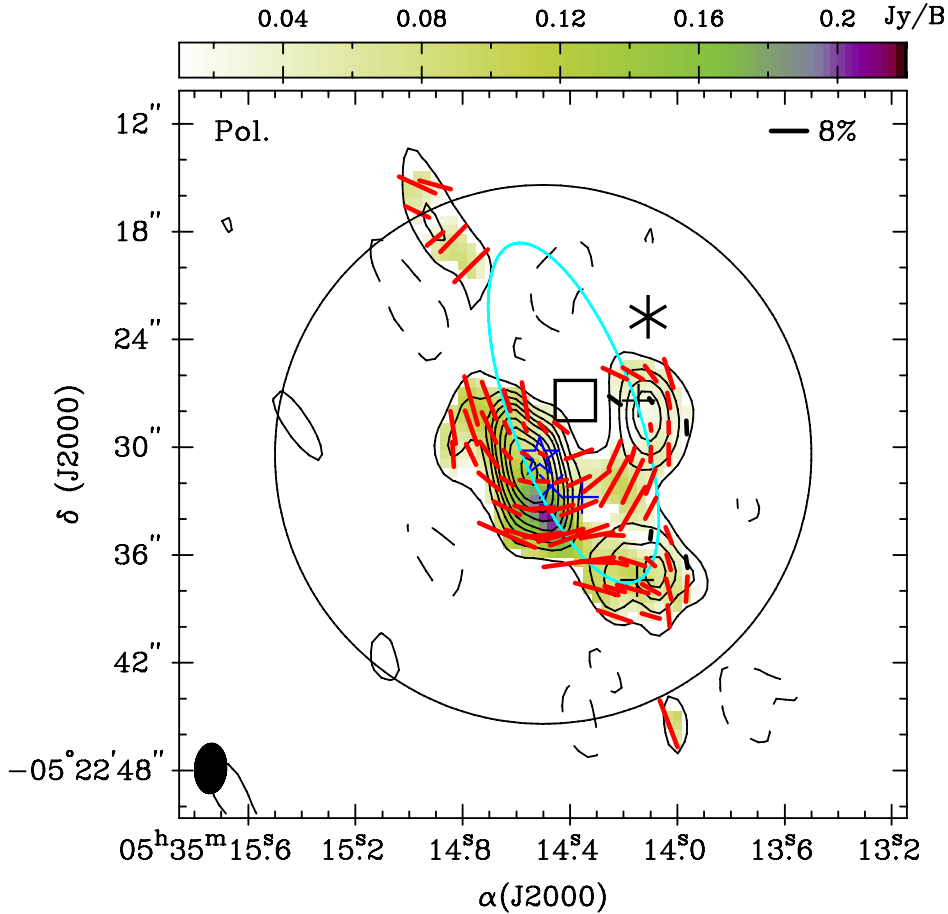
Figure 4.3 B field map in Orion BN/KL inferred from 0.87 mm with compact and sub-compact array data. With robust weighting of 0.5, the synthesized beam is $2\rlap.{''}8 \times 1\rlap.{''}8$. All the symbols are the same as in Figure 1. The continuum emission at 0.87 mm is shown in contours plotted at 3, 6, 9, 12, 15, 20, 25, 30, 35, 40 $\times$ 0.16 Jy beam^{-1}. The cyan ellipse marks the proposed inclined disk, where the BN-I center is at the center of the ellipse with size equivalent to the positional uncertainty given in Zapata et al. (2009). The black circle marks the primary beam of the SMA at this wavelength. The red and black segments mark the inferred B field direction with S/N ratio above 3 and in between 2 to 3 σ_{I_P}, respectively.
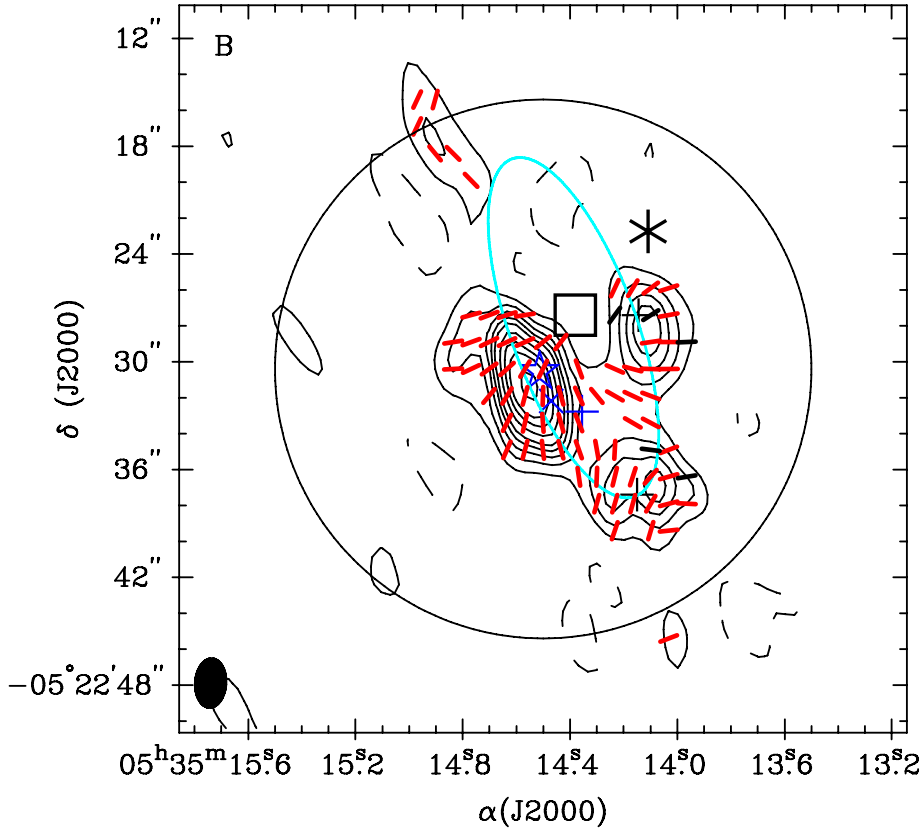
Figure 4.4 Left-panel: Map of 870 μm dust continuum emission with highest angular resolution. This map is constructed with extended array data only with uniform weighting. The size of the synthesized beam is $0\overset{''}{.}8 \times 0\overset{''}{.}6$ with a P.A. of $-74°$. The triangles mark the positions of clumps identified in NH_3 by Migenes et al. (1989) with V_{LSR} labelled in units of km s^{-1}. Note that near SMA 1, the V_{LSR}s of these clumps vary significantly, ranging from 1.6 to 9.3 km s^{-1}.
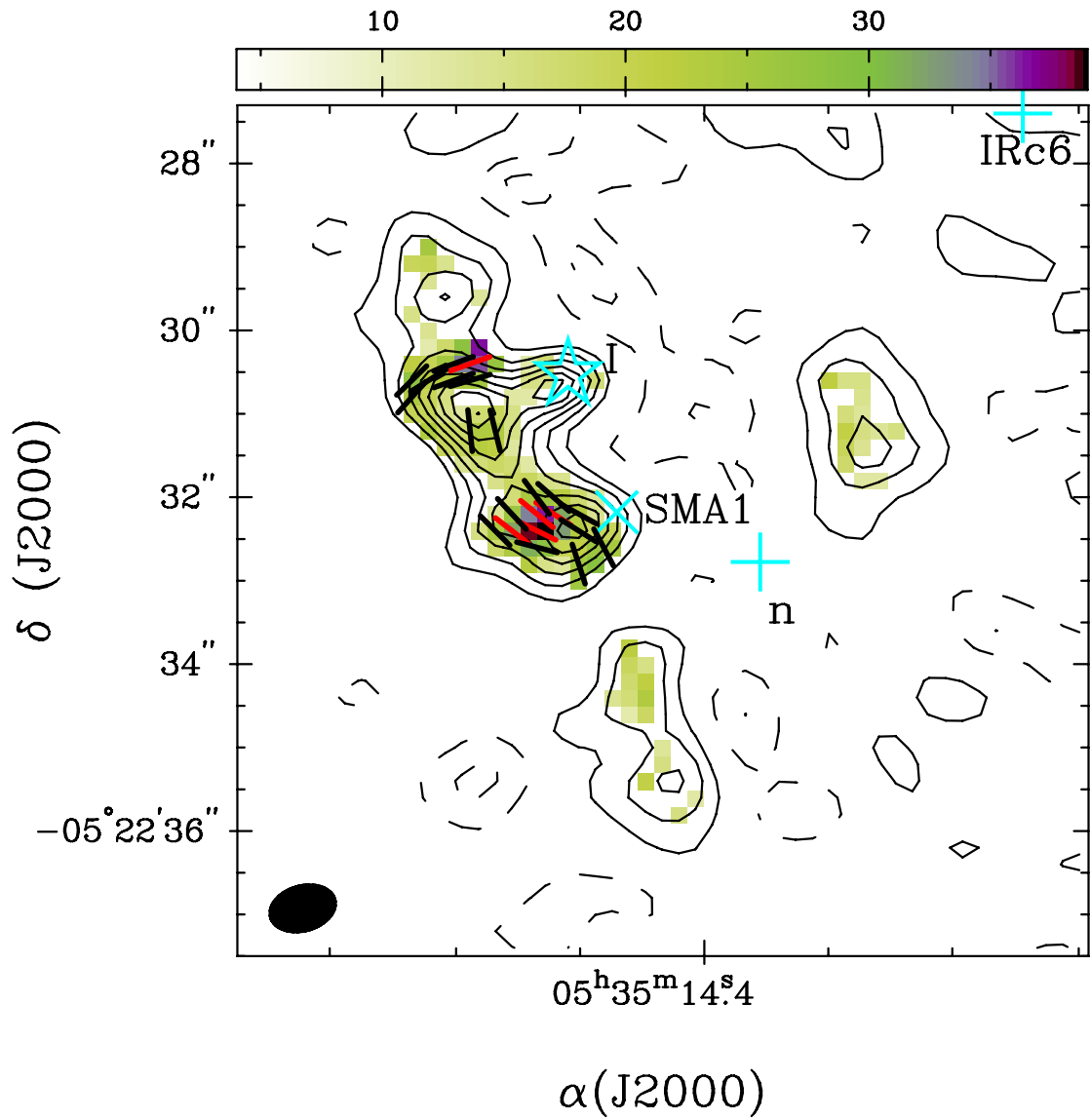
Figure 4.4 Middle-panel: B field map of the extended array track with uniform weighting overlayed on the maps shown in the left panel. The polarized intensity is presented in color scale in units of mJy beam^{-1}. The presented vectors are B field direction above $3\sigma_{I_{\mathrm{p}}}$ and between 2 to 3 $\sigma_{I_{\mathrm{p}}}$ in red and black segments, respectively.
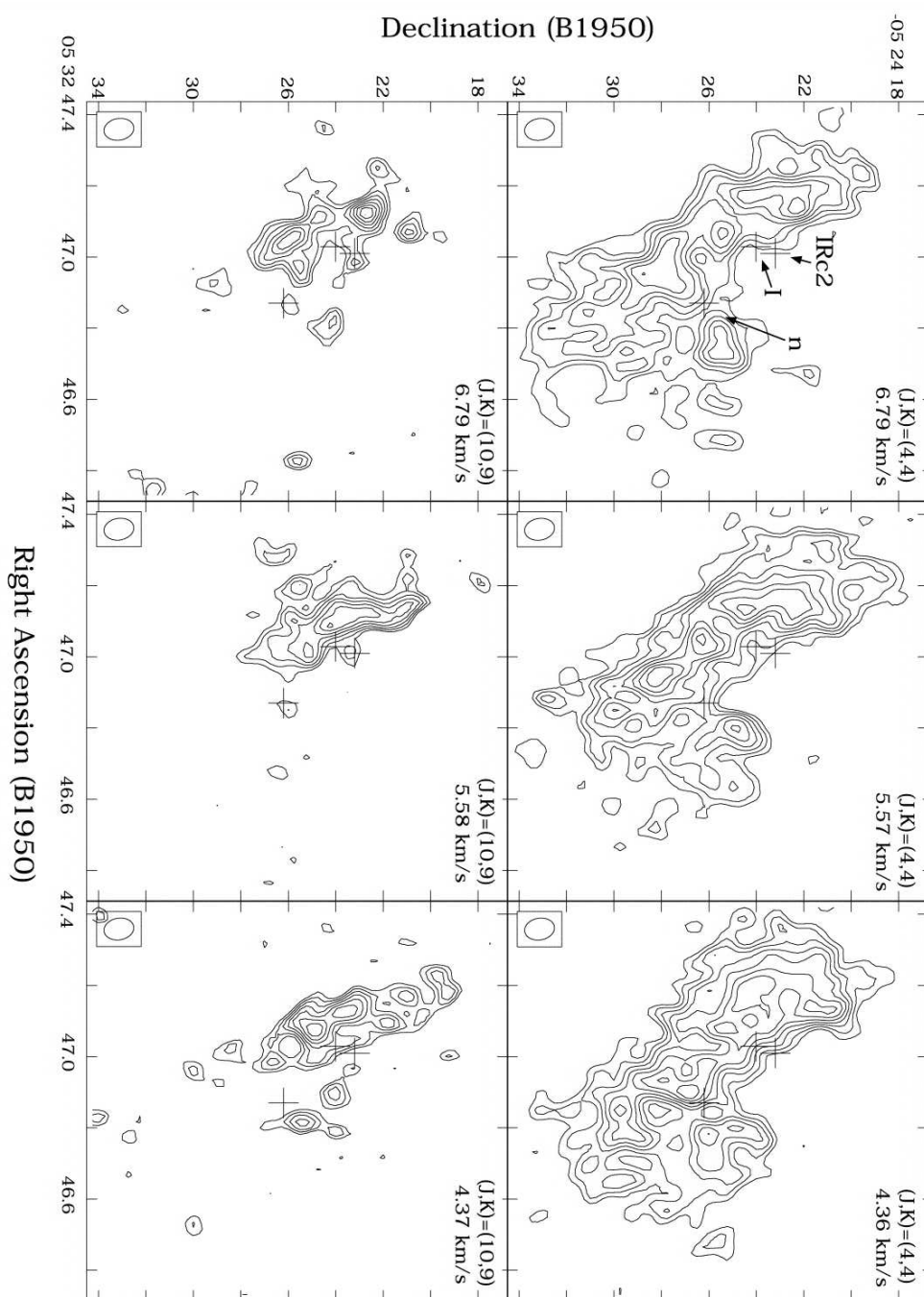
Figure 4.4 Right-panel: NH₃ maps by Wilson et al. (2000). Note that the distribution of the NH₃ gas is similar to the 870 μm continuum emission, i.e. have a cavity near the center. Source I and n are also at the edge of the NH₃ gas.
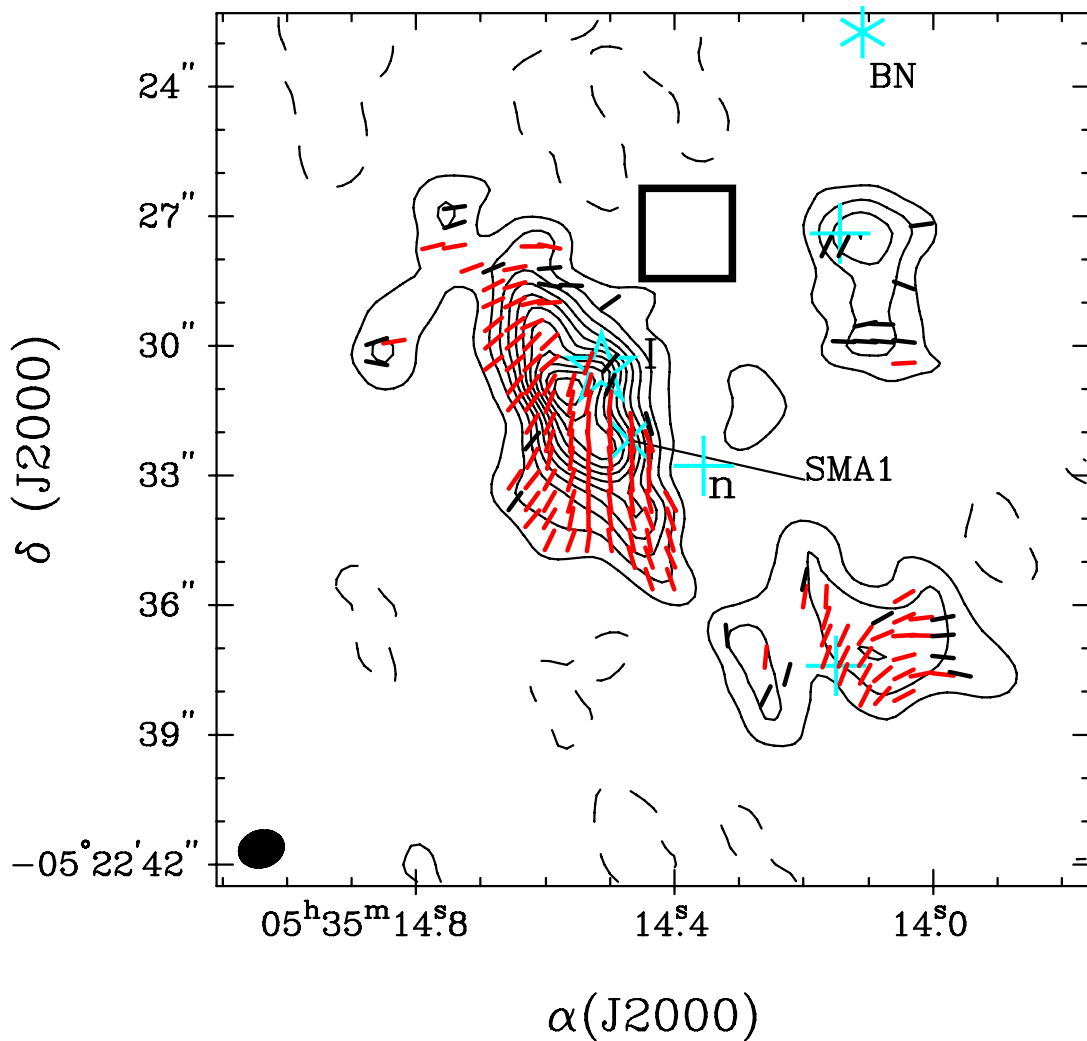
Figure 4.5 Left-panel: B field map in Orion BN/KL of the combined three tracks with uniform weighting. Contours are plotted from and step in 3σ, where 1 $\sigma = 53$ mJy beam^{-1}. All the symbols are the same as in Figure 1. The B field vectors are derived by rotating the polarization by 90° with identical length. The synthesized beam is $1''.1 \times 0''.8$ with a P.A. of $-72°$.
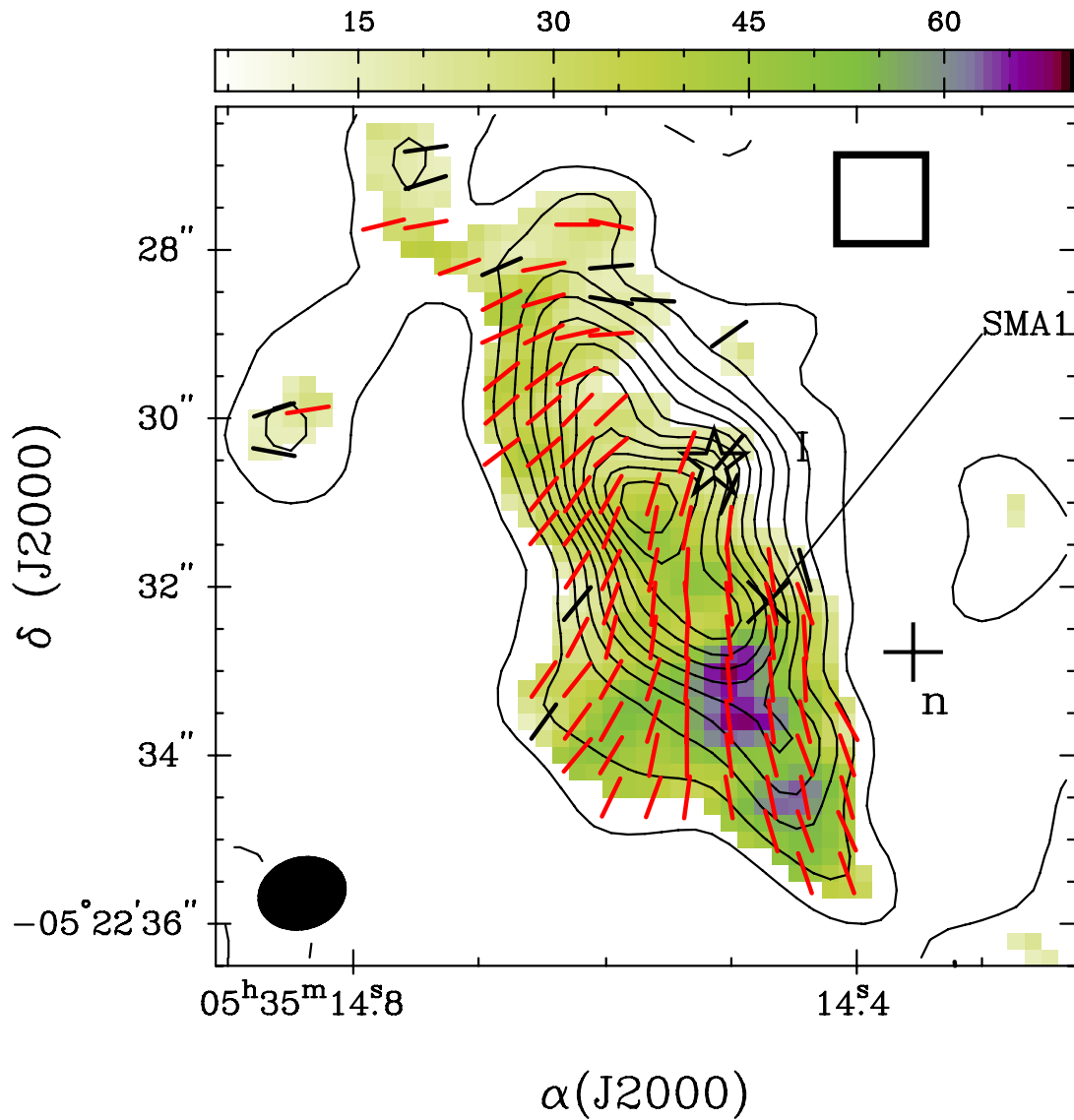
Figure 4.5 Right-panel: Zoomed-in B field map in Orion BN/KL of the combined tracks with uniform weighting. The polarized intensity map is shown in color scale in units of mJy beam^{-1} shown in color wedge. In both panels, the vectors are gridded with $0\rlap{.}''45$, $\sim$ half of the synthesize beam in order to show the variation of B field direction across each independent data points. Note that the B field direction vary smoothly by more than $90°$ across the *main dust ridge*.
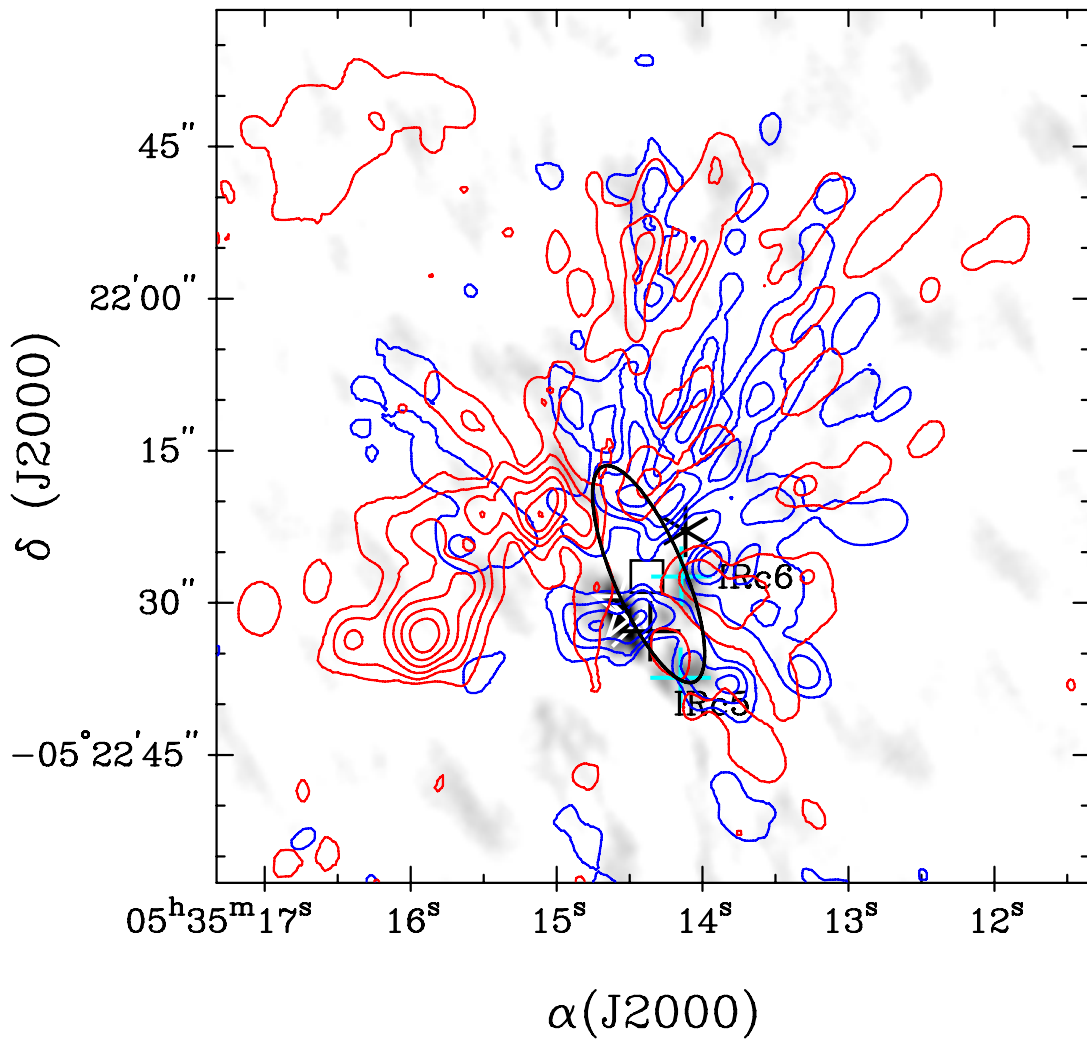
Figure 4.6 870 μm dust continuum (grey scale) of the combined tracks with natural weighting and CO outflows in blue and red contours by Zapata et al. (2009).

Chapter 5

Submillimeter Array Dust Polarization Image of the Ultracompact H II Region G5.89-0.39

Ya-Wen Tang[1,2], Paul T. P. Ho[2,3], Josep Miquel Girart[4], Ramprasad Rao[2], Patrick Koch[2], and Shih-Ping Lai[5]

[1]Department of Physics, National Taiwan University, No. 1, Sec. 4, Roosevelt Road, Taipei 10617

[2]Academia Sinica Institute of Astronomy and Astrophysics, P. B. Box 23-141, Taipei 10617

[3]Harvard-Smithsonian Center for Astrophysics,60 Garden Street Cambridge, MA 02138, U.S.A.

[4]Institut de Ciències de l'Espai (CSIC-IEEC), Campus UAB, Facultat de Ciencies, Torre C5 - parell 2, 08193 Bellaterra, Catalunya, Spain

[5]Institute of Astronomy and Department of Physics, National Tsing Hua University, 101, Section 2, Kuang Fu Road, Hsinchu, Taiwan 300, R. O. C.

Abstract

We report high angular resolution ($3''$) Submillimeter Array (SMA) observations of the molecular cloud associated with the Ultracompact H II region G5.89-0.39. Imaged dust continuum emission at 870μm reveals significant linear polarization. The position angles (P.A.s) of the polarization vary enormously but smoothly in a region of 2×10^4 AU. Based on the distribution of the P.A.s and the associated structures, the polarized emission can be separated roughly into two components. The component "x" is associated with a well-defined dust ridge at 870 μm, and is likely tracing a compressed B field. The component "o" is located at the periphery of the dust ridge and is probably from the original B field associated with a pre-existing extended structure. The global B field morphology in G5.89, as inferred from the P.A.s, is clearly disturbed by the expansion of the HII region and the molecular outflows. Using the Chandrasekhar−Fermi method, we estimate from the smoothness of the field structures that the B field strength in the plane of sky can be no more than 2−3 mG. We then compare the energy densities in the radiation, the B field, and the mechanical motions as deduced from the $C^{17}O$ 3-2 line emission. We conclude that the B field structures are already overwhelmed and dominated by the radiation, outflows, and turbulence from the newly formed massive stars.

Keywords: ISM: individual (G5.89-0.39) – ISM: magnetic fields – polarization – stars: formation

5.1   Introduction

One of the main puzzles in the study of star formation is the low star formation efficiency in molecular clouds. Since molecular clouds are known to be cold, the thermal pressure is small. Hence, if there are no other supporting forces against gravity, the free-fall timescale will be short and the star formation rate will be much higher than what is observed. Magnetic (B) fields have been suggested to play the primary role in providing a supporting force to slow down the collapsing process (see the reviews by Shu et al. 1999 and Mouschovias & Ciolek 1999). In these models, the B field is strong enough and has an orderly structure in the molecular cloud. The B field lines, which are anchored to the ionized particles, will then be dragged in along the direction of accretion, only when the ambipolar diffusion process allows the neutral component to slip pass the ionized component. In the

standard low-mass star formation model (Galli & Shu 1993; Fiedler & Mouschovias 1993), an hourglass-like B field morphology is expected with an accreting disk near the center of the pinched field. Alternatively, turbulence has also been suggested as a viable source of support against contraction (see reviews by Mac Low & Klessen 2004 and Elmegreen & Scalo 2004). The relative importance of B field and turbulence continues to be a hot topic as the two methods of support will lead to different scenarios for the star formation process.

Compared with the low-mass stars, the formation process of high-mass stars is relatively poorly understood. High mass star-forming regions, because of their rarity, are usually at larger distances and are always located in dense and massive regions because they are typically formed in a group. Hence, both poor resolution and complexity have hampered past observational studies. Furthermore, the environments of high-mass star-forming regions are very different from the low-mass case because of higher radiation intensity, higher temperature, and stronger gravitational fields. Will the B fields in massive star-forming sites have a similar morphology to the low-mass cases?

Polarized emission from dust grains can be used to study the B field in dense regions, because the dust grains are not spherical in shape. They are thought to be aligned with their minor axes parallel to the B field in most of the cases, even if the alignment is not magnetic (Lazarian 2007). Due to the differences in the emitted light perpendicular and parallel to the direction of alignment, the observed thermal dust emission will be polarized, the direction of polarization is then perpendicular to the B field. Although the alignment mechanism of the dust grains has been a difficult topic for decades (see review by Lazarian 2007), the radiation torques seem to be a promising mechanism to align the dust grains with the B field (e.g., Draine & Weingartner 1996; Lazarian & Hoang 2007). However, other processes such as mechanical alignments by outflows can also be important.

Polarized dust emission has been detected successfully at arcsecond scales. The best example might be the low-mass star-forming region NGC 1333 IRAS 4A (Girart, Rao & Marrone 2006), which reveals the classic predicted hourglass B field morphology. Results on the massive star-forming regions, such as W51 e1/e2 cores (Lai et al. 2001), NGC2024 FIR5 (Lai et al. 2002), DR21 (OH) (Lai et al. 2003), G30.79 FIR 10 (Cortes et al. 2006), and G34.4+0.23 MM (Cortes et al. 2008), typically show an organized and smooth B field morphology. However, this could be due to the lack of spatial resolution. Indeed, for the nearby high-mass cases such as Orion KL (Rao et al. 1998) and NGC 2071IR (Cortes,

Crutcher, & Matthews 2006), abrupt changes of the polarization direction on small physical scales have been seen, which may suggest mechanical alignments by outflows as proposed by these authors. Whether high-mass star-forming regions will all show complicated B field structures on small scales remains to be examined.

In this study, we report on one of the first SMA measurements of dust polarization for a high-mass star-forming region, G5.89-0.39 (hereafter, G5.89). The linearly polarized thermal dust emission is used to map the B field at $\sim 3''$ resolution, and the $C^{17}O$ 3-2 line is used to study the structure and kinematics of the dense molecular cloud. The description of the source, the observations and the data analysis, the results, and the discussion are in Sec. 2, 3, 4, and 5, respectively. The conclusions and summary are in Sec. 6.

5.2 Source Description

G5.89 is a shell-like Ultracompact HII (UC HII) region (Wood & Churchwell 1989) at a distance of 2 kpc (Acord et al. 1998). The UC HII region is 0.01 pc in size, and its dynamical age is 600 years, estimated from the expansion velocity (Acord et al. 1998). Observations of the K_s and L' magnitudes and color by Feldt et al. (2003) suggest that G5.89 contains an O5 V star.

Just as in other cases of massive stars, G5.89 contains most likely a cluster of stars. The detections of associated H_2O masers (Hofner & Churchwell 1996), OH masers (Stark et al. 2007; Fish et al. 2005) and class I CH_3OH masers (Kurtz et al. 2004), suggest that multiple stars have formed in this region. Furthermore, the morphology of the detected molecular outflows also suggests the presence of multiple driving sources, because different orientations are observed in different tracers. In CO 1-0, the large−scale outflow is almost in the east−west direction (Harvey & Forveille 1988; Watson et al. 2007). In $C^{34}S$ and the OH masers, the outflow is in the north-south direction (Cesaroni et al. 1991; Zijlstra et al. 1990). In SiO 5−4, the outflow is at a P.A. of 28° (Sollins et al. 2004). In the CO 3-2 line, the outflows (Hunter et al. 2008) are in the north−south direction and at the P.A. of 131°, and the latter one is associated with the Brγ outflow (Puga et al. 2006). In addition, the detected 870 μm emission has also been resolved into multiple peaks (labeled in Figure 1(a); Hunter et al. 2008). The different masers, the multiple outflows, and the multiple dust peaks, are all consistent with the formation of a cluster of young stars.

G5.89 should be expected to have a substantial impact on its environment. In terms of the total energy in outflows in this region, G5.89 is definitely one of the most powerful groups of outflows ever detected (Churchwell 1997).

5.3   Observation and Data Analysis

The observations were carried out on 2006 July 27 and 2006 September 10, 2006 using the Submillimeter Array (SMA; Ho, Moran & Lo (2004))[1] in the compact configuration, with seven of the eight antennas available for both tracks. The projected lengths of the baselines ranged from 6.5 to 70 kλ ($\lambda \approx 870$ μm). Therefore, our observational results are insensitive to structures larger than 39$''$. The SMA receivers are intrinsically linearly polarized, and only one polarization is available at the current time. Thus, quarter-wave plates (see Marrone & Rao 2008) were installed in order to convert the linear polarization (LP) to circular polarization (CP). The quarter-wave plates were rotated by 90° on a 5 minutes cycle using a Walsh function to switch between 16 steps in order to sample all the 4 Stokes parameters. The integration time spent on the source in each step was approximately 15 s. The overhead required in switching between the different states was approximately 5 s. In each cycle all four cross-correlations (LL, LR, RL, and RR) were each calculated 4 times. The data were then averaged over this complete cycle in order to obtain quasi-simultaneous dual polarization visibilities. We assume that the smearing due to the change of the polarization angles on this timescale is negligible.

The local oscillator frequency was tuned to 341.482 GHz. With a 2 GHz bandwidth in each sideband we were able to cover the frequency range from 345.5 to 347.5 GHz and from 335.5 to 337.5 GHz in the upper and lower sidebands, respectively. The correlator was set to a uniform frequency resolution of 0.65 MHz (~ 0.7 km s^{-1}) for both sidebands. While our main emphasis was to map the polarized continuum emission from the dust, we were also able to detect a number of molecular lines simultaneously. These results will be published separately.

Generally, the conversions of the LP to CP of the receivers are not perfect. This nonideal characteristic of the receiver will cause an unpolarized source to appear polarized, which is

---

known as instrumental polarization or leakage. Nevertheless, these leakage terms (see Sault, Hamaker, & Bregman 1996) can be calibrated by observing a strong linearly polarized quasar. In this study, the leakage and bandpass were calibrated by observing 3c279 for the first track and 3c454.3 for the second track. Both sources were observed for 2 hr while they were transiting in order to get the best coverage of parallactic angles. The leakage terms are frequency dependent, $\sim 1\%$ and $\sim 3\%$ for the upper and lower sidebands before the calibration, respectively. After calibration, the leakage is less than 0.5% in both sidebands. Besides the calibration for the polarization leakage, the amplitudes and phases were calibrated by observing the quasars 1626-298 and 1924-292 every 18 minutes. These two gain calibrators in both tracks were used because of the availabilities of the calibrators during the observations. Finally, the absolute flux scale was calibrated using Callisto.

The data were calibrated and analyzed using the MIRIAD package (Sault, Teuben, & Wright 1995). After the standard gain calibration, self-calibration was also performed by selecting the visibilities of G5.89 with uv distances longer than 30 kλ. As a result, the sidelobes and the noise level of the Stokes I image were reduced by a factor of 2. In order to get the images from the measured visibilities, the task INVERT in the MIRIAD package was used. The Stokes Q and U maps are crucial for the derivation of the polarization segments. We used the dirty maps of Q and U to derive the polarization to avoid a possible bias introduced from the CLEAN process. The Stokes I map shown in this paper is after CLEAN.

The Stokes I, Q and U images of the continuum were constructed with natural weighting in order to get a better S/N ratio for the polarization. The final synthesized beam is $3''.0 \times 1''.9$ with the natural weighting. The C^{17}O images are presented with a robust weighting 0.5 in order to get a higher angular resolution, and the synthesized beam is $2''.8 \times 1''.8$ with a P.A. of 13°. The noise levels of the I, Q, and U images are ~ 30, 5, and 5 mJy Beam^{-1}, respectively. Note that the noise level of the Stokes I image is much larger than the ones in the Stokes Q and U images. The large noise level of the I image is most likely due to the extended structure, which cannot be recovered with our limited and incomplete uv sampling. The strength (I_p) and percentage (P) of the linearly polarized emission are calculated from: $I_p^2 = Q^2 + U^2 - \sigma_{Q,U}^2$ and $P = I_p/\text{I}$, respectively. The term $\sigma_{Q,U}$ is the noise level of the Stokes Q and U images, and it is the bias correction due to the positive measure of I_p. The noise of I_p (σ_{I_p}) is thus 5 mJy Beam^{-1}. The presented polarization is

derived using the task IMPOL in the MIRIAD package, where the bias correction of σ_{I_p} is included.

5.4 Results

In this section, we present the observational results of the dust continuum and the dust polarization at 870μm, and the C^{17}O 3-2 emission line. No polarization was detected in the CO 3-2 emission line.

5.4.1 Continuum Emission

The total continuum emission at 870 μm, shown in Figure 1(a), is resolved with a total integrated flux density 12.6±1.3 Jy. In general, the morphology of the continuum emission at 870μm is similar to the emission at 1.3 mm by Sollins et al. (2004). However, the 870μm emission peaks at $\sim 1''$ west of the position of the O5 star, which is offset toward the northwest by $\sim 1''.7$ from the peak of the 1.3 mm continuum emission. Because there is still a significant contribution from the free−free emission to the continuum at 870 μm and at 1.3mm, the differences between the 870 μm and 1.3 mm maps most likely result from the increasing contribution from the dust emission as compared to the free−free emission at shorter wavelengths. Due to the importance of a correct dust continuum image in the derivation of the polarization, we describe here how the free−free continuum was estimated and removed from the 870μm total continuum emission.

Removing the free−free emission

The free−free continuum at 2cm (shown in a color scale in Figure 1 (a) and (b)) was imaged from the Very Large Array (VLA) archival database observed on 1986 August 7. The VLA synthesized beam of the 2 cm free−free image is $0''.92 \times 0''.45$ with natural weighting of the uv data. Since the free−free shell is expanding at a rate of 2.5 mas yr^{-1} (Acord et al. 1998), at a distance of 2 kpc, this expansion motion over the intervening 20 yr is negligible within the synthesized beam of our SMA observation.

The contribution from the free−free continuum was removed by the following steps. First, we adopted a spectral index $\alpha = -0.154$ calculated in Hunter et al. (2008) for the free−free continuum emission between 2 cm and 870 μm. The resulting estimated free−free

continuum strength at $870\mu m$ was 4.9 Jy. Second, we further assumed that the morphology of the free−free continuum at 870 μm and at 2cm were identical. We then smoothed the VLA 2cm image to the SMA resolution and scaled the total flux density to 4.9 Jy. Finally, we subtracted this image from the total continuum at 870 μm. The resultant 870 μm dust continuum image is shown in Figure 1(b). The total flux density of the dust continuum is therefore 7.7±0.8 Jy.

Dust continuum: mass and morphology

The corresponding gas mass (M_{gas}) was calculated from the flux density of the dust continuum at 870 μm following Lis et al. (1998):

$$M_{gas} = \frac{2\lambda^3 Ra\rho d^2}{3hcQ(\lambda)J(\lambda, T_d)}S(\lambda). \tag{5.1}$$

Here, we assumed a gas-to-dust mass ratio R of 100, a grain radius a of 0.1 μm, a mean grain mass density ρ of 3 g cm^{-3}, a distance to the source d of 2 kpc, a dust temperature T_d of 44 K, an observed flux density $S(\lambda)$ of 7.7 Jy, the Planck factor $J(\lambda, T_d) = [exp(hc/\lambda kT_d) - 1]^{-1}$. h, c and k are the Planck constant, the speed of light, and the Boltzmann constant, respectively. The grain emissivity $Q(\lambda)$ was estimated to be 1.5×10^{-5} after assuming $Q(350\mu m)$ of 7.5×10^{-4} and β of 2 (cold dust component), and using the relation $Q(\lambda) = Q(350\mu m)(350\mu m/\lambda)^{\beta}$ (Hunter et al. 2000). As suggested in the same paper, the dust emission can be modeled by two temperature components, with the emission dominated by the colder component at $T_d \sim 44$ K. We adopted this value for T_d, and therefore, the mass given here refers only to the cold component and is an underestimate of the total mass. The derived gas mass of the dust core M_{gas} is ~ 300 M$_{\odot}$, with a number density $n_{H_2} = 5.3 \times 10^6$ cm^{-3} averaged over the emission region. The sizescale along the line of sight is assumed to be 0.13 pc, which is the diameter of the circle with the equivalent emission area.

The dust emission presented in Figure 1(b) has an extension toward the northeast (NE), east and southwest(SW), and has a steep roll−off on the northwestern(NW) edge of the ridge. In the higher angular resolution (0.″8) observation at the same wavelength by Hunter et al. (2008), the dust core is resolved into 5 peaks, where the two strongest peaks align in the north-south direction to the west of the O5 star. The dust continuum emission associated with SMA-N, SMA-1 and SMA-2 is called *sharp dust ridge* hereafter because of its strong emission and its morphology. There is no peak detected at the position of the O5

star. It is likely that the O5 star is located in a dust-free cavity, as proposed by Feldt et al. (1999) and Hunter et al. (2008).

5.4.2   Dust polarization

We first compare the dust polarization derived from the 870 μm total continuum (Figure 1(c)) and from the 870 μm dust continuum (Figure 1(d)). In both cases the derived polarization is at the same location with the same P.A.s. The only difference of the polarization in Figures 1(c) and (d) is that the percentage of polarization near the H II region is increased in Figure 1(d). This is because of the fact that the free−free continuum is not polarized, and the Q and U components are not affected by the free−free continuum subtraction. Therefore, the expected polarization percentage will increase when the free−free continuum is removed from the 870 μm continuum. The total detected polarized intensity I_p is 59 mJy. All the polarization shown in the figures besides Figure 1(c) is calculated from the derived dust continuum image. The offset positions, percentages and P.A.s of the polarization segments are listed in Table 1.

Morphology of the detected polarization

The polarized emission is not uniformly distributed (Figure 2(a)). Detected polarizations at $2\sigma_{I_p}$ are shown as blue segments, and detections above $3\sigma_{I_p}$ are shown by red segments (Figure 2(b)). Most of the polarized emission is located in the northern half of the dust core close to the HII region and appears as four patches, mostly with $\sigma_{I_p} \geq 3$ (Figure 2(a) in a color scale). There is a sharp gap where no polarization is detected extending from the NE to the SW across the O star. The southern half of the dust core is free of polarization, except for a few positions at the edge of the dust core. However, the polarization in the southern half of the dust core is at 2 to $3\sigma_{I_p}$ level only. We will focus our discussions on the more significant detections in the core of the cloud.

We separate the polarized emission into two groups. We are guided principally by the fact that one group is associated with the periphery of the total dust emission, while the other group tracks the strongest parts of the total dust emission. The polarized patches to the east of the O star and to the west of the Brγ outflow source have similar P.A.s of $\sim 50°$ (Figure 2(b)). These polarization segments are located at the fainter edges of the higher resolution 870 μm dust continuum image (Figure 2(c); Hunter et al. 2008) and

at the less steep part of the $3''$ resolution image (this paper). This may suggest that this polarization originates from a more extended overall structure, rather than from the detected condensations. Therefore, these polarization segments are suggested to be the component "o" (defined in the following section). The rest of the polarization in the northern part is all next to the sharp gap where no polarization is detected. Most of the polarization is on the 870μm *sharp dust ridge* observed with $0.''8$ resolution, except for the ones at the NE and SW ends where the polarization patches stretch toward the extended structure. At these NE and SW ends, the polarization is probably the sum of the extended and the condensed structures. These polarization segments are suggested to belong to the component "x".

The $0.''8$ resolution observations show that there is a hole in the southern part of the detected dust continuum. This hole is not resolved with the $3''$ synthesized beam of our map. That may explain why polarization is not detected at this position. Here, and also for the dust ridge sharply defined with $0.''8$ resolution, the dust polarization is sensitive to the underlying structures and can help to identify unresolved features which are smaller than our resolution.

Distribution of the polarization segments

The detected P.A.s vary enormously over the entire map, ranging from $-60°$ to $61°$ (Figure 3(a)). Nevertheless, they vary smoothly along the dust ridge and show organized patches. We have roughly separated the polarized emission into two different components according to their locations (as discussed in Sec. 4.2.1) and their P.A.s. The "o" component is probably from an extended structure with P.A.s ranging from $33°$ to $61°$. The mean P.A. weighted with the observational uncertainties of component "o" is $49\pm3°$, with a standard deviation of $11°$. The "x" component associated with the *sharp dust ridge* has P.A.s ranging from $-60°$ to $4°$. Its weighted mean P.A. is $-24\pm1°$, with a standard deviation of $18°$. If the polarization were not separated into two components, the weighted mean P.A. is $-9°$ with a standard deviation of $39°$.

The relation between the percentage of polarization and the intensity is shown in Fig. 3(b). The percentage of polarization decreases towards the denser regions, which has already been seen for other star formation sites, such as the ones listed in Sec. 1. This is possibly due to a decreasing alignment efficiency in high-density regions, because the radiation torques are relatively ineffective (Lazarian & Hoang 2007). It can also be due to the geometrical

effects, such as differences in the viewing angles (Gonçalves et al. 2005), or due to the results from averaging over a more complicated underlying field morphology.

5.4.3 $C^{17}O$ 3-2 emission line

In order to trace the physical environments and the gas kinematics in G5.89, we choose to use the $C^{17}O$ 3-2 emission line because of its relatively simple chemistry. The critical density of $C^{17}O$ 3-2 is $\sim 10^5$ cm^{-3}, assuming a cross-section of 10^{-16} cm^{-2} and a velocity of 1 km s^{-1}, and therefore, it will trace both the relative lower ($n_{H_2} \sim 10^5$ cm^{-3}) and higher ($n_{H_2} \sim 10^6$ cm^{-3}) density regions. Although its critical density is much smaller than the estimated gas density of 5.3×10^6 cm^{-3} from the dust continuum, it is apparently tracing the same regions as the dust continuum because of the similar morphology of the integrated intensity image, shown in the next section. We therefore assume that the kinematics traced by $C^{17}O$ represents the bulk majority of the molecular cloud and that it is well correlated with the dust continuum.

Morphology of $C^{17}O$ 3-2 emission

The emission of the $C^{17}O$ 3-2 line covers a large velocity range, from -7 to 28 km s^{-1}, as shown in the channel maps in Figure 4. The majority of the gas traced by the $C^{17}O$ 3-2 line is relatively quiescent and has a morphology similar to the 870μm dust continuum emission. Besides the components which trace the dust continuum, an arc feature is seen in the south-east corner of the panel covering $10-15$ km s^{-1}. There is no associated 870μm dust continuum detected at this location, probably due to the low total column density or mass of this feature. Another feature seen in the more quiescent gas is the clump extending towards the south of the dust core (see the panel covering $6-10$ km s^{-1} in Figure 4). This clump has a similar morphology as seen in the 870 μm dust continuum where no polarization has been found. At the higher velocity ends, i.e. from -7 to -3 km s^{-1} and from 23 to 28 km s^{-1}, the emission appears at the 870μm dust ridge. This suggests that at the *sharp dust ridge*, there are high$-$velocity components besides the majority of quiescent material. Furthermore, the brightest HII features appear correlated with the strongest $C^{17}O$ emission, especially at low velocities ($v_{lsr} = 6$ to 15 km s^{-1}), which may point toward an interaction between the molecular gas and the H II region.

The total integrated intensity (zeroth moment) image (Figure 5(upper-panel) of the

$C^{17}O$ 3-2 emission line shows a similar morphology as the 870 μm dust continuum. The morphology of the $C^{17}O$ gas to the west of the O star is similar to the dense dust ridge, i.e. there is an extension from north to south. The steep roll off of the dust continuum in the NW and an extension from NE to the west of the O star are also seen in $C^{17}O$. Besides these similar features to the dust continuum, a strong $C^{17}O$ peak is found at position A, where no dust continuum peak is detected. This feature A likely does not have much mass, and we will not discuss its properties further in this paper.

Total gas mass from $C^{17}O$ 3-2 line

The total gas mass M_{gas} in this region can be derived from the $C^{17}O$ 3-2 line. This provides a complementary estimate, which is independent from the mass derived from the dust continuum in Eq. 1. Assuming that the observed $C^{17}O$ 3-2 line is optically thin and in local thermal equilibrium (LTE), the mean column density $N_{C^{17}O}$ is calculated following the standard derivation of radiative transfer (see Rohlfs & Wilson 2004):

$$N_{C^{17}O} = 1.3 \times 10^{13} \times \frac{T_{R3-2}\triangle V}{D(n, T_{\mathrm{k}})} \tag{5.2}$$

Here, the $T_{R3-2}\triangle V$ term is the mean flux density of the entire emission region in K km s^{-1}. The D parameter depends on the number density n and the kinetic temperature T_{k} and is given by

$$D(n, T_{\mathrm{k}}) = f_2[J_\nu(T_{\mathrm{ex}}) - J_\nu(T_{\mathrm{bk}})][1 - exp(-16.597/T_{\mathrm{ex}})],$$

where f_2 is the population fraction of $C^{17}O$ molecules in the $J = 2$ state. T_{ex} and T_{bk} are the excitation and background temperatures, respectively. The adopted value of D is 1.5 from the LVG calculation by Choi, Evans II & Jaffe (1993). In their calculation, this D value is correct within a factor of 2 for $10 < T_{\mathrm{k}} < 200$ K in the LTE condition. The total gas mass M_{gas} is given by

$$M_{gas} = \mu m_{H_2} d^2 \Omega \frac{N_{C^{17}O}}{X_{C^{17}O}}. \tag{5.3}$$

Here μ is 1.3, which is a correction factor for elements heavier than hydrogen. m_{H_2} is the mass of a hydrogen molecule. d and Ω are the distance to the source and the solid angle of the emission, respectively. The $C^{17}O$ abundance $X_{C^{17}O}$ is assumed to be 5×10^{-8} (Frerking et al. 1982; Kramer et al. 1999). The derived mean $N_{C^{17}O}$ is 2×10^{16} cm^{-2}. The

mean gas number density n_{H_2} is 1.6×10^6 cm^{-3}, assuming the size of the molecular cloud is 0.13 pc along the line of sight, which is the diameter of the circle with the equivalent emission area. The derived M_{gas} from the $C^{17}O$ 3-2 emission is $\sim$100 $M_\odot$.

The gas mass calculated using the $C^{17}O$ 3-2 line is a factor of 3 smaller than the value derived from the dust continuum (300 $M_\odot$). This difference has also been seen in the $C^{17}O$ survey towards the UC H II regions by Hofner et al. (2000). Their M_{gas} estimated from the measurement of the $C^{17}O$ emission tends to be a factor of 2 smaller than the measurement from the dust continuum. The uncertainty of the estimate here possibly results from the assumptions of the dust emissivity, the gas to dust ratio, the abundance of the $C^{17}O$, and from the possibility that $C^{17}O$ might not be entirely optically thin.

5.5 Discussion

We discuss the possible reasons of the nondetected polarization in the CO 3-2 line in the next paragraph. In order to interpret our results, we have also analyzed the kinematics of the molecular cloud in G5.89 using the $C^{17}O$ 3-2 first and second moment images, the position$-$velocity (PV) diagrams, and the spectra at various positions. The strength of the B field inferred from the dust polarization is calculated using the Chandrasekhar$-$Fermi method. A possible scenario of the dust polarization is discussed based on the calculation of the mass$-$to$-$flux ratio and the energy density.

5.5.1 CO 3-2 polarization

Under the presence of the B field, the molecular lines can be linearly polarized if the molecules are immersed in an anisotropic radiation field and the rate of radiative transitions is at least comparable with the rate of collisional transitions. This effect is called the Goldreich$-$Kylafis (G$-$K) effect (Goldreich & Kylafis (1981); Kylafis (1983)). The G$-$K effect provides a viable way to probe the B field structure of the molecular cores, because the polarization direction is either parallel or perpendicular to the B field. The degree of the polarization depends on several factors: the degree of anisotropy, the ratio of the collision rate to the radiative rate, the optical depth of the line, and the angle between the line of sight, the B field, and the axis of symmetry of the velocity field. In general, the maximum polarization occurs when the line optical depth is $\sim$ 1 (Deguchi & Watson 1984). Although

the predicted polarization can be as high as 10%−20%, the G−K effect is only detected in a limited number of star formation sites: the molecular outflow as traced by the CO molecular lines with BIMA in the source NGC 1333 IRAS 4A (Girart & Crutcher 1999), and the outer low-density envelope in G34.4+0.23 MM (Cortes et al. 2008), G30.79 FIR 10 (Cortes & Crutcher 2006), and DR 21(OH) (Lai et al. 2003). High−resolution observations are required to separate regions with different physical conditions.

We have checked the polarization in the molecular lines. No detection in the CO 3-2 and other emission lines was found. The molecular outflows as seen in the CO 3-2 and SiO 8-7 emission lines will be shown in Tang et al. (in preparation). We briefly discuss the possible reasons for the lack of polarization in the molecular lines here.

One possible reason is the high optical depth (τ) of the CO 3-2 line. It has been shown by Goldreich and Kylafis (1981) that the percentage of polarization depends on the value of τ, decreasing rapidly as the line becomes optically thick. When corrected for multi-level populations, Deguchi & Watson (1984) suggested that the percentage of polarization decreases further by about a factor of 2. In G5.89, τ of the CO 3-2 line is $\sim$10 at $v_{\mathrm{lsr}} = 25$ km s^{-1} (Choi et al. 1993), which is the channel where the emission is strongest in our SMA observation. Note that this emission does not peak at the systematic velocity (v_{sys}) of 9.4 km s^{-1}, which is most likely due to the missing extended structure which our observation cannot reconstruct. We then estimate that the expected percentage of polarization will be about 1.5%, or a polarized flux density of 0.5 Jy Beam^{-1} for the CO 3-2 line, which is below our sensitivity.

Besides an optimum τ, the anisotropic physical conditions, such as the velocity gradient and the density of the molecular cloud, are needed to produce a polarized component from the spectral line. The fraction and direction of polarization will also change as a function of τ if there are external radiation sources nearby (Cortes et al. 2005). Here, we are not able to distinguish between these possible reasons.

5.5.2   The kinematics traced by C^{17}O 3-2 emission line

As shown in Sec. 4.3.1, high-velocity components of the molecular gas are traced by the C^{17}O 3-2 emission near the HII region. Here, we examine the kinematics in G5.89.

The intensity weighted velocity (first moment) image provides the information on the line-of-sight motion (mean velocity). The molecular cloud is red-shifted with respect to the

$v_{\rm sys}$ of 9.4 (km s^{-1}) in the NW (position B) and SE (position D) of the O5 star (middle panel of Figure 5). Next to the south of the O5 star, a blue-shifted clump with respect to 9.4 km s^{-1} is detected. The molecular cloud in G5.89 has significant variations in mean velocity within a radius of 5$''$ around the O5 star.

To further investigate the relative motions, the total velocity dispersion δv_{total} (second moment) image is also presented (Figure 5(lower-panel)). δv_{total} is related to the spectral line width at full width half-maximum (FWHM) for a Gaussian line profile: FWHM = 2.355δv_{total}. Around the HII region in G5.89, δv_{total} has a maximum of ~ 6 km s^{-1} (FWHM ~ 14 km s^{-1}) near the O5 star and decreases in the regions away from the O5 star. In terms of mean velocity and velocity dispersion, the molecular gas near the H II region is clearly disturbed. Besides the feature near the H II region, the velocity dispersion along the *sharp dust ridge* is larger and has a correspondent extension (NE−SW), which suggests that the molecular cloud along the *sharp dust ridge* is more turbulent (see also Sec. 4.3.1). This enhanced turbulent motion supports our separation of the polarized emission into component "o" and "x" in Sec. 4.2.2. These two polarized components are most likely tracing different physical environments.

The PV plots cut at various P.A.s at the position of the O5 star and cut along the extension in the NE and SW direction on the second moment image (white segments on the lower panel of Figure 5) are shown in Figure 6. The strongest emission is at v_{sys} with an extension of 18$''$, which suggests that the majority of the gas is quiescent. Besides the quiescent gas, a ring-like structure, indicated as red-dashed ellipses in Figure 6, can be seen clearly, especially at the P.A. of 60°-100°. Both an infalling motion (e.g. Ho & Young 1996) and an expansion can produce a ring-like structure in the PV plots. In an infalling motion, the expected free-fall velocity is ~ 5 km s^{-1} for a central mass of 50 M$_\odot$ at a distance of 2$''$ from the central star. This is smaller than the value measured in the ring-like structure in G5.89. This C^{17}O 3-2 ring-like structure in the PV plots is therefore more likely tracing the expansion along with the HII region because of its high velocity (± 10 km s^{-1}) and its dimension (2$''$ in radius). However, the ring structure is not complete. This may be because the material surrounding the H II region is not homogeneously distributed, or the H II region is not completely surrounded by the molecular gas.

Besides the expansion motion along with the HII region, there are higher velocity components extending up to 30 km s^{-1} (red-shifted) and −5 km s^{-1} (blue-shifted) (Figure 6).

The high-velocity structure extending from the position of $2\rlap{.}''5$ to the velocity of $\sim$30 km s^{-1} is clearly seen in the PV cuts at P.A. of 0°-40° (indicated as cyan arcs in Figure 6). These high-velocity components are probably due to the sweeping motion of the molecular outflows in G5.89, because there is no other likely energy source which can move the material to such a high velocity. From the PV plots at the position of the O5 star at various P.A.s and the PV plot cut along the *sharp dust ridge*, we conclude that the molecular cloud is most likely both expanding along with the H II region and being swept-up by the molecular outflows, all in addition to the bulk of the quiescent gas.

The examination of the spectra at various positions also helps to analyze the kinematics in G5.89. The spectra (Figure 7) near the H II ring (positions C, D, F, G and H) have broad line widths. Furthermore, the spectra are not Gaussian-like, or with distinct components at high velocities ($\pm$ 10 km s^{-1}). At position F and H, both spectra show a strong peak at v_{sys}. The high-velocity wing at the position F is red-shifted, and it is blue-shifted at position H. This is consistent with the NS molecular outflow. The molecular gas near the positions E and I is more quiescent because of its narrow line width. The spectrum taken at position I has a FWHM of 4 km s^{-1} and a peak intensity at $\sim$ 7 km s^{-1}. Comparing with the spectra at other positions, the cloud around the position I is relatively quiescent and unaffected by the H II region or the outflows. This cloud in the south near the position I may be a more independent component which is further separated along the line of sight. We conclude that the C^{17}O 3-2 spectra demonstrate that the kinematics and morphology have been strongly affected by the expansion of the H II region. The nearly circular structure in the PV plots, and in the channel maps near the systemic velocity, as well as the spectra, suggest that a significant part of the mass has been pushed by the H II region. An impact from the molecular outflow can also be seen in the PV plots and spectra.

5.5.3   Estimate of the B field strength

The B field strength projected in the plane of sky (B$_\perp$) can be estimated by means of the Chandrasekhar−Fermi (CF) method (Chandrasekhar & Fermi 1953; Falceta-Gonçalves, Lazarian, & Kowal 2008). In general, the CF method can be applied to both dust and line polarization measurements. We apply the CF method only to the dust continuum polarization, because there is no line polarization detected in this paper. Although the dust grains can also be mechanically aligned, the existing observational evidence in NGC 1333

IRAS4A (Girart et al. 2006) demonstrates that the dust grains can align with the B field in the low-mass star formation regions. Here, we assume that the dust grains also align with the B field in G5.89.

The strength of $B_\perp$ can be calculated from

$$B_\perp = Q\sqrt{4\pi\bar{\rho}}\frac{\delta v_{los,A}}{\delta\phi} = 63\sqrt{n_{H_2}}\frac{\delta v_{los,A}}{\delta\phi}. \tag{5.4}$$

Here, $B_\perp$ is in the unit of mG. The term Q is a dimensionless parameter smaller than 1. Q is $\sim$0.5 (Ostriker, Stone & Gammie 2001), depending on the inhomogeneities within the cloud, the anisotropies of the velocity perturbations, the observational resolution and the differential averaging along the line of sight. The term $\bar{\rho}$ is the mean density. $\delta\phi$ is the dispersion of the polarization angles in units of degree. $\delta v_{los,A}$ is the velocity dispersion along the line of sight in units of km s^{-1}, which is associated with the Alfvénic motion. n_{H2} is the number density of H_2 molecules in units of 10^7 cm^{-3}. It has been shown numerically that the CF method is a good approximation for $\delta\phi < 25^\circ$ (Ostriker, Stone, & Gammie (2001)).

$\delta v_{los,A}$ is estimated from δv_{total} in the second moment image (lower panel in Figure 5). δv_{total} contains the information of the dispersions caused by the Alfvénic turbulent motion ($\delta v_{los,A}$) and the dispersions caused by the H II expansion and outflow motions (δv_{bulk}). The relation of these three components is

$$\delta v_{total} \sim \sqrt{\delta v_{los,A}^2 + \delta v_{bulk}^2}.$$

Here, we neglect the minor contributions from the thermal Doppler motions. The measured δv_{total} at the positions of detected polarization are listed in Table 1. δv_{total} is in the range of $1-6$ km s^{-1}. However, the molecular gas near the H II region is clearly disturbed by both the H II expansion and the molecular outflows (see Sec. 4.3.1 and 5.2). Therefore, the detected δv_{total} at these positions is dominated by the bulk motion. Since δv_{total} in the relatively quiescent regions is more likely tracing the Alfvénic motion only, we adopt the minimum value δv_{total} of 1 km s^{-1} at these positions for $\delta v_{los,A}$ in order to derive $B_\perp$.

The term n_{H_2} is $\sim$3$\times10^6$ cm^{-3}, estimated from the averaged n_{H_2} from the 870μm dust continuum and the C^{17}O 3-2 line emission (Sec. 4.1.2 and Sec. 4.3.2). $\delta\phi$ in Eq. 4 can be extracted from the observed standard deviation of the P.A.s $\delta\phi_{obs}$. $\delta\phi_{obs}$ contains both the observational uncertainty $\sigma_{\phi,obs}$ and $\delta\phi$. The relation is $\delta\phi_{obs}^2 = \delta\phi^2 + \sigma_{\phi,obs}^2$. Since the polarization in G5.89 results probably from two different systems (discussed in Sec.

4.2.1 and 4.2.2), it is more reasonable to separate these two groups when deriving $\delta\phi$. The derived $\sigma_{\phi,obs}$, $\delta\phi_{obs}$, and $\delta\phi$ are 3°, 11°, and $\sim$11° for component "o", and 2°, 18°, and $\sim$18° for component "x", respectively. By using Eq. (4), the derived $B_\perp$ is 3 mG and 2 mG for component "o" and "x", respectively.

The estimated $B_\perp$ is highly uncertain. Due to the bulk motions, it is difficult to extract the $\delta v_{los,A}$ component from the observed δv_{total}. The uncertainty introduced from $\delta v_{los,A}$ is within a factor of 6. Of course, the grouping of "o" and "x" components of the polarization, as motivated in Sec. 4.2.1, 4.2.2, and 5.2, is not a unique interpretation. If $\delta\phi$ is calculated without grouping, a more complex model of the larger scale B field morphology is needed to calculate the deviation due to the Alfvénic motion. More observations with sufficient uv coverage are required to establish such a model. Based on the standard deviation $\delta\phi$ of 39° from the detected polarization without subtracting the larger scale B field and without grouping, the calculated lower limit of $B_\perp$ is $\sim$1mG. Therefore, the estimated $B_\perp$ from the grouping of components "o" and "x" seems reasonable. The value is comparable to the ones estimated via the CF method in other massive star formation regions with an angular resolution of a few arcseconds: $\sim$1 mG in DR 21(OH) (Lai et al. 2003) and $\sim$1.7 mG in G30.79 FIR 10 (Cortes & Crutcher 2006). Moreover, $B_\perp$ is similar to $B_\parallel$ measured from the Zeeman pairs of the OH masers by Stark et al. (2007), ranging from -2 to 2 mG. Although $B_\parallel$ measured from OH masers is most likely tracing special physical conditions, such as shocks or dense regions, it is the only direct measurement of $B_\parallel$ in G5.89, and hence, is of interest to compare. Assuming $B_\perp$ and $B_\parallel$ have the same strengths of 2 mG, the total B field strength in G5.89 is $\sim$ 3 mG.

5.5.4 Collapsing cloud or not?

The mass-to-flux ratio λ, a crucial parameter for the magnetic support/ambipolar diffusion model, can be calculated from $\lambda = 7.6 \times 10^{-21} \frac{N_{H_2}}{B}$ (Mouschovias & Spitzer 1976; Nakano & Nakamura 1978). N_{H_2} is in cm^{-2}. B is the total B-field strength in μG. In the case of $\lambda < 1$, the cloud is in a subcritical stage and magnetically supported. In the case of $\lambda > 1$, the cloud is in a collapsing stage.

Since there is no observation of the B field strength as a function of position in the entire cloud, we assume that the B field is uniform with the strength of 3 mG in the entire cloud when λ is calculated. For consistency, when comparing with the kinetic pressure in

the next section, N_{H_2} is derived from the $C^{17}O$ 3-2 emission (Section 4.3.2). The derived λ in G5.89 is >1 in most parts of the molecular cloud, as shown in the upper panel of Figure 8. If the statistical geometrical correction factor of 1/3 is considered (Crutcher 2004), the corrected mass-to-flux ratio λ_{corr} in the *sharp dust ridge* is still close to 1, whereas at the positions of the component "o" and the outer part, it is much smaller than 1. This suggests that G5.89 is probably in a supercritical phase near the H II region and in a subcritical phase in the outer part of the dust core.

This conclusion is based on the assumption that the B field in the entire cloud is uniform with a strength of 3 mG. This assumption seems to be crucial at first glance. However, the derived λ increases from 0.1 to 2.5 toward the UC H II region, which is due to the high contrast of the column density across the cloud. Unless the actual B field strength differs by a factor of 25 across the region and compensates for the contrast in the column density, such a variation of λ in G5.89 is indeed possible.

5.5.5 Compressed field?

The coincident location of the detected polarization of component "x" and the *sharp dust ridge* is quite interesting. One possible scenario is that the B field lines are compressed by the shock front, i.e. HII expansion. In a magnetized large molecular cloud with a B field traced by a component "o", and with a shock sent out from the east of the narrow dust ridge, we expect a rapid change of the polarization P.A.. This is similar to the results in magnetohydrodynamic simulations by Krumholz et al. (2007). Because of our limited angular resolution, polarization with a large dispersion in the P.A.s over a small physical scale will be averaged out within the synthesized beam. In our result, in fact, there is a gap where polarized emission is not detected right next to the *sharp dust ridge*, and a series of OH masers are detected in this gap. Note that the OH masers are most likely from the shock front. From the discussion in Sec. 5.2, evidence for the molecular cloud expanding with the HII region is found in the molecular gas traced by the $C^{17}O$ 3-2 emission. The $870\mu m$ *sharp dust ridge* can be explained by the swept-up material along with the molecular gas from the HII expansion. In this scenario, the component "o" is tracing the B field in the preshock region, while the "x" component is tracing the compressed field.

However, the swept-up flux density (summation of the flux density of SMA-N, SMA-1 and SMA-2 reported in Hunter et al. 2008) is $\sim$ 20% of the total detected flux density in

this paper. This requires a huge amount of energy to sweep up the material with this mass. Is the radiation pressure (P_{rad}) from the central star large enough to overcome the kinetic pressure (P_{kin}) and the B field pressure (P_{B})? Here, we compare these pressure terms.

P_{rad} can be calculated from the luminosity in G5.89 following the equation: $P_{\mathrm{rad}} = \frac{L}{cA}$, where L, c and A are the luminosity, speed of light and the area, respectively. Since the G5.89 region is dense, most of the radiation is absorbed and redistributed into the surrounding material. The total far infrared luminosity of G5.89 is $3 \times 10^5 L_\odot$ (Emerson, Jennings, & Moorwood 1973) and the radius of the HII region at 2cm is $\sim 2''$ (4000 AU). The energy density and hence, the radiation pressure (P_{rad}) in the sphere with a radius of $2''$ is 8.5×10^{-7} dyne cm^{-2}.

P_{kin} is calculated by using the zeroth moment (MOM0) and second moment (MOM2) images of the C^{17}O 3-2 line:

$$P_{kin} = \frac{1}{2}\rho \delta v_{total}^2 = 3.4 \times 10^{-9} \times (\mathrm{MOM0}) \times (\mathrm{MOM2})^2 \qquad (5.5)$$

where P_{kin} is in dyne cm^{-2}, ρ is the gas density in g cm^{-3} and δv_{total} is the velocity dispersion in cm s^{-1}, MOM0 is in units of K km s^{-1}, and MOM2 is in units of km s^{-1}. ρ is calculated following Sec. 4.3.2, with the size of 0.13 pc for the molecular cloud along the line of sight. The derived P_{kin} image is shown in the middle and lower panels of Figure 8. P_{kin} is in the range of $\sim 1 \times 10^{-9} - 1.4 \times 10^{-6}$ dyne cm^{-2}. P_{kin} is calculated under the assumption that the length along the line of sight is uniform in G5.89, which is the main bias in the calculation. The estimated total B field strength is 3 mG, thus the B-field pressure (P_{B}) is 3.6×10^{-7} (dyne cm^{-2}). Although the upper limit of P_{kin} is 1.6 times larger than P_{rad} at a radius of $2''$, any variation of the structure in the direction along the line of sight in G5.89 − which is most likely the case − will affect the estimated P_{kin}. Nevertheless, P_{rad} is at the same order as P_{kin} and P_{B} at the radius of $2''$ around the O5 star. Therefore, in terms of pressure, the radiation from the central star is likely sufficient to sweep up the material and compress the B field lines along the narrow dust ridge. λ_{corr} close to 1 near the UC H II region suggests that the B fields play a minor role as compared with the gravity.

The B field direction traced by component "x" is parallel to the major axis of this sharp dust ridge, which is also seen in some other star formation sites such as Cepheus A (Curran & Chrysostomou 2007) and DR 21(OH) (Lai et al. 2003). However, in most of the cases, the detected B field direction is parallel to the minor axis of the dust ridge, e.g., W51 e1/e2 cores (Lai et al. 2001) and G34.4+0.23 MM (Cortes et al. 2008), which

agrees with the ambipolar diffusion model. A possible explanation is that the polarization is from the swept-up material, which interacts with the original dense filament. Thus, the polarization here may represent the swept-up field lines. This scenario is supported by the energy density and also the morphology of the field lines in the case of G5.89.

5.5.6   Comparison with Other Star Formation Sites

The detected B field structure in the G5.89 region is more complicated than the B fields in other massive star formation sites detected so far with interferometers. Both the compressed field structure and the more organized larger scale B field are detected in G5.89.

The B field lines vary smoothly in the cores at earlier star formation stages, such as the W51 e1/e2 cores (Lai et al. 2001), G34.4+0.23 MM (Cortes et al. 2008) and NGC 2024 FIR 5 (Lai et al. 2002). These cores are still in a collapsing stage (Ho et al. 1996 ; Ramesh et al. 1997; Mezger et al. 1992). Among these observations, the B fields inferred from the dust polarization show an organized structure over the scale of 10^5 AU ($15''$) at a distance of 7 kpc in the W51 e1/e2 cores and also on the scale of 10^5 AU ($35''$) at a distance of 3.9 kpc in G34.4+0.23 MM. In contrast, the B fields in NGC 2024 FIR 5, which is closer at a distance of 415 pc, show an hourglass morphology on a scale of 4×10^3 AU ($9''$). Such small-scale structures would not be resolved in the current data of W51 e1/e2 core and G34.4+0.23 MM due to the resolution effect. Compared to these sources, G5.89 is more complicated with polarization structures on both small (4×10^3 AU) and large (2×10^4 AU) scales. However, higher angular resolution polarization images of the cores in the earlier stages are necessary in order to compare the B field morphology with the later stages in the massive star formation process. At this moment, we cannot conclude at which stage the B field structures become more complex.

Currently, the best observational evidence supporting the theoretical accretion model is the polarization observation of the source NGC 1333 IRAS 4A (Girart, Rao & Marrone 2006) carried out with the SMA. The NGC 1333 IRAS 4A is a low-mass star formation site, at a distance of $\sim$300 pc. The detected pinched B-field structure is at a scale of 2400 AU ($8''$). If NGC 1333 IRAS 4A were at a distance of 2kpc, we could barely resolve it at our resolution of $3''$. Higher angular resolution polarization measurements are required to resolve the underlying structure in G5.89.

5.6   Conclusions and Summary

High angular resolution ($3''$) studies at 870μm have been made of the magnetic (B) field structures, the dust continuum structures, and the kinematics of the molecular cloud around the UC H II region G5.89-0.39. The goal is to analyze the role of the B field in the massive star-forming process. Here is the summary of our results.

1. The gas mass (M_{gas}) is estimated from the dust continuum and from the $C^{17}O$ $3-2$ emission line. The continuum emission at 870 μm is detected with its total flux density of 12.6$\pm$1.3 Jy. After removing the free$-$free emission from the detected continuum, the flux density of the 870 μm dust continuum is 7.7 Jy, which corresponds to M_{gas} $\sim$300 $M_\odot$. M_{gas} derived from the detected $C^{17}O$ 3-2 emission line is $\sim$100 $M_\odot$, which is 3 times smaller than the value derived from the dust continuum. The discrepancy of M_{gas} derived from the dust continuum and the $C^{17}O$ emission line is also seen in other UC H II regions, e.g. Hofner et al. (2000). The lower values measured from $C^{17}O$ could be due to optical depth effects or abundance problems.

2. The linearly polarized 870 μm dust continuum emission is detected and resolved. The dust polarization is not uniformly distributed in the entire dust core. Most of the polarized emission is located around the HII ring, and there is no polarization detected in the southern half of the dust core except at the very southern edges. The P.A.s of the polarization vary enormously but smoothly in a region of 2×10^4 AU ($10''$), ranging from $-60°$ to $61°$. Furthermore, the polarized emission is from organized patches, and the distribution of the P.A.s can be separated into two groups. We suggest that the polarization in G5.89 traces two different components. The polarization group "x", with its P.A.s ranging from $-60°$ to $-4°$, is located at the 870μm *sharp dust ridge*. In contrast, the group "o", with its P.A.s ranging from $33°$ to $61°$, is at the periphery of the *sharp dust ridge*. The inferred B field direction from group "x" is parallel to the major axis of the 870μm dust ridge. One possible interpretation of the polarization in the group "x" is that it may represent swept-up B field lines, while the group "o" traces more extended structures. In the G5.89 region, both the large-scale B field (group "o") and the compressed B field (group "x") are detected.

3. By using the Chandrasekhar$-$Fermi method, the estimated strength of $B_\perp$ from component "o" and from component "x" is in between 2 and 3 mG, which is comparable

to the Zeeman splitting measurements of $B_{\parallel}$ from the OH masers, ranging from -2 to 2 mG by Stark et al. (2007). The derived lower limit of $B_{\perp}$ from the detected polarization without grouping and without modeling larger scale B field is $\sim$1mG. Assuming that $B_{\perp}$ and $B_{\parallel}$ have the same strengths of 2 mG in the entire cloud, the derived λ increases from 0.1 to 2.5 toward the UC H II region, which is due to the high contrast of the column density across the cloud. Unless the actual B field strength differs by a factor of 25 across the region and compensates for the contrast in the column density, such a variation of λ in G5.89 is suggested. The corrected mass-to-flux ratio (λ_{corr}) is closer to 1 near the HII region and is much smaller than 1 in the outer parts of the dust core. G5.89 is therefore most likely in a supercritical phase near the H II region.

4. The kinematics of the molecular gas is analyzed using the $C^{17}O$ 3-2 emission line. From the analysis of the channel maps, the PV plots and spectra, the molecular gas in the G5.89 region is expanding along with the HII region, and it is also possibly swept-up by the molecular outflows. Assuming the size along the line of sight is uniform in G5.89, P_{kin} is in the range from $\sim 1 \times 10^{-9}$ to 1.4×10^{-6} dyne cm^{-2}. The calculated radiation pressure (P_{rad}) at a radius of $2''$ and the B field pressure (P_{B}) with a field strength of 3 mG are 8.5×10^{-7} and 3.6×10^{-7} dyne cm^{-2}, respectively. Although the upper limit of P_{kin} is 1.6 times larger than P_{rad} at a radius of $2''$, any variation of the structure in the direction along the line of sight in G5.89 $-$ which is most likely the case $-$ will affect the estimated P_{kin}. Nevertheless, P_{rad} is on the same order as P_{kin} and P_{B} at the radius of $2''$ around the O5 star. The scenario that the matter and B field in the 870μm *sharp dust ridge* have been swept-up is supported in terms of the available pressure.

G5.89 is in a more evolved stage as compared with the corresponding structures of other sources in the collapsing phase. The morphologies of the B field in the earlier stages of the evolution show systematic or smoothly varying structures, e.g. on the scale of 10^5 AU for W51 e1/e2 and G34.4+0.23 MM, and on the scale of 4×10^3 AU for NGC 2024 FIR 5. With the high-resolution and high-sensitivity SMA data, we find that the B field morphology in G5.89 is more complicated, being clearly disturbed by the expansion of the HII region and the molecular outflows. The large-scale B field structure on the scale of 2×10^4 AU in G5.89 can still be traced with dust polarization. From the analysis of the $C^{17}O$ 3-2 kinematics and

the comparison of the available energy density (pressure), we propose that the B fields have been swept up and compressed. Hence, the role of the B field evolves with the formation of the massive star. The ensuing luminosity, pressure, and outflows overwhelm the existing B field structure.

Figure 5.1 *(a)* SMA 870 μm total continuum image (contours) overlaid on the VLA 2 cm continuum (free−free continuum; color scale). The white contours represent the continuum emission strength at 3, 5, 10, 15, 20, 25 ... 60, and 65 σ levels, and the black contours in the center represent 70, 80, 90, 100, and 110 σ levels, where 1σ is 30 mJy Beam^{-1}. The star marks the O star detected by Feldt et al. (2003). The asterisk marks the origin of the Brγ outflow detected by Puga et al. (2006). The SMA and VLA synthesized beams are shown as white and black ellipses at the lower-left corner, respectively. The white "+" mark the positions of the sub-mm peaks identified in Hunter et al. (2008). *(b)* The same as in (a), with the contours representing the SMA 870 μm dust continuum (after the subtraction of the free−free continuum). The contours start from and step in 3σ, where 1σ is 30 mJy Beam^{-1}. The color wedge on the upper-right edge represents the strength of the 2 cm free−free continuum in the units of Jy Beam $^{-1}$. The red and blue arrows indicate the axes of the molecular outflows. The outflows in the N−S and NW−SW direction in the west of O5 star are identified in Hunter et al. (2008). The third outflow in the east of O5 star is identified in Tang et al. (in preparation). *(c)* The polarization (red segments) derived by using image (a). The length of the red segment represents the percentage of the polarized intensity. The 870 μm continuum is shown both in white contours with the steps as in Fig. (a) and in the color scale. *(d)* The polarization (red segments) derived by using image (b). The 870 μm dust continuum is again shown both in white contours with the steps as in Fig. (b) and in the color scale. The color wedge at the lower-right edge shows the strength of the dust continuum in the units of Jy Beam^{-1}. In *(c)* and *(d)*, the polarization plotted is above $3\sigma_{I_p}$.
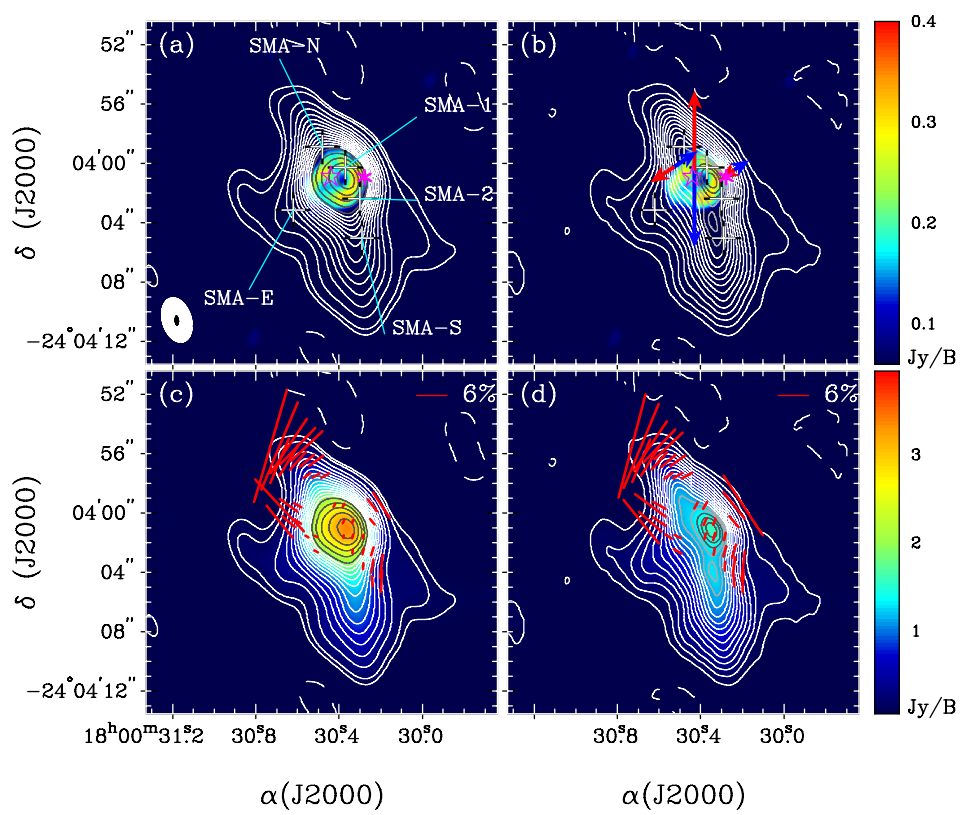
Figure 5.1 –continue

Figure 5.2 (a) 870μm dust continuum (contours) overlaid on the polarized intensity (I_P) image (color scale). The contours plotted are the same as in Figure 1(b). The color wedge shows the strength of polarization intensity in units of mJy Beam^{-1}. The smallest white open circles and plus signs mark the positions of the Zeeman pairs of the OH maser (Stark et al. 2007) with different polarimetries. The other symbols are the same as in Figure 1. The larger solid white circles mark component "o", defined in Sec. 4.2.2. (b) The polarization (red and blue segments) overlaid on the 870 μm dust continuum (black contours) and the 2 cm free−free continuum emission (color scale). Red and blue are polarization segments above $3\sigma_{I_p}$ and between 2 and $3\sigma_{I_p}$, respectively. The contours, star, asterisk, circles, and plus signs are all the same as in (a). The color wedge shows the strength of the 2cm free−free emission in units of Jy Beam^{-1}. The ellipses in the lower-left corner are the synthesized beams of this paper, shown in black, and of the 2cm free-free continuum image, shown in white. (c) The inferred B field (red segments) overlaid on the 870 μm dust continuum (blue contours) in this paper and in Hunter et al. (2008) (gray scale). The ellipses in the lower-left corner are the synthesized beams of this work, shown in black, and of Hunter et al. (2008), shown in white. The white crosses mark the sub-mm sources detected by Hunter et al. (2008). The triangles mark the positions of the H_2 knots identified in Puga et al. (2006).
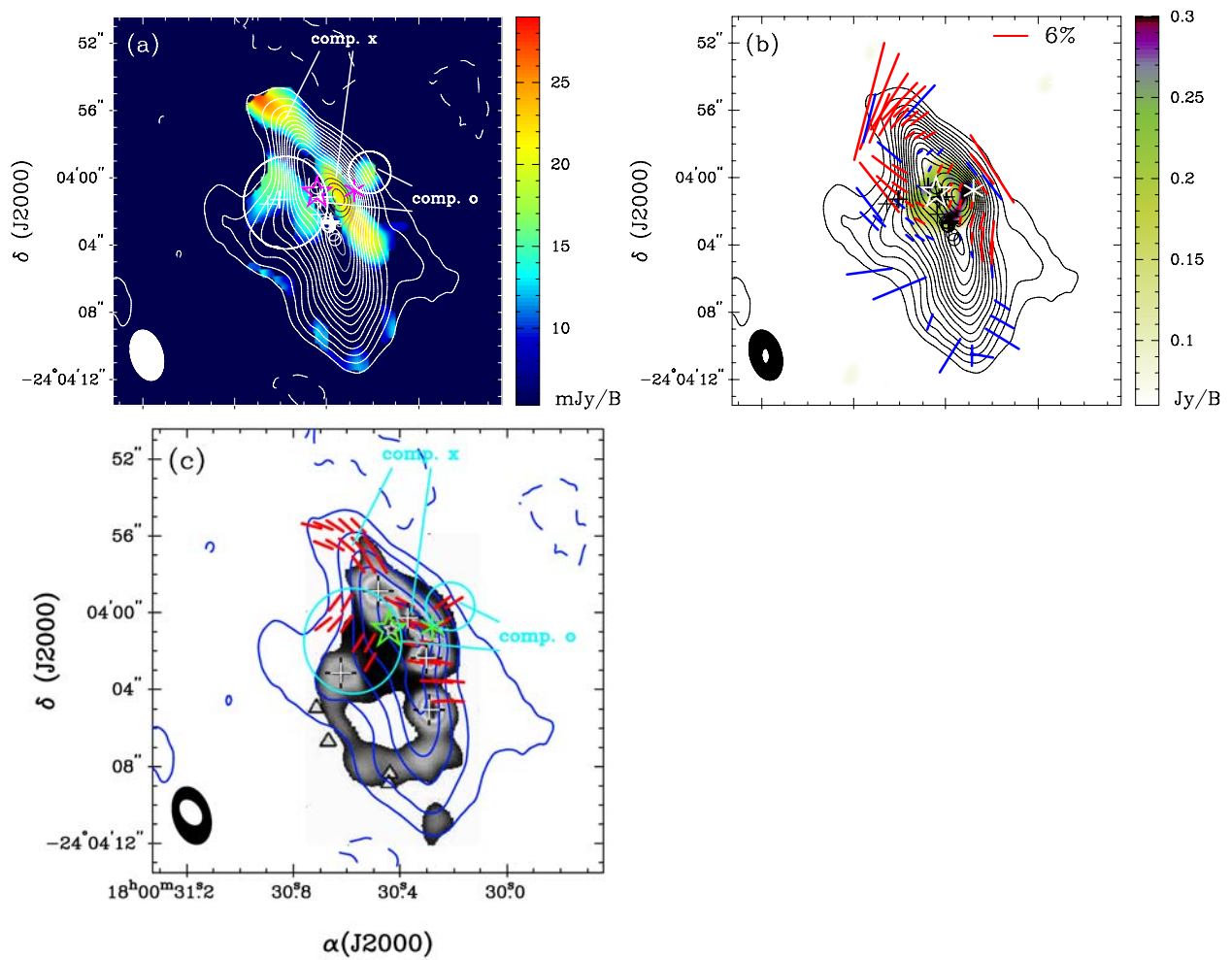
Figure 5.2 –continue

(a)

(b)
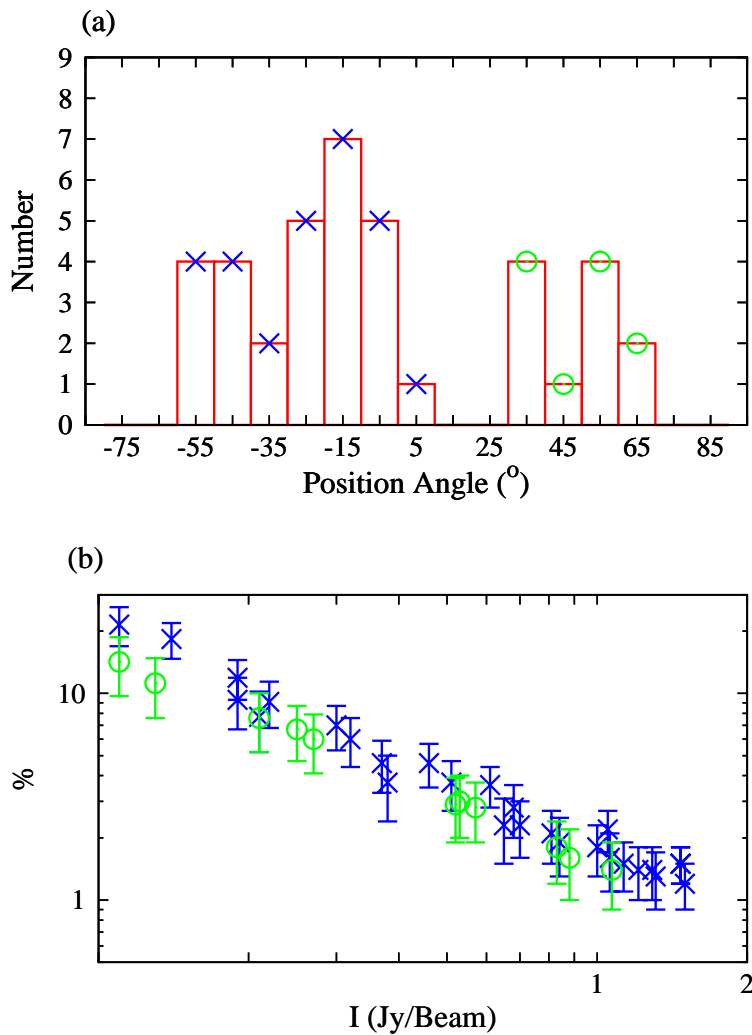
Figure 5.3 (a) Distribution of the P.A.s (defined in the range from $-90°$ to $90°$) of the polarization in G5.89. (b) Total intensity (I) vs. percentage (%) of the polarized flux density. In both (a) and (b) panels, the statistics are from the detected polarization segments above the $3\,\sigma_{I_p}$ confidence level. The "cross" represents the component "x", which is associated with the sharp dust ridge. The "circle" represents the component "o", which is associated with the extended structure.

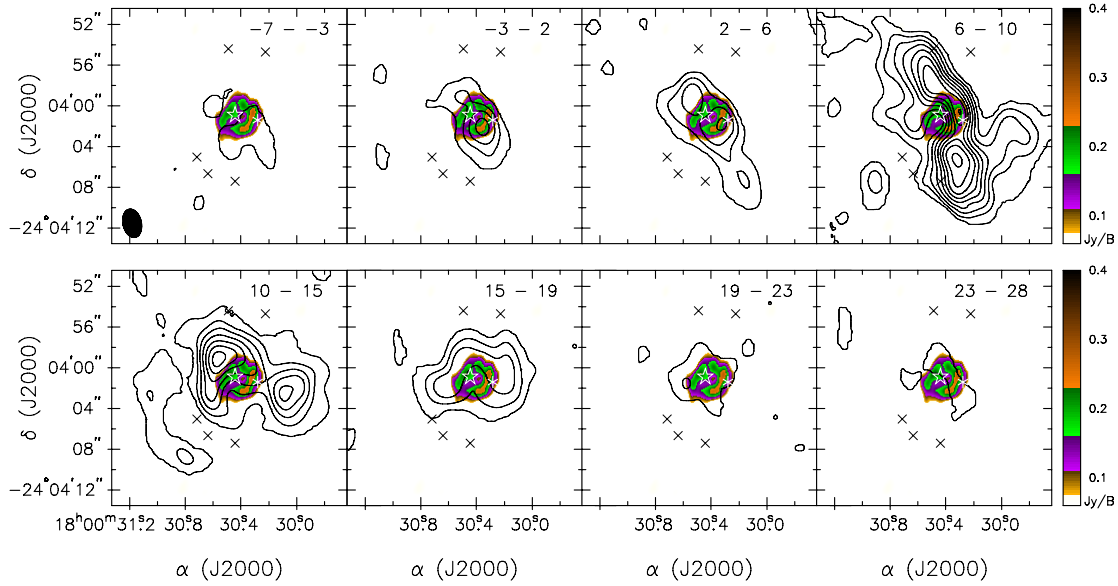Figure 5.4 C^{17}O 3-2 line emission (black contours) integrated in eight different velocity ranges, as indicated in each panel in units of km s^{-1}. The color scale images represent the VLA 2 cm free−free continuum emission with its strength shown in the wedge in units of Jy Beam^{-1}. To show the fainter component in the higher velocity panels, the black contours represent the strengths at 2, 6, 10, 15, 21, 27, 33, 40, and 48 σ, where 1 σ is 0.4 Jy Beam^{-1} km s^{-1}. The black crosses mark the positions of the H$_2$ knots detected by Puga et al. (2006). The other symbols are the same as in Figure 1. In the panels from −7 to −3 and 23 to 28 km s^{-1}, the C^{17}O dense cloud has an extension similar to the dust ridge detected in the 0$''$.8 dust continuum image (Figure 2). The peak positions of the high-velocity components do not coincide with the location of the O5 star.

Figure 5.5 Upper Panel: the total integrated intensity (zeroth moment) image of the C^{17}O 3-2 emission line (black contours) overlaid on the dust continuum at 870 μm (color scale). The contours represent the emission strength starting from and stepping in 3 Jy Beam^{-1} km s^{-1}. The letters mark the positions where the spectra were taken in Figure 7. The black cross marks the peak emission at position A. The color wedge shows the strength of the 870 μm dust continuum in units of Jy Beam^{-1}. The black contours start from and step in 3 σ, where 1σ is 1 Jy Beam^{-1} km s^{-1}. Middle Panel: the intensity weighted velocity image (first moment) of the C^{17}O 3-2 emission line. The contours start from and step in 1 km s^{-1}. The wedge is in units of km s^{-1}. Lower Panel: the intensity weighted velocity dispersion (δv_{total}) image (second moment) of the C^{17}O 3-2 emission line. The contours start from and step in 1 km s^{-1}. The wedge is in units of km s^{-1}. The white segments mark the cut of the PV diagram shown in Figure 6(j). The rest of the symbols are the same as in Figure 1.
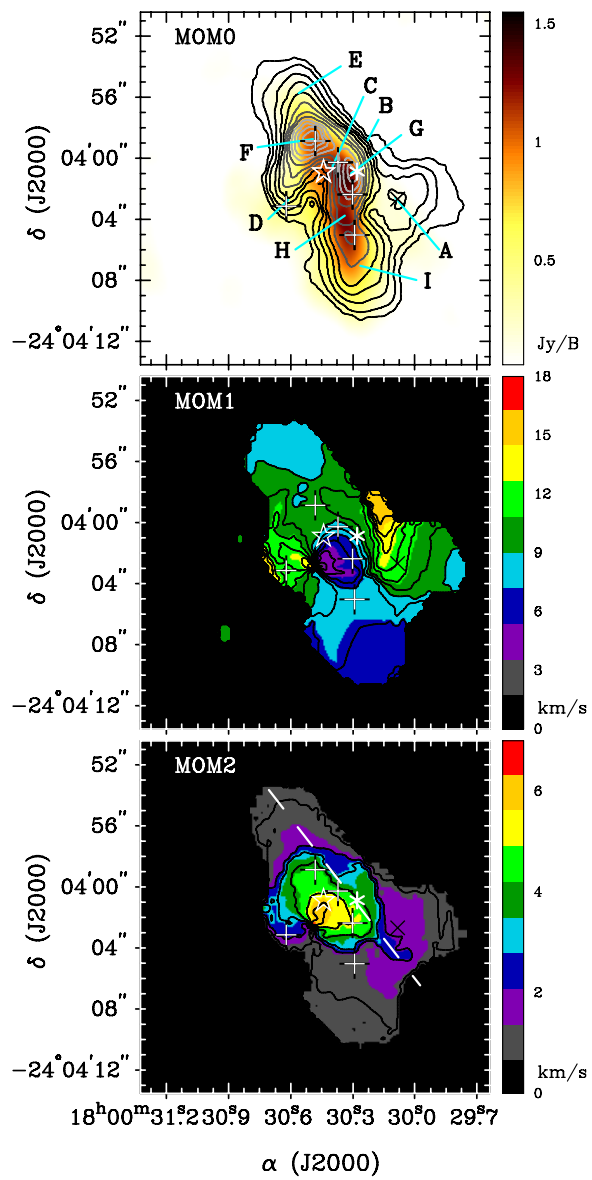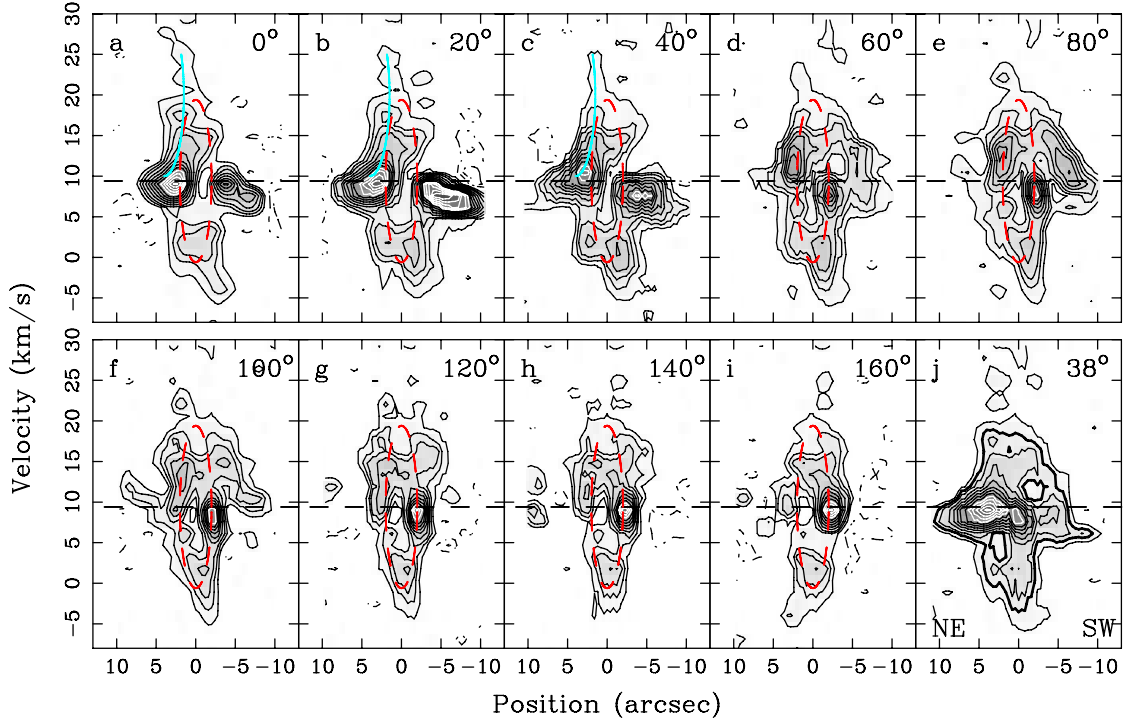
Figure 5.5 –continue

Figure 5.6 PV diagram cuts at the position of the O5 star (panel *a* to *i*) at nine different P.A.s, as indicated at the upper-right corner in each panel. Panel *j* is the PV diagram along the white segments indicated in the lower panel of Figure 5. To show the fainter emission at outer regions, the black contours are plotted in 2, 4, 6, 9, 12, 15, 18 and 21 × σ and white contours in 24, 27, 30, 33, 36 × σ, where 1σ =0.16 Jy Beam^{-1}. The thick contour in panel *j* represents the emission strength of 4σ. The dashed segments indicate the v_{sys} of 9.4 km s^{-1}. The red dashed ellipse marks the ring-like structure with a radius of 2″ and 10 km s^{-1} and centered at the position of the O5 star and v_{sys} of 9.4 km s^{-1}. The majority of the gas is quiescent with a velocity close to v_{sys}. In panel *j*, a loop-like structure is seen at positions of ± 2″. A clump at a v_{lsr} of 0 km s^{-1} is detected in all the PV cuts at different P.A.s (panel *a* to *i*). At the P.A. of 0°−40°, the high-velocity structure extending from the position of 2″.5 is clearly seen, as indicated by the blue arc.
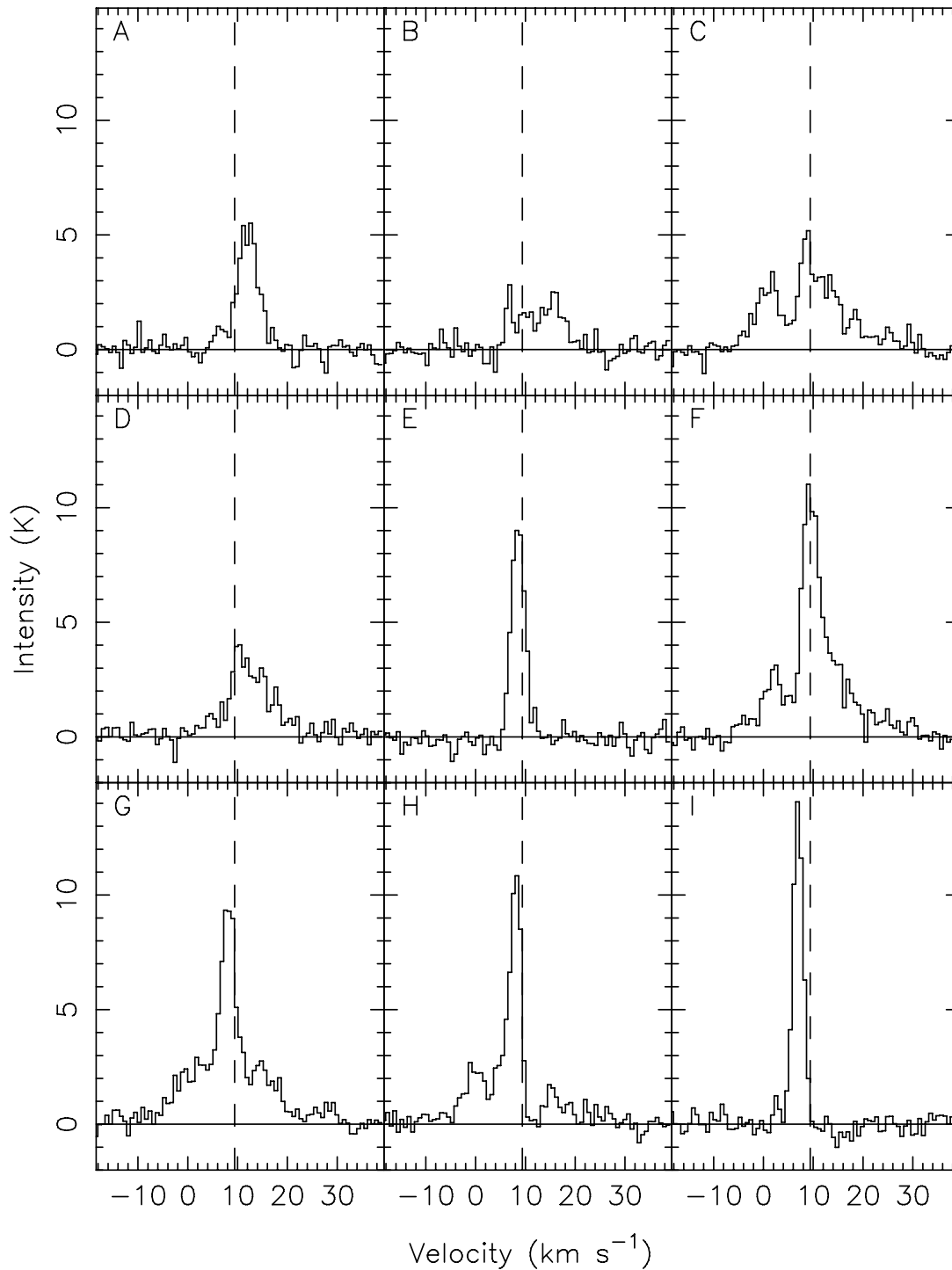
Figure 5.7 Spectra of the $C^{17}O$ 3-2 line at various positions as indicated in Figure 5. The solid and dashed segments mark the intensity of 0 K and $v_{\rm sys}$ of 9.4 km s^{-1}, respectively. Note that the typical HII region expands at a velocity of $\pm$ 10 km s^{-1}. At position E and I, the spectra are narrowest.

Figure 5.8 Upper panel: an image of the mass-to-flux ratio λ in both contours and color scale. λ is derived using the $C^{17}O$ 3-2 emission line assuming a uniform total B field strength of 3 mG, which corresponds to a B field pressure (P_B) of 3.6×10^{-7} dyne cm^{-2}. The thick black contour marks $\lambda=1$. The thin black contours mark $\lambda=0.1$, 0.5, 1.5, 2, 2.5. The strength of λ in color scale is indicated in the wedge. The other symbols are the same as in Figure 2. Middle panel: an image of the derived kinetic pressure (P_{kin}) in log scale in both black contours and color scale. The thick black contour marks $logP_{kin} = -6.45$, which is equal to $P_B=3.6 \times 10^{-7}$ dyne cm^{-2}. The thin black contours mark $logP_{kin} = -6, -7, -8$, and -9. The white contours represent the 2 cm free$-$free emission starting from and stepping in 72 mJy $Beam^{-1}$. The wedge is in the units of log dyne cm^{-2}. Lower panel: an image of P_{kin} in a linear scale in both black contours and color scale. P_{kin} is in the unit of dyne cm^{-2}. The thick black contour marks $P_{kin} = 3.6 \times 10^{-7}$ dyne cm^{-2}. The thin black contours mark $P_{kin} = (0.3, 3, 60, 90, 120) \times 10^{-8}$. The red segments represent the 870 μm polarization above $3\sigma_{I_p}$, detected in this paper.

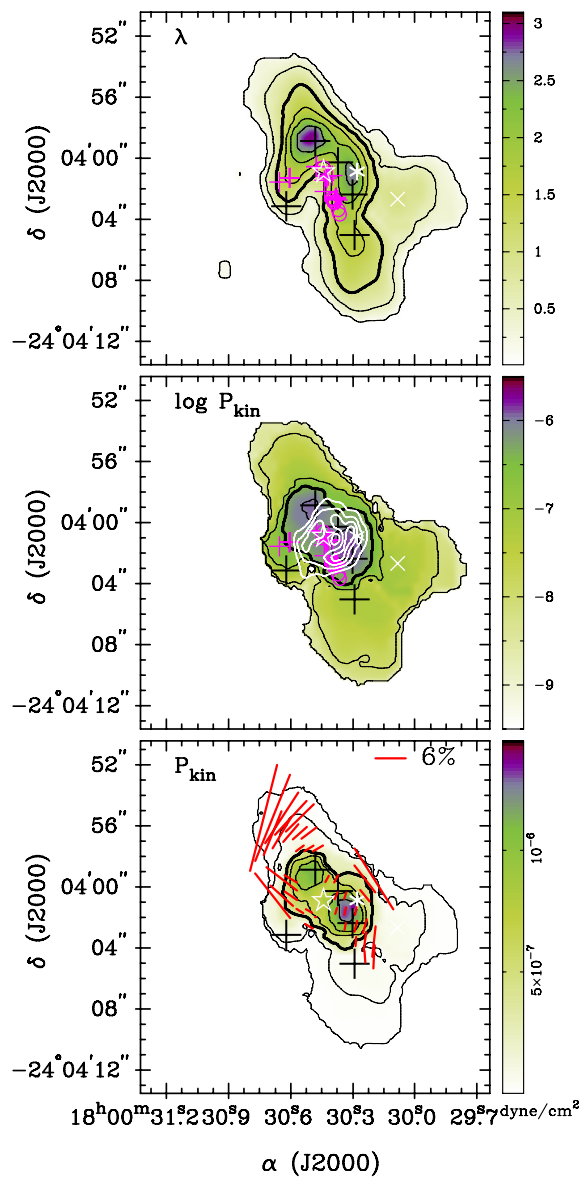Figure 5.8 –continue

Table 5.1.   SMA dust polarization at 870 μm in G5.89-0.39

$\triangle$x	$\triangle$y	I$_p$	%	PA	δv_{total}	group
5.4	5	24	21.5 ± 4.6	-14 ± 6	1.0	x
4.8	5	26	18.3 ± 3.6	-22 ± 5	1.2	x
4.2	5	23	11.9 ± 2.6	-33 ± 6	1.2	x
3.6	5	20	9.1 ± 2.3	-43 ± 7	1.2	x
3	5	16	7.7 ± 2.5	-46 ± 9	1.2	x
4.8	4	18	9.3 ± 2.6	-22 ± 8	1.0	x
4.2	4	21	7 ± 1.7	-31 ± 7	1.5	x
3.6	4	21	4.6 ± 1.1	-41 ± 7	1.5	x
3	4	19	3.7 ± 1	-49 ± 8	1.5	x
2.4	4	14	3.7 ± 1.3	-53 ± 10	1.4	x
3	3	16	1.9 ± 0.6	-54 ± 9	2.5	x
2.4	3	17	2.1 ± 0.6	-59 ± 8	2.2	x
1.8	3	15	2.3 ± 0.8	-60 ± 10	2.0	x
4.2	1	16	7.6 ± 2.4	53 ± 9	3.4	o
3.6	1	16	2.8 ± 0.9	60 ± 9	4.3	o
1.2	1	17	1.4 ± 0.4	-29 ± 8	4.0	x
0.6	1	17	1.6 ± 0.5	-29 ± 8	3.3	x
-1.2	1	17	6.7 ± 2	38 ± 9	3.8	o
-1.8	1	16	14.2 ± 4.5	33 ± 9	1.8	o
4.8	0	15	11.2 ± 3.6	38 ± 9	2.7	o
4.2	0	16	6 ± 1.9	48 ± 9	3.6	o
3.6	0	16	3 ± 1	56 ± 9	4.0	o
0.6	0	22	1.5 ± 0.3	-24 ± 7	4.6	x
0	0	17	1.3 ± 0.4	-18 ± 9	4.5	x
-1.2	0	15	2.9 ± 1	39 ± 10	3.9	o
3	-1	14	1.6 ± 0.6	58 ± 10	4.5	o

Table 5.1 (continued)

$\triangle$x	$\triangle$y	I_p	%	PA	δv_{total}	group
2.4	-1	15	1.4 ± 0.5	61 ± 9	5.8	o
0.6	-1	18	1.2 ± 0.3	-16 ± 8	5.3	x
0	-1	22	1.5 ± 0.3	-15 ± 6	5.0	x
-0.6	-1	17	1.5 ± 0.4	-12 ± 8	4.8	x
2.4	-2	15	1.8 ± 0.6	59 ± 9	5.9	o
0	-2	18	1.4 ± 0.4	-10 ± 8	5.0	x
-0.6	-2	23	2.2 ± 0.5	-14 ± 6	4.8	x
-1.2	-2	19	2.8 ± 0.8	-16 ± 8	4.7	x
-0.6	-3	18	1.8 ± 0.5	-4 ± 8	3.3	x
-1.2	-3	22	3.6 ± 0.8	-8 ± 6	2.4	x
-1.8	-3	19	6 ± 1.6	-6 ± 8	2.7	x
-1.2	-4	16	2.3 ± 0.7	4 ± 9	1.4	x
-1.8	-4	17	4.6 ± 1.3	-3 ± 8	1.4	x

Note. — $\triangle$x & $\triangle$y: offsets in arcsecond from the coordinate (J2000): $\alpha = 18^h00^m30.32^s$, $\delta = -24^{\circ}04'00''.48$. I_p: the polarized intensity in mJy Beam^{-1}. %: polarization percentage, defined as the ratio of I_p/I. PA: position angle from the north to the east in degree. δv_{total}: total dispersion velocity (2nd moment) measured in the C^{17}O 3-2 emission line in km s^{-1}. All data listed are above $3\sigma_{I_p}$.

Chapter 6

B field geometry in relatively quiescent core MMS 6 in OMC 2/3

Tang, Ya-Wen, Ho, Paul T. P. et al.

ApJ, in prep.

Abstract

The OMC2/3 dust ridge has an integral-shape at 0.5 pc scale, and the B field direction has been shown to be perpendicular to the elongation of the dust ridge. With $0\rlap{.}''7$ angular resolution, our revealed polarized emission exhibits a clear deviation of field direction in the compact core MMS 6 in the scale of 7 mpc. Shorter baseline data will be helpful to link the field of the core to the extended and fainter part of the dust ridge.

6.1   Introduction

To complete the evolutionary trend of the magnetic field in the massive star forming regions, we observe a relative quiescent core MMS 6 in OMC 3.

MMS 6 is the strongest millimeter continuum source in the OMC-3 cloud (Chini et al. 1997). Located at a distance of 450 pc, it is one of the closest massive star forming regions, with a total bolometric luminosity < 60 $L_\odot$, and a total mass of gas and dust of 34 $M_\odot$. Previous 2mm NMA observations revealed that the core splits into a bright source, MMS

6-main, surrounded by at least 7 faint dust condensations (a-g in Fig. 1(a)). However, there is no heating source and outflow signature detected in MMS 6-main (Takahashi et al. 2009; Matthews et al. 2005). The size, mass and the average density of MMS 6-main are estimated to be 900 AU, 2.8 $M_\odot$, and 10^7 cm^{-3}, respectively. Its density is one order of magnitude larger than the low mass star forming cloud L723 (3 $L_\odot$), where the density is 10^6 cm^{-3} as estimated from the previous SMA observation. There is no 24μm counterpart toward MMS 6-main, which implies that it is a cold and massive starless core. The free-free continuum detected (Reipurth et al. 1999) toward MIR-N (Fig. 1(a)) suggests that there is a shock region resulting from a jet in this location. MMS 6 is probably a mixture of intermediate/massive starless and star forming cores.

A dust polarization observation carried out with BIMA has shown relatively uniform polarization vectors with the synthesized beam of 4.3"×3.0" (Matthews et al. 2005). In the BIMA observation, one to two independent vectors are detected. Higher angular resolution observations are needed to resolve the B field associated with the core structure.

6.2   Observations and Data Reduction

The observations were carried out on 2007 Nov. 15, Dec. 15 in compact array, and on 2008 Feb. 15 in extended array using the SMA (Ho, Moran, & Lo 2004)[1]. Here, we present the results based on the extended array data. The calibration and data reduction procedures were done simultaneously with Orion BN/KL (Chapter 4). The projected lengths of baselines ranged from 30 to 262 kλ. The largest size scale which could be sampled in this observation was 8″. The local oscillator frequency was tuned to 341.482 GHz. With the 2 GHz bandwidth in each sideband, we were able to cover the frequency ranging from 345.5 to 347.5 GHz and from 335.5 to 337.5 GHz in the upper and lower sidebands, respectively. The primary beam (field of view) of the SMA at 345 GHz is ∼30″.

The rms of stokes I map is 10 mJy, and of the polarized intensity (I_p) is 4 mJy with natural weighting.

---

[1]The Submillimeter Array is a joint project between the Smithsonian Astrophysical Observatory and the Academia Sinica Institute of Astronomy and Astrophysics and is funded by the Smithsonian Institution and the Academia Sinica.

6.3   Results

The 870 μm dust continuum emission is detected with an angular resolution of $0''\!.8\times0''\!.7$ (Figure 1). The deconvolved size of a Gaussian toward the peak position is the same as the synthesized beam. Therefore, the dust continuum is not resolved. There is only one continuum peak detected with a slight elongation from north-east to south-west. The continuum strength is 2.6 Jy. Note that the peak intensity is 1.3 Jy beam^{-1} in MMS 6.

6.3.1   Polarization

The linearly polarized emission is weak. The detected polarized intensity is 18 mJy, and the polarized percentage is 2%, consistent with the detected P(%) toward the peak position with 14$''$ angular resolution (Matthews et al. 2001).

The position angles, defined as from the north to the east, of the detected polarization at 870 μm range from -10° to -100° across the dust core. As comparing to previous observational results at 1.3 mm with 3$''$ resolution (Figure 2), there is a clear deviation between the 1.3 mm and the reported 870 μm results.

6.4   Discussion

With the SMA, the low mass cores VLA 1623, L1551 IRS1 and HL TAU are also seen to be point-like, and the P(%) at the peak position is $\leq$1%. These cores are known to harbor star formation activities. MMS 6 is in an earlier stage, because there are no known star formation activities detected.

Is the field geometry more complex, or the magnetic flux has been re-distribute so that the material can transfer inward in these strong but compact cores? The observational results with combined compact and extended array data in MMS 6 will be helpful to reveal the field morphology in the fainter region.
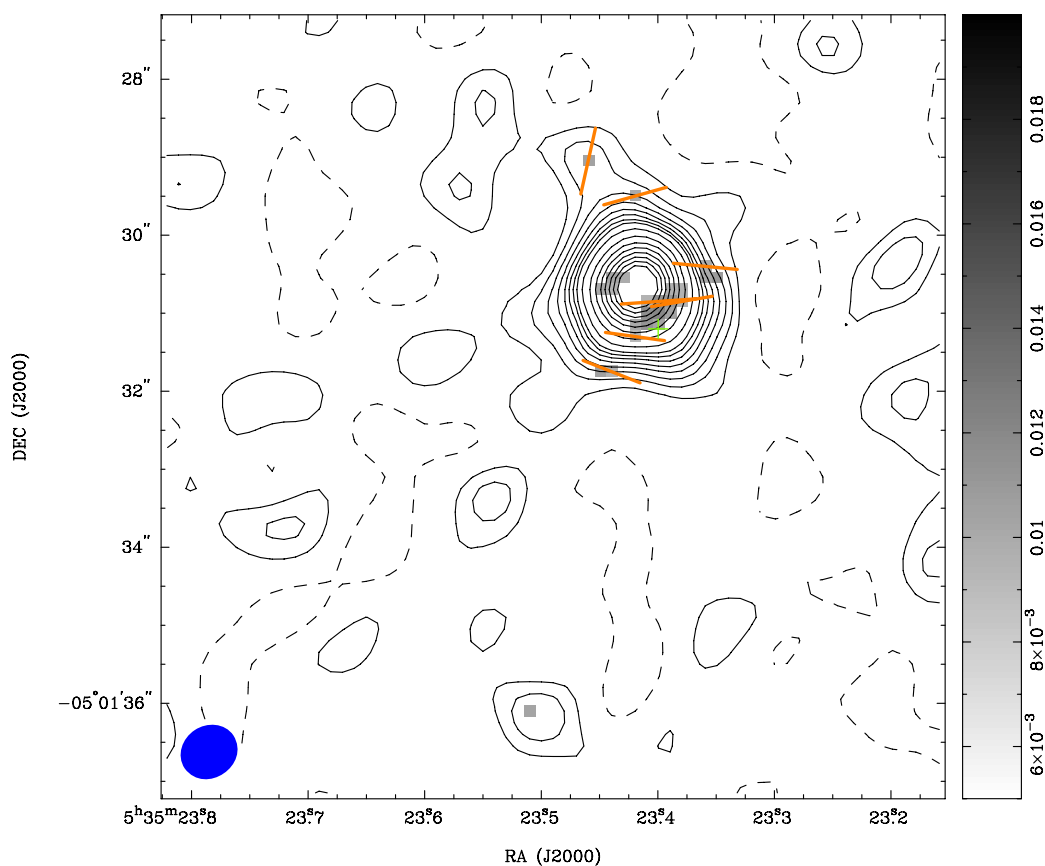
Figure 6.1 SMA dust continuum at 870 μm and its linear polarized emission in MMS 6. The segments here indicate the polarized direction. This is the result of the extended array. Contours start from and step in 3σ (0.03 Jy beam^{-1}). The plotted vectors are above 2.5 $\sigma_{\mathrm{I_P}}$.
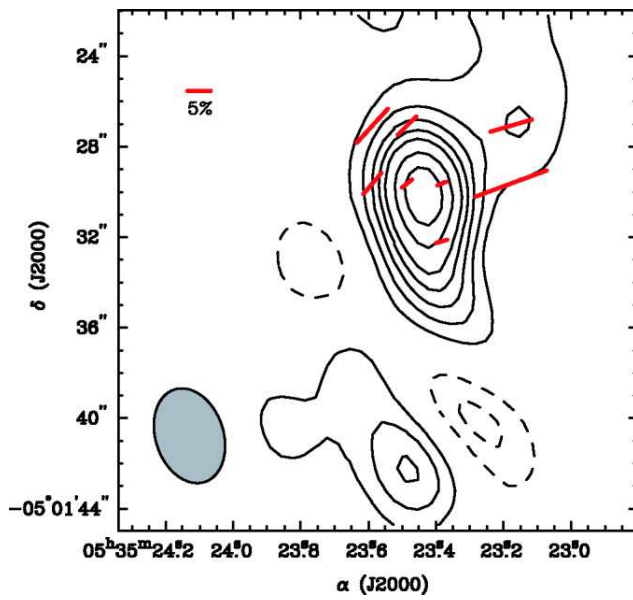
Figure 6.2 BIMA dust continuum at 1.3 mm and its linear polarized emission in MMS 6, adopted from Matthews et al. (2005). The segments here indicate the polarized direction.

Chapter 7

Conclusion and Future Direction

The morphologies of magnetic field in the plane of sky ($B_\perp$) in five massive star forming regions have been imaged from the linear polarization of dust continuum. By comparing the $B_\perp$ of the selected sources at various evolutionary stages, the roles of the B fields are observed to vary in different evolutionary stages. In the earliest stage observed, i.e. collapsing cores, the B field dominates and controls the dynamical evolution of the envelope and cores as revealed in the W51 e2/e8 region. In the collapsing core where several star forming regions are evolving, the B field is preserved in most of the condensations, while there are variations detected between each condensations in W51 North:dust. In a more evolved stage, i.e. the radiation and molecular outflows have significantly influenced the surrounding molecular cloud, the B field is evidently overwhelmed by these stellar feedbacks as in G5.89-0.39. Because the massive star forming regions are typically further away at distances of a few kpc, observations with higher spatial resolution are important to reveal the smaller physical scale $B_\perp$ field. The $B_\perp$ field in the closest massive star forming region, Orion BN/KL, has been resolved at 2 milli-pc (480 AU) resolution. The revealed B field in Orion BN/KL has smooth change in position angle by 90° within 3000 AU near IRc2. One possible interpretation is that the detected dust continuum and B field trace the remnant disk structure centered near source I and therefore, both the poloidal and toroidal B field are revealed. However, the possibility that the dust grains are mechanically aligned can not be ruled out. Finally, in stages when the star forming activities are not obvious and UCH II regions are not formed yet, the role of B field is not clear, because the polarization seems to be low, as seen in MMS 6.

In summary, the star formation process seems to be hierarchical and evolves through different stages. In larger scales, B field dominates the molecular cloud (sub-critical). Within the sub-critical region, there are denser cores formed. The stellar feedbacks in massive star forming regions are energetic and will overwhelm the surrounding molecular clouds. Depends on which epoch we observe, the role of the B field may change. In comparison with previous $B_\perp$ maps observed with slightly poorer resolution at wavelengths of 3 mm and 1.3 mm, the $B_\perp$ detected in this thesis apparently revealing more complex structure, suggesting that the B field plays a less important role in smaller physical scales.

Depolarization often seen in denser regions is most likely due to more complex B field geometry underlying, as seen in W51 e2/e8 regions and the abrupt change in position angle along the dust ridges in W51 North:dust and G5.89-0.39.

7.1   Summary of Individual Source

1. In the more evolved region, the UCHII region G5.89-0.39, the morphology of the detected polarization is complex but vary smoothly in position angles. By analyzing $C^{17}O$ 3-2 line, we found that the surrounding molecular cloud has been disturbed by the stellar feedbacks, such as expansion of UCHII region and molecular outflows. By comparing the pressure terms available, we conclud that the B field has been overwhelmed by the stellar feedback and thus play a more passive role (Chapter 5).

2. In the collapsing core, W51 e2/e8, the revealed B field geometry appears to be pinched with rather sharp opening angle. By testing the null hypothesis of a radial field, it seems that a pure radial field can not describe the system well. Furthermore, the pinched plane is parallel to the plane of ionized accretion flow. Therefore, we suggest that the massive star forming cores are formed through similar process, i.e. accretion, as in the low mass cases. Since the e2 and possible e8 are know to be in collapsing phase, they are super-critical cores, where gravity dominates over B field. In contrast, the envelope surrounding these cores are in subcritical phase. We conclude that these cores are formed through magnetic fragmentation, where magnetic field controls the dynamical evolution of the envelope and cores in W51 e2/e8 (Chapter 2).

3. In another collapsing core observed with similar resolution as in W51 e2/e8, the revealed B field in W51 North is different. The dust ridge appears to be more extended

and 6 clumps have been resolved. The B fields in most clumps have similar position angle. The two interesting features seen are: A twisted B field geometry is detected near the continuum peak. A fan-like B field geometry detected with extension of $2''$. Since there are several star forming regions have been identified within the dust ridge, some are protostars, some already has weak free-free emission, we speculate that the difference in the observed B field geometries between clumps is due to evolution status (Chapter 3).

4. In the closest massive star forming site, Orion BN/KL, the polarization is resolved with 2 milli-pc (480 AU) resolution. The revealed B field in Orion BN/KL changes smoothly in position angle by $90°$ within 3000 AU near IRc2. The dust continuum is detected in the hot core region, in the north of compact ridge and in the south of BN. The well-known source I, infrared source n and BN are all off from the continuum peak. Besides, there are 0.14 pc CO outflows originated from the same position of the proposed common center before the ejection of BN, I sources, and there CO filaments are more obviously seen in the northern part. One possible interpretation is that the detected dust continuum and B field trace the remnant disk structure centered near source I and therefore, both the poloidal and toroidal B field are revealed. In this scenario, most part of the disk has been dispersed by the close encounter when source BN and I were ejected, which also triggered the 0.14 pc scale CO outflows. The revealed remnant is the densest part of the disk. However, the possibility that the dust grains are mechanically aligned can not be ruled out (Chapter 4).

5. In the earliest evolutionary stage where no obvious star formation activities are found, MMS 6 in OMC 2/3 region, the polarized intensity and percentage is low. Either the B field morphology is uniform or a more complex field geometry is possible (Chapter 6).

7.1.1   On-going projects

Orion BN/KL

This source has been observed with BIMA at 1.3 mm and 3 mm. The ratio of the polarized percentage at different locations can be used to test the properties of the dust

grains (Hildebrand et al 1999). The mosaic of the field along the entire ridge will be helpful to link the B field seen in BN/KL core to the OMC-1 cloud.

To test the proposed remnant of disk, the kinematics information is needed. However, depends on which molecules chosen, the appearance and derived temperature can be very different. A proper tracer for dense cloud is needed. The observational results utilizing the absorption of background stellar light at infrared can provide the B field geometry in the regions with smaller column density. It will be helpful to combine all the existing polarization data observed at different wavelengths.

W51 e2/e8 and W51 North: dust

The presented polarizations in W51 e2/e8 and North:dust are from the extended array data, and therefore, they are sensitive to the compact structures. By adding both the shorter and longer baseline visibilities, we expect to linking to the field from the cores to the envelope, and resolve the depolarization zones. We have awarded very extended and compact/subcompact array tracks of the SMA in 2009 A semester.

The kinematics associated with the collapsing cores can be derived from hot core lines. With SiO 8-7, the molecular outflows closer to the driving source can be traced. With the detected lines, the rotation axis of the hot core and outflows can be better determined. This information is crucial to test if the angular momentum is preserved in the cores. With more complete data, we are able to see if there is clear trend of turbulence as a function of structure.

7.2 Future Direction

7.2.1 More polarization measurements toward earlier sources

The selected sources are already in the stage where the UCHII region are formed. Observation toward high-mass proto-stars, such as G30.79 FIR 10 and G28.34+0.06, will be helpful to complete the evolutionary sequence. Besides, the morphology of $B_\perp$ is projected in the plane of sky and therefore, it highly depends on the relative inclination angle of the field geometry and the line of sight. More observations with sufficient angular resolution toward difference sources are important.

7.2.2   Linking to larger scale B field

The presented synthesized polarization images in this thesis are powerful to trace the B fields in compact structures. To interpret these B field geometries, larger scale B field information is important to analyze the role of the B field in the star formation process. The sub-compact array of the SMA is powerful.

7.2.3   Kinematics of the cores

The polarization tracks are usually carried out at good weather conditions. Besides dust polarization, there are molecular lines detected. The kinematics associated with these cores can get derived utilizing these lines. The rotation, outflow direction and linewidths at different positions are important when we want to compare the angular momentum, energy budget or turbulence in the system. The comparison of the angular momentum in the cores with the envelope may provide a test if turbulence or magnetic field is dominant in the star formation process.

7.2.4   Simulate $B_\perp$ of disks/flattened structures

The $B_\perp$ morphologies are highly dependent on the field geometries with respect to the line of sight and the kinematics of the disks or flattened structures. For example, the system if collapsing and field lines are anchored to the ionized particles, hourglass-like B field morphologies are expected. If the system is rotating, the B field will be dragged along the rotation and therefore, twisted. Toy models or simulations considering the observed kinematics in the system will be helpful to interpret the observed polarization in a more quantitative way.

7.2.5   Higher sensitivity observations

The polarized percentage is typically 1 to 10% in massive star forming regions. We can only detected the B field morphology if the source is strong enough, typically a few Jy within a few arcseconds. Observations with higher sensitivity are required to trace the field geometry in fainter regions. AlMA will be very power to reach both high sensitivities and high angular resolutions.

Bibliography

1 Acord, J. M., Churchwell, E., & Wood, D. O. S. 1998, ApJ, 495, 107

2 Aitken, D. K., Efstathiou, A., McCall, A., & Hough, J. H. 2002, MNRAS, 329, 647

3 Aitken, D. K., Smith, C. H., Moore, T. J. T., Roche, P. F., Fujiyoshi, T., & Wright, C. M. 1997, MNRAS, 286, 85

4 Beuther, H. et al. 2004, ApJ, 616, L31

5 Beuther, H., Zhang, Q., Greenhill, L. J., Reid, M. J., Wilner, D., Keto, E., Shinnaga, H., Ho, P. T. P., & Moran, J. M. 2005, ApJ, 632, 355

6 Beuther, H. et al. 2006, ApJ, 636, 323

7 Beuther, H., & Nissen, H. D. 2008, ApJ, 679, L121

8 Bonnor, W. B. 1956, MNRAS, 116, 351

9 Cesaroni, R., Walmsley, C. M., Koempe, C., & Churchwell, E. 1991, A&A, 252, 278

10 Chandler, C. J. 2005, in ASP conf. Proc., 340, Future Directions in High Resolution Astronomy: The 10th Anniversary of the VLBA, ed. J. Romney & M. Reid. (San Francisco: Astronomical Society of the Pacific), 317

11 Chandrasekhar, S., & Fermi, E. 1953, ApJ, 118, 113

12 Chini, R., Ward-Thompson, D. et al. 1997, ApJ, 474, L135

13 Choi, M., Evans II, N., & Jaffe, D. T. 1993, ApJ, 417, 624

14 Chrysostomou, A., Aitken, D. K., Jenness, T., Davis, C. J., Hough, J. H., Curran, R., & Tamura, M. 2002, 385, 1014

15 Chrysostomou, A., Hough, J. H., Burton, M. G., & Tamura, M. 1994, MNRAS, 268, 325

16 Churchwell 1997, ApJ, 479, L59

17 Cohen, R. J., Gasiprong, N., Meaburn, J., & Graham, M. F. 2006, MNRAS, 367, 541

18 Cortes, P., & Crutcher, R. M. 2006, ApJ, 639, 965

19 Cortes, P. C., Crutcher, R. M., & Watson, W. D. 2005, 628, 780

20 Cortes, P., Crutcher, R. M., & Matthews, B. 2006, ApJ, 650, 246

21 Cortes, P., Crutcher, R. M., Shepherd, D. S., & Bronfman, L. 2008, ApJ, 676, 464

22 Crutcher, R. M. 2004, ApSS, 292, 225

23 Crutcher, R. M., Nutter, D., Ward-Thompson, D., & Kirk, J. M. 2004, ApJ, 600, 279

24 Curran, R. L. & Chrysostomou, A. 2007, MNRAS, 382, 699

25 Davis, L. Jr., & Greenstein J. L. 1951, ApJ, 114, 206

26 De Buizer, J. M., Radomski, J. T., Telesco, C. M., & Pina,R. K. 2005, ApJS, 156, 179

27 Deguchi, S. & Watson, W. 1984, ApJ, 285, 126

28 Dotson, J. 1996, ApJ, 470, 566

29 Dotson, J. L., Davidson, J., Dowell, C. D., Schleuning, D. A., & Hildegrand, R. H. 2000, ApJSS, 128, 335

30 Draine, B. T., & Weingartner, J. C. 1996, ApJ, 470, 551

31 Ebert, R. 1955, Zs. Ap., 37, 217

32 Ebert, R. 1957, Zs. Ap., 42, 263

33 Elmegreen, B. G., & Scalo, J. 2004, ARA&A, 42, 211

34 Emerson, J. P., Jennings, R. E., & Moorwood, A. F. M. 1973, ApJ, 184, 401

35 Eisner, J. A., Greenhill, L. J., Herrnstein, J. R., Moran, J. M., & Menten, K. M. 2002, ApJ, 569, 334

36 Erickson, E. F., & Tokunaga, A. T. 1980, ApJ, 238, 596

37 Falceta-Goncalves, D., Lazarian, A., & Kowal, G. 2008, ApJ, 679, 537

38 Feldt, M., Stecklum, B., Henning, Th., Launhardt, R., & Hayward, T. L. 1999, A&A, 346, 243

39 Feldt, M., Puga, E., Lenzen, R., Henning, Th., Brandner, W., Stecklum, B., Lagrange, A.-M., Gendron, E., & Rousset, G. 2003, ApJ, 599, L91

40 Fiedler, R. A., & Mouschovias, T. Ch. 1993, ApJ, 415, 680

41 Fish, V. L, Reid, M. J., Argon, A. L., & Zheng, X.-W. 2005, ApJS, 160, 220

42 Frerking, M. A., Langer, D. L., & Wilson, W. W. 1982, ApJ, 262, 590

43 Galli, D., & Shu, F. H. 1993, ApJ, 417, 243

44 Gaume, R. A., Johnston, K. J., & Wilson, T. L. 1993, ApJ, 417, 645

45 Gaume, R. A., & Mutel, R. L. 1987, ApJS, 65, 193

46 Genzel, R., Reid, M. J., Moran, J. M., & Downes, D. 1981, ApJ, 244, 884

47 Genzel, R., Downes, D., Schneps, M. H., Reid, M. J., Moran, J. M., Kogan, L. R., Kostenko, V. I., Matveenko, L. I., & Ronnang, B. 1981, ApJ, 247, 1039

48 Girart, J. M., Rao, R., & Marrone, D. P. 2006, Sci., 313, 812

49 Girart, M. M., Beltran, M. T., Zhang, Q., Estalella, R., & Rao, R. 2009, Sci., in press

50 Girart, J. M., Crutcher, R. M. & Rao, R. 1999, ApJ, 525, L109

51 Goddi, C., Greenhill, L. J., Chandler, C. J., Humphreys, E. M. L., Matthews, L. D., & Gray, M. D. 2009, arXiv: 0904.1373v1

52 Goldreich, P., & Kylafis, N. D. 1981, ApJ, 243, 75

53 Goncalves, J., Galli, D., & Walmsley, M. 2005, A&A, 430, 979

54 Goodman, A. A., Jones, T. J., Lada, E. A., & Myers, P. C. 1995, ApJ, 448, 748

55 Gomez, L., Rodriguez, L. F., Loinard, L., & Lizano, S. 2005, ApJ, 635, 1166

56 Greenhill, L. J., Reid, M. J., Chandler, C. J., Diamond, P. J., & Elitzur, M. 2004, in IAU Symp. 221, Star Formation in High Angular Resolution, ed. M. G. Burton, R. Jayawardhana, & T. L. Bourke (Cambridge: Cambridge Univ. Press), 115

57 Harvey, P. M., & Forveille, T. 1988, A&A, 197, L19

58 Ho, P. T. P., Genzel, R. & Das, A. 1983, ApJ, 266, 596

59 Ho, P. T. P., & Young, L. M. 1996, ApJ, 472, 742

60 Ho, P. T. P., Moran, J. M., & Lo, K. Y. 2004, ApJ, 616, 1

61 Hofner, P., & Churchwell 1996, A&AS, 120, 283

62 Hofner, P., Wyrowski, F., Walmsley, C. M., & Churchwell, E. 2000, ApJ, 536, 393

63 Hunter, T. R., Churchwell, E., Watson, C., Cox, P., Benford, D. J., & Roelfsema, P. R. 2000, AJ, 119, 2711

64 Hunter, T. R., Brogan, C. L., Indebetouw, R., & Cyganowski, C. J. 2008, ApJ, 680, 127

65 Heitsch, F., Zweibel, E. G., Mac Low, M.-M., Li, P., & Norman, M. 2001, ApJ, 561, 800

66 Imai, H., Deguchi, S., Fujii, T., Glass, I. S., Ita, Y., Izumiura, H., Kameya, O., Miyazaki, A., Nakada, Y., & Nakashima, J.-I. 2002, PASJ, 54, 741

67 Imai, H., Watanabe, T., Omodaka, T. et al. 2002, PASJ, 54, 741 Kraemer, K. E., Jackson, J. M., & Deutsch, L. K., et al. 2001, ApJ, 561, 282

68 Jaffe, D. T., Genzel, R., Harper, D. A., Harris, A. I., & Ho, P. T. P. 1987, in IAU Symp. 115, Star Forming Regions, ed. M. Peimbert & J. Jugaku (Dordrecht: Reidel), 143

69 Keto, E. & Klaassen, P. 2008, ApJ, 678, L109

70 Kirby, L. 2009, ApJ, 694, 1056

71 Kirk, J. M., Ward-Thompson, D.,& Crutcher, R. M. 2006, MNRAS, 369, 1445

72 Kleinmann, D. E., & Low, F. J. 1967, ApJ, 149, L1

73 Klessen, R. S., Heitsch, F., & Mac Low, M.-M. 2000, ApJ, 535, 887

74 Kramer, C., Alves, J., Lada, C., Lada, E., Sievers, A., Ungerechts, H., & Walmsley, M. 1999, A&A, 342, 257

75 Krumholz, M., Stone, J. M., & Gardiner, T. A. 2007, ApJ, 671, 518

76 Krumholz & Tan 2007, ApJ, 654, 304

77 Kurtz, S., Hofner, P., & Alvarez, C. V. 2004, ApJS, 155, 149

78 Kylafis, N. D. 1983, ApJ, 267, 137

79 Lai, S.-P., Crutcher, R. M., Girart, Josep M., & Rao, Ramprasad 2001, ApJ, 561, 864

80 Lai, S.-P., Crutcher, R. M., Girart, J. M., & Rao, R. 2002, 566, 925

81 Lai, S.-P., Girart, J. M., & Crutcher, R. M. 2003, ApJ, 598, 392

82 Lazarian, A., & Hoang, T. 2007, MNRAS, 378, 910

83 Lazarian, A. 2007, Journal of Quantitative Spectroscopy & Radiative Transfer, 106, 255

84 Leahy, P. 1989, VLA Scientific Memoranda 161 (Socorro: VLA)

85 Lis, D. C., et al. 1998, ApJ, 509, 299

86 Lizano, S., & Shu, F. H. 1989, ApJ, 342, 834

87 Mac Low, M.-M., & Klessen, R. S. 2004, Rev. Mod. Phys., 76, 125

88 Marrone, D. P., Moran, J. M., Zhao, J.-H., & Rao, R. 2006, ApJ, 640, 308

89 Marrone, D. P., & Rao, R. 2008, in Millimeter and Submillimeter Detectors and Instrumentation for Astronomy IV., ed. W. D. Duncan, W. S. Holland, S. Withington, & J. Zmuidzinas (Proceedings of the SPIE), 7020, p. 70202B-70202B-8 (arXiv:0807.2255)

90 Martin, A. 1972, MNRAS, 157, 31 Matthews, B. C., Wilson, C. D., & Fiege, J. D. 2001, ApJ, 562, 400

91 Matthews, B. C. et al. 2005, ApJ, 626, 959

92 Matthews, B. C., Wilson, C. D., & Fiege, J. D. 2001, ApJ, 562, 400

93 Mauersberger, R., Henkel, C., & Wilson, T. L., 1987, A&A, 173, 352

94 McKee, C. F. 1989, ApJ, 345, 782

95 Menten, K. M. & Reid, M. J. 1995, ApJ, 445, L157

96 Mestel, L., & Spitzer, L. 1956, MNRAS, 116, 503

97 Mezger, P. G., Sievers, A. W., Haslam, C. G. T., Kreysa, E., Lemke, R., Mauersberger, R., & Wilson, T. L. 1992, A&A, 256, 631

98 Migenes, V., & Wilson, T. L. 1989, ApJ, 347, 294

99 Motte, F., Bontemps, S., Schilke, P., Schneider, N., Menten, K. M., & Broguiere, D. 2007, A&A, 476, 1243

100 Mouschovias, T. Ch., & Spitzer, L. 1976, ApJ, 210, 326

101 Mouschovias, T. ch. 1978, in Protostars and Planets, ed. T. Gehrels (Tucson: University of Arizona Press), p. 209

102 Mouschovias, T. Ch., & Ciolek, G. E. 1999, in The Origin of Stars and Planetary Systems, ed. C. J. Lada & N. D. Kylafis (Dordrecht: Kluwer), 305 Nakano, T., & Nakamura, T. 1978, PASJ, 30, 681

103 Mouschovias, T. CH., & Morton, S. 1991, 371, 296

104 Mouschovias, T. Ch. 1991, ApJ, 373, 169

105 Nakano T. 1979, PASJ, 31, 697

106 Netterfield, C. B. 2009, arXiv: 0904.1207v1

107 Okamoto, Y., Kataza, H., Yamashita, T., Miyata, T., & Onaka, T. 2001, ApJ, 553, 254

108 Ostriker, E. C., Stone, J. M., & Gammie, C. F. 2001, ApJ, 546, 980

109 Pelkonen, V.-M., Juvela, M. & Padoan, P. 2009, arXiv:0901.0831v2

110 Plambeck, R. L., Wright, M. C. H., Mundy, L. G., & Looney, L. W. 1995, ApJ, 455, L189

111 Pratap, P., Menten, K. M., Reid, M. J., Moran, J. M., & Walmsley, C. M. 1991, ApJ, 373, L13

112 Puga, E., Feldt, M., Alvarez, C., Henning, Th., Apai, D., Coarer, E. Le, Chalabaev, A., & Stecklum, B. 2006, ApJ, 641, 373 Ramesh, B., Bronfman, L., & Deguchi, S. 1997, PASJ, 49, 307

113 Rao, R., Crutcher, R. M., Plambeck, R. L., & Wright, M. C. H. 1998, ApJ, 502, L75

114 Reipurth, B., Rodriguez, L. F., & Chini, R. 1999, ApJ, 118, 983

115 Reid, M. J., Menten, K. M., Greenhill, L. J., & Chandler, C. J. 2007, ApJ, 664, 950

116 Rohlfs, K., & Wilson, T. L. 2004, Tools of Raido Astronomy (4th ed; Berlin: Springer)

117 Rudolph, A., Welch, W. J., Palmer, P., & Dubrulle, B. 1990, ApJ, 363, 528

118 Sault, R. J., Hamaker, J. P., & Bregman, J. D. 1996, A&AS, 117, 149

119 Sault, R. J., Teuben, P. J., & Wright, M. C. H. 1995, in ASP Conf. Ser. 77, Astronomical Data Analysis Software and Systems IV, ed. R. A. Shaw, H. E. Payne, & J. J. E. Hayes (San Francisco: ASP), 433

120 Schleuning, D. A. 1998, ApJ, 493, 811

121 Schneps, M. H., Lane, A. P., Downes, D., Moran, J. M., Genzel, R., & Reid, M. J. 1981, ApJ, 249, 124

122 Scoville, N., Kleinmann, S. G., Hall, D. N. B., & Ridgway, S. T. 1983, ApJ, 275, 201

123 Shuping, R. Y., Morris, M., & Bally, J. 2004, AJ, 128, 363

124 Shu, F., Allen, A., Shang, H., Ostriker, E. C., & Li, Z.-Y. 1999, in The Origin of Stars and Planetary Systems, ed. Charles J. Lada & Nikolaos D. Kylafis, (Dordrecht: Kluwer), 193

125 Shu, F. H., Li, Z.-Y., & Allen, A. 2004, ApJ, 601, 930

126 Sollins, P. K., et al. 2004, ApJ, 616, 35

127 Sollins, P. K., Zhang, Q., & Ho, P. T. P. 2004, ApJ, 606, 943

128 Stark, D. P., Goss, W. M., Churchwell, E. Fish, V. L., & Hoffman, I. M. 2007, ApJ, 656, 943

129 Takahashi, S., Ho, P. T. P., Tang, Y.-W., Kawabe, R., & Saito, M. 2009, ApJ, submitted

130 Tan, J. 2005, in IAU Symp. 227, Massive Star Birth: A Crossroads of Astrophysics, ed. R. Cesaroni, et al. (Cambridge: Cambridge Univ. Press), 318

131 Tang, Y.-W., Ho, P. T. P., Koch, P. M., Girart, J. M., Lai, S.-P., & Rao, R. 2009, ApJ, in press

132 Tang, Y.-W., Ho, P. T. P., Girart, J. M., Rao, R., Koch, P., & Lai, S.-P. 2009, ApJ, 695, 1399

133 Vaillancourt, J. E. 2009, in Astronomical Polarimetry 2008: Science from Small to Large Telescopes, eds. P. Bastien and N. Manset (astroph:// arXiv:0904.1979)

134 Vaillancourt, J. E. et al. 2008, ApJ, 679, L25

135 Vallee, J. P., & Fiege, J. 2007, AJ, 133, 1012

136 Wardle, J. F. C., & Kronberg, P. P. 1974, ApJ, 194, 249

137 Ward-Thompson, D., Kirk, J. M., Crutcher, R. M., Greaves, J. S., Holland, W. S., & Andre, P. 2000, ApJ, 537, L135

138 Ward-Thompson, D., Andre, P., Crutcher, R., Johnstone, D., Onishi, T., & Wilson, C. 2006, Protostars and Planets V, ed. B. Reipurth, D. Jewitt, & K. Keil (Tucson, AZ: Univ. Arizona Press), 33

139 Watson, C., Churchwell, E., Zweibel, E. G., & Crutcher, R. M. 2007, ApJ, 657, 318

140 Wilson, T. L., Gaume, R., & Johnston, K. J. 1991, A&A, 251, L7

141 Wilson, T. L., Gaume, R. A., Gensheimer, P., & Johnston, K. J. 2000, ApJ, 538, 665

142 Wood, D. O. S., & Churchwell, E. 1989, ApJS, 69, 831

143 Zapata, L. A., Palau, A., Ho, P. T. P., Schilke, P., Garrod, R. T., Rodriguez, L. F., & Menten, K. 2008, A&A, 479, L25

144 Zapata, L. A., Ho, P. T. P., Schilke, P., Rodriguez, L. F., Menten, K., Palau, A., & Garrod, R. 2009, ApJ, accepted

145 Zapata, L. et al. 2009, in prep.

146 Zhang, Q., & Ho, P. T. P. 1995, ApJ, 450, L63

147 Zhang, Q., & Ho, P. T. P. 1997, ApJ, 488, 241

148 Zhang, Q., Ho, P. T. P., & Ohashi, N. 1998, ApJ, 494, 636

149 Zijlstra, A. A., Pottasch, S. R., Engels, D., Roelfsema, P. R., Hekkert, P. T., & Umana, G. 1990, MNRAS, 246, 217

150 Zuckerman, B., & Evans, N. J. 1974, ApJ, 192, L149

CURRICULUM VITAE

Personal Data

Surname:	Tang
First name:	Ya-Wen
Nationality:	Taiwan
Contact address:	Academia Sinica
	Institute of Astronomy and Astrophysics
	P.O.Box 23-141
	Taipei 106, Taiwan, R.O.C.
Phone:	(886) 2 33 65 22 00 ext. 818
Email:	ywtang@asiaa.sinica.edu.tw

Education

09/2004 - 06/2009:	PhD, Physics
	Institute of Physics, National Taiwan University, Taiwan
	Supervisor: Dr. Paul Ho
	Thesis:
	Evolution of Magnetic Fields in High Mass Star Formation
06/2003:	M.S., Astronomy
	Institute of Astronomy, National Tsing Hua University, Taiwan
06/2001:	B.S., Earth Sciences, sub-major in Physics
	National Taiwan Normal University, Taiwan

Working experience

10/2006 - 06/2009:	**Second shift operator**	
	Observatory:	Submillimeter Array
07/2003 - 08/2004:	**Research Assistant**	
	Institute:	ASIAA
	Supervisor:	Dr. Paul Ho

Computer, Software and Programming Experience

C, Mathematica, Matlab, Gnuplot

Astronomical Software: MIR-IDL, MIRIAD, AIPS, GILDAS

Publication List

1. "Millimeter Imaging of the HH 270 Protostellar Core and Outflow" Choi, M., & **Tang, Y.-W.**, 2006, ApJ, 648, 504

2. "Prevalence of Tidal Interactions among Seyfert Galaxies: the Control Experiment" **Tang, Y.-W.**, Kuo, C.-Y., Lim, J., & Ho, P. T. P., 2008, ApJ, 679, 1094

3. "Prevalence of Tidal Interactions among Local Seyfert Galaxies" Kuo, C.-Y., Lim, J., **Tang, Y.-W.**, & Ho, P. T. P., 2008, ApJ, 679, 1047

4. "First Confirmed Detection of a Bipolar Molecular Outflow from a Young Brown Dwarf" Phan-Bao, N., Riaz, B., Lee, C.-F., **Tang, Y.-W.**, Ho, P. T. P., Martin, E. L., Lim, J., Ohashi, N., & Shang, H. 2008, ApJ, 689, L141

5. "Evolution of Magnetic Fields in High Mass Star Formation: SMA dust polarization image of the UCHII region G5.89-0.39" **Tang, Y.-W.**, Ho, P. T. P., Girart, J. M., Rao, R., Koch, P. M., & Lai, S.-P. 2009, ApJ, 695, 1399

6. "Evolution of Magnetic Fields in High Mass Star Formation: Linking Field Geometry and Collapse for the W51 e2/e8 Cores" **Tang, Y.-W.**, Ho, P. T. P., Koch, P. M., Girart, J. M., Lai, S.-P., & Rao, R. 2009, ApJ, in press

7. "Evolutionary Status of Brightest and Youngest Source in the Orion Molecular Cloud-3 region" Takahashi, S., Ho, P., **Tang, Y.-W.**, Kawabe, R., Saito, M. 2009, ApJ, submitted